

# **Alma Mater Studiorum – Università di Bologna**

## **DOTTORATO DI RICERCA IN AUTOMOTIVE PER UNA MOBILITÀ INTELLIGENTE**

**Ciclo 35**

**Settore Concorsuale:** 09/E2 - INGEGNERIA DELL'ENERGIA ELETTRICA

**Settore Scientifico Disciplinare:** ING-IND/32 - CONVERTITORI, MACCHINE  
E AZIONAMENTI ELETTRICI

### **High power density electrical machines with hairpin windings**

**Presentata da:**  
Mohammad Soltani

**Coordinatore Dottorato:**  
Prof. Nicolo Cavina

**Supervisore:**  
Prof. Davide Barater

**Co-Supervisore:**  
Prof. Giovanni Franceschini

Esame finale anno 2023

## **Declaration**

I hereby declare that the contents and organization of this dissertation constitute my own original work and do not compromise in any way the rights of third parties, including those relating to the security of personal data.

\* This dissertation is presented in partial fulfilment of the requirements for the **Ph.D. degree** in the Graduate



## **Abstract**

Nowadays, the interest in electric propulsion is increasing due to the need to decarbonize society. Electric drives and their components play a key role in this electrification trend. The electrical machine is seeing an ever-increasing development and extensive research is currently being dedicated to the improvement of its efficiency and torque/power density. Although the standard preliminary sizing of electrical machines equipping random windings is well consolidated and is worldwide acknowledged to be a good starting point for the design, there is a lot of research to do and currently on-going when it comes to hairpin windings. Recently, hairpin windings are receiving more and more interest from both industry and academia, as they are a promising solution to achieve the above requirements all together. Compared to conventional random windings, it inherently features lower DC resistance, higher fill factor, better thermal performance, improved reliability, and an automated manufacturing process. However, several challenges still need to be addressed, including electromagnetic, thermal and manufacturing aspects. Of these, the high ohmic losses at high-frequency operations due to skin and proximity effects (AC losses) are the most severe, resulting in low efficiency or high-temperature values in the machine.

First, in this work, a comparative design is done using the classical sizing tools available in the literature between two surface-mounted permanent magnet synchronous machines, one featuring a random winding and one with a hairpin layout. This part of the study aims at highlighting the hairpin winding challenges at high-frequency operations and at showing the limits of applicability of these standard approaches when applied to this technology. In the second step, a multi-objective design optimization is proposed aiming to provide a fast and useful tool

to enhance the exploitation of the hairpin technology in electrical machines. Efficiency and volume power density are considered as main design objectives. The analytical and finite element evaluations are performed to support the proposed methodology.

In the third stage, a changing paradigm is made for the design of electric motors equipped with hairpin windings, where it is proven that a temperature-oriented approach would be beneficial when designing this type of pre-formed winding. Furthermore, the effect of the rotor topology on AC losses is also considered. After providing design recommendations and finite element electromagnetic and thermal evaluations, experimental tests are also performed for validation purposes on a motorette wound with pre-formed conductors. The results show that operating the machine at higher temperatures could be beneficial to the overall efficiency, particularly in high-frequency operations where AC losses are higher at low operating temperatures.

Another challenge of hairpin windings which is considered in this research relates to the need of reducing the welding spots within the winding, thus increasing the reliability of the welding process. Hence, the solution may be to adopt continuous hairpin windings. Nevertheless, these involve open slot designs or special stator arrangements, which can produce undesirable effects in motors, such as torque ripple, increased permanent magnet losses, etc. The last part of the thesis focuses on comparing the main electromagnetic performance metrics for a conventional hairpin winding, wound onto a benchmark stator with a semi-closed slot opening design, and a continuous hairpin winding, in which the slot opening is open. Lastly, the adoption of semi-magnetic slot wedges is investigated to improve the overall performance of the motor.

# Contents

## Chapter 1

<b>Introduction.....</b>	<b>1</b>
1.1 Transportation requirements .....	1
1.2 Traditional windings .....	2
1.3 Hairpin windings.....	3
1.4 Optimization .....	4
1.5 Skin and proximity Effects .....	5
1.6 Continuous Hairpin winding.....	6
1.7 Summary of research .....	8

## Chapter 2

<b>Hairpin versus Round windings .....</b>	<b>10</b>
2.1 Introduction.....	10
2.2 Preliminary Design Process .....	10
2.2.1 Starting requirements and assumptions .....	10
2.2.2 Sizing calculations .....	11
2.2.3 Power losses.....	13
2.2.4 Design at increased frequency operation .....	16
2.2.5 Summary of results .....	17
2.3 FE Analysis- Validation and Discussion .....	17
2.3.1 Validation of analytical results .....	18
2.3.2 Further considerations and discussion .....	24

---

2.4	Conclusion .....	24
<b>Chapter 3</b>		
<b>Optimization Process .....</b>		<b>26</b>
3.1	Introduction.....	26
3.2	Preliminary Design Process .....	27
3.2.1	Assumptions and Constraints.....	27
3.3	Optimization Process .....	29
3.4	Results.....	31
3.4.1	Preliminary Sensitivity Analysis and Validation of the Analytical Model.....	31
3.4.2	Effective parameters .....	35
3.4.3	MOEA Results and Comparison.....	37
3.5	Conclusion .....	40
<b>Chapter 4</b>		
<b>AC and DC loss Analysis.....</b>		<b>42</b>
4.1	Introduction.....	42
4.2	Practical design .....	43
4.3	Analysis of Ohmic Losses versus Temperature.....	45
4.4	Analysis of Losses versus Rotor Topologies.....	50
4.4.1	Ohmic Losses versus Different Rotor Topologies.....	50
4.4.2	Analysis of Ohmic Losses versus Both Temperature and Rotor Topologies .....	52
4.5	Experimental test .....	55
4.6	Conclusion .....	60
<b>Chapter 5</b>		
<b>Continuous Hairpin winding .....</b>		<b>62</b>
5.1	Introduction.....	62
5.2	The benchmark motor.....	62

---

5.3	Conventional vs. continuous hairpin winding performance comparison .....	64
5.3.1	First rotor position .....	64
5.4	Investigation with Magnetic Wedge .....	67
5.4.1	Selection of the M-W permeability and comparison .....	69
5.4.2	Analysis of ohmic loss and efficiency .....	72
5.5	Conclusion .....	74
<b>Chapter 6</b>		
<b>Conclusions.....</b>		<b>76</b>
<b>References.....</b>		<b>79</b>

## List of Figures

FIGURE 1.1	A QUALITATIVE VIEW OF A SLOT CROSS SECTION FOR (A) REGULAR ROUND WINDING, (B) MODIFIED ROUND WINDING, AND (C) RECTANGULAR WINDING. ....	3
FIGURE 1.2	A GENERAL EXAMPLE SHOWING THE NON-UNIFORM CURRENT DENSITY DISTRIBUTION IN HAIRPIN CONDUCTORS DURING HIGH-FREQUENCY OPERATIONS. ....	7
FIGURE 2.1	MACHINE GEOMETRIES RESULTING FROM THE PRELIMINARY ANALYTICAL DESIGN WITH (A) HAIRPIN WINDINGS AT 200HZ; (B) ROUND WINDING AT 200HZ; (C) HAIRPIN WINDING AT 1000HZ; (D) ROUND WINDING IN 1000HZ.....	16
FIGURE 2.2	COMPARISON OF ANALYTICAL (IN RED) AND FE (IN BLUE) FLUX DENSITY VALUES FOR THE MOTOR WITH ROUND WINDING AT 200 HZ IN (A) TEETH, (B) YOKE AND (C) AIRGAP	20
FIGURE 2.3	COMPARISON OF ANALYTICAL (IN RED) AND FE (IN BLUE) FLUX DENSITY VALUES FOR THE MOTOR WITH HAIRPIN WINDING AT 200 HZ IN (A) TEETH, (B) YOKE AND (C) AIRGAP	21
FIGURE 2.4	COMPARISON OF ANALYTICAL (IN RED) AND FE (IN BLUE) FLUX DENSITY VALUES FOR THE MOTOR WITH ROUND WINDING AT 1000 HZ IN (A) TEETH, (B) YOKE AND (C) AIRGAP	21
FIGURE 2.5	COMPARISON OF ANALYTICAL (IN RED) AND FE (IN BLUE) FLUX DENSITY VALUES FOR THE MOTOR WITH ROUND WINDING AT 1000 HZ IN (A) TEETH, (B) YOKE AND (C) AIRGAP	22
FIGURE 2.6	OUTPUT FE TORQUE IN THE HAIRPIN AND ROUND WINDING DESIGNS AT 200HZ	22
FIGURE 2.7	OUTPUT FE TORQUE WITH THE HAIRPIN AND ROUND WINDING DESIGNS AT 1000HZ	23
FIGURE 2.8	LINE-TO-LINE VOLTAGE WITH THE HAIRPIN AND ROUND WINDING IN 200 HZ AND ITS HARMONIC ORDERS .....	23
FIGURE 2.9	LINE-TO-LINE VOLTAGE WITH THE HAIRPIN AND ROUND WINDING IN 1000 HZ AND ITS HARMONIC ORDERS .....	23
FIGURE 3.1	SEQUENTIAL TASK DECOMPOSITION FOR MOEA.....	31
FIGURE 3.2	PRELIMINARY SENSITIVITY ANALYSIS. ....	33
FIGURE 3.3	FE ONE POLE PAIR MODEL OF THE MOTOR WITH THE HAIRPIN WINDING, HIGHLIGHTING FLUX DENSITY MAP (T) AND FIELD LINES DISTRIBUTION AT FULL-LOAD OPERATION. ....	33
FIGURE 3.4	OUTPUT TORQUE (IN BLUE) AND ITS AVERAGE VALUE (IN RED) WERE OBTAINED VIA FE ANALYSIS. ....	34
FIGURE 3.5	FE NO-LOAD LINE-TO-LINE VOLTAGE (IN BLUE) AND ITS FUNDAMENTAL HARMONIC (IN RED) VS. ANALYTICAL NO-LOAD LINE-TO-LINE VOLTAGE (IN GREEN).....	34
FIGURE 3.6	COMPARISON IN TERMS OF FLUX DENSITY IN THE AIRGAP, TEETH, AND YOKE. .	35
FIGURE 3.7	EFFECT OF THE INPUT PARAMETERS ON THE TOTAL POWER LOSSES. ....	36
FIGURE 3.8	EFFECT OF THE INPUT PARAMETERS ON THE VOLUME POWER DENSITY.....	37
FIGURE 3.9	COMPARISON BETWEEN THE GEOMETRIES OF (A) THE FIRST ANALYZED MOTOR AND (B) THE OPTIMAL MOTOR. ....	38

FIGURE 3.10	COMPARISON BETWEEN THE GEOMETRIES OF (A) THE FIRST ANALYZED MOTOR AND (B) THE OPTIMAL MOTOR. ....	39
FIGURE 3.11	COMPARISON BETWEEN THE MAIN PARAMETERS FOR THREE DESIGNED MOTORS IN THIS CHAPTER. ....	40
FIGURE 4.1	OPTIMIZATION RESULTS FOR THE DESIGN OF THE SURFACE PMSM WITH HAIRPIN WINDING.44	
FIGURE 4.2	THE GEOMETRY OF THE NEWLY DESIGNED OPTIMAL MOTOR. ....	45
FIGURE 4.3	DC AND AC LOSSES VERSUS FREQUENCY AT AMBIENT TEMPERATURE (20 °C) ..	47
FIGURE 4.4	PMS, CORE, AND TOTAL LOSSES VERSUS FREQUENCY AT AMBIENT TEMPERATURE (20 °C). ....	48
FIGURE 4.5	THE FEA TEMPERATURE MAP OF THE CONSIDERED SURFACE PMSM. ....	48
FIGURE 4.6	DC AND AC LOSSES VERSUS FREQUENCY AT THE STEADY-STATE TEMPERATURE. 49	
FIGURE 4.7	COMPARISON IN TERMS OF TOTAL LOSSES VERSUS FREQUENCY BETWEEN AMBIENT AND STEADY-STATE TEMPERATURE OPERATION. ....	49
FIGURE 4.8	ROTOR TOPOLOGIES: (A) TOPOLOGY 2, (B) TOPOLOGY 3, (C) TOPOLOGY 4, AND (D) TOPOLOGY 5. ....	51
FIGURE 4.9	COMPARISON IN TERMS OF LOSSES VERSUS FREQUENCY AMONG THE FIVE TOPOLOGIES CONSIDERED. ....	51
FIGURE 4.10	COMPARISON IN TERMS OF DC POWER LOSSES AMONG THE FIVE CONSIDERED TOPOLOGIES, AT BOTH AMBIENT AND STEADY-STATE TEMPERATURE CONDITIONS. ....	53
FIGURE 4.11	COMPARISON IN TERMS OF TOTAL LOSSES VERSUS FREQUENCY BETWEEN AMBIENT AND STEADY-STATE TEMPERATURE OPERATIONS FOR ALL INVESTIGATED TOPOLOGIES. ....	53
FIGURE 4.12	COMPARISON AMONG THE FIVE CONSIDERED TOPOLOGIES IN TERMS OF (1) THE FREQUENCY AT WHICH $K_{RU} = 2$ AT AMBIENT TEMPERATURE (IN BLUE), (2) THE FREQUENCY AT WHICH $K_{RU} = 2$ AT STEADY-STATE TEMPERATURE (IN RED), AND (3) THE FREQUENCY OF INTERSECTION POINT WHERE THE TOTAL OHMIC LOSSES AT STEADY-STATE TEMPERATURE BECOME LOWER THAN THOSE AT AMBIENT TEMPERATURE (IN YELLOW). ....	54
FIGURE 4.13	INSTANTANEOUS CURRENT DENSITY AT THE INTERSECTION FREQUENCY POINT IN STEADY-STATE CONDITION FOR THE FIVE ROTOR TOPOLOGIES, (A)FIRST TOPOLOGY (SMPMSM), (B) SECOND TOPOLOGY, (C) THIRD TOPOLOGY (MAGNETS EMBEDDED IN THE CORE), (D) FOURTH TOPOLOGY (THE CLASSICAL V SHAPE), FIFTH TOPOLOGY (THE CLASSICAL $\Delta$ SHAPE). ....	55
FIGURE 4.14	INSTANTANEOUS CURRENT DENSITY IN THE CONDUCTORS WITHIN ONE SLOT OF ALL FIVE CONSIDERED TOPOLOGIES, IN THE WORST-CASE SCENARIO. ....	55
FIGURE 4.15	MOTORETTE WOUND AS Q=2 AS LOAD EQUIPPED WITH HAIRPIN. ....	56
FIGURE 4.16	EXPERIMENTAL SETUP TESTBENCH .....	58
FIGURE 4.17	CURRENT WAVEFORM AND ITS AMPLITUDE HARMONIC SPECTRUM AT 200HZ. 59	
FIGURE 4.18	OHMIC POWER LOSS OF MOTORETTE IN FIVE DIFFERENT TEMPERATURES (A) FEM RESULT (B) EXPERIMENTAL RESULT .....	60
FIGURE 5.1	AN ANGULAR SECTOR OF A 2D CROSS-SECTION OF THE BENCHMARK MOTOR. .	63

FIGURE 5.2	THE SLOT OPENING GEOMETRY: (A) SEMI-CLOSED, (B) OPEN, (C) OPEN WITH M-W.	63
FIGURE 5.3	3D MEAN TORQUE VALUES VS. CURRENT ANGLE AND LOADING FOR THE MOTOR WITH (A) A SEMI-CLOSED SLOT, (B) AN OPEN SLOT; (C) MEAN TORQUE HEAT MAP FOR THE MOTOR WITH A SEMI-CLOSED SLOT AND (D) WITH AN OPEN SLOT. ....	66
FIGURE 5.4	TORQUE RIPPLE HEAT MAP VS. CURRENT ANGLE AND LOADING FOR THE MOTOR WITH (A) SEMI-CLOSED SLOT AND (B) OPEN SLOT.....	66
FIGURE 5.5	THE TORQUE RIPPLE DIFFERENCE BETWEEN SEMI-CLOSED SLOT OPENING MOTOR (CONVENTIONAL HAIRPIN WINDING) AND OPEN SLOT OPENING MOTOR (CONTINUOUS HAIRPIN WINDING).....	67
FIGURE 5.6	THE MEAN TORQUE CURVES VERSUS CONTROL ANGLE (DEG.) FOR ANY INDIVIDUAL LOAD (P.U.) IN DIFFERENT M-W PERMEABILITIES AND THE SPECIFIED CONTROL ANGLE EQUIVALENT TO THE MAXIMUM MEAN TORQUE VALUE.....	68
FIGURE 5.7	THE MEAN TORQUE HEAT MAP VS. LOAD AND CONTROL ANGLE USING DIFFERENT PERMEABILITY VALUES FOR THE M-W .....	69
FIGURE 5.8	TORQUE RIPPLE HEAT MAP VS. LOAD AND CONTROL ANGLE USING DIFFERENT PERMEABILITY VALUES FOR THE M-W .....	69
FIGURE 5.9	WITH A DIFFERENT PERMEABILITY OF M-W FOR A 1 P.U. LOAD (A) MEAN TORQUE VALUE, (B) TORQUE RIPPLE PERCENTAGE (%). ....	71
FIGURE 5.10	THE TORQUE RIPPLE DIFFERENCE BETWEEN SEMI-CLOSED SLOT OPENING MOTOR (CONVENTIONAL HAIRPIN WINDING) AND OPEN SLOT OPENING WITH AN M-W MOTOR (CONTINUOUS HAIRPIN WINDING) .....	71
FIGURE 5.11	THE AC-TO-DC LOSS RATIO VS. FREQUENCY FOR THE MOTORS WITH DIFFERENT SLOT OPENING DESIGNS. ....	73
FIGURE 5.12	EFFICIENCY DIFFERENCE IN TORQUE-SPEED MAP FOR SEMI-CLOSED SLOT VERSUS OPEN SLOT OPENING WITH M-W .....	73
FIGURE 5.13	EFFICIENCY DIFFERENCE IN TORQUE-SPEED MAP FOR OPEN SLOT OPENING VERSUS OPEN SLOT OPENING WITH M-W .....	74

### List of Tables

TABLE 2.1	EXPECTED PERFORMANCE FROM PROTOTYPE DESIGN.....	13
TABLE 2.2	EXPECTED PERFORMANCE FROM PROTOTYPE DESIGN.....	13
TABLE 2.3	SUMMARY OF THE ANALYTICAL DESIGNS FOR RANDOM AND HAIRPIN WINDING..	18
TABLE 2.4	COMPARISON BETWEEN ANALYTICAL AND FE RESULTS .....	20
TABLE 3.1	DESIGN CHOICES AND REQUIREMENTS.....	28
TABLE 3.2	MOTOR DESIGN PARAMETERS.....	28
TABLE 3.3	DESIGN CHOICES AND SYMBOLS.....	28
TABLE 3.4	SUMMARIZING COMPARISON AMONG THE BENCHMARK MOTOR [50], THE HAIRPIN MOTOR OBTAINED THROUGH THE FIRST SENSITIVITY ANALYSIS AND THE OPTIMUM HAIRPIN MOTOR.....	39

TABLE 4.1	DESIGN SUMMARY OF THE PMSM AND COMPARISON VERSUS THE PREVIOUS DESIGN IN CHAPTER 3 .....	44
TABLE 4.2	MOTORETTE'S SPECIFIC PARAMETERS USED AS A LOAD FOR THE TEST .....	56
TABLE 4.3	POWER LOSS (W) RESULTS ACHIEVED FROM THE EXPERIMENTAL TEST BENCH AT DIFFERENT FREQUENCIES AND TEMPERATURES. ....	58
TABLE 5.1	MAXIMUM MEAN TORQUE VALUE AND THEIR CONTROL ANGLES FOR BOTH SEMI-OPEN SLOT AND OPEN SLOT .....	66
TABLE 5.2	MAXIMUM MEAN TORQUE VALUE AND THEIR CONTROL ANGLES WITH DIFFERENT PERMEABILITY .....	68

# Chapter 1

## Introduction

### 1.1 Transportation requirements

The average energy efficiency of internal combustion engine (ICE) vehicles to convert fuel energy into motion is between 10 and 20 percent. The residual fuel energy is wasted in terms of heat or expelled into the air, which accounts for nearly 80-90% of fuel waste. Therefore, more efficient, and further enhanced performance vehicles are needed to reduce fuel consumption and greenhouse gas exhaust emissions. Electrification of transportation is a well-accepted approach that can significantly reduce oil dependence, fuel dissipation, and environmental effects in transportation systems [1,2]. A great deal of ongoing research and development is currently underway in the transportation sector, where vehicle electrification plays one of the most critical roles in lowering emissions and maximizing efficiency. In the years ahead, mobility will increasingly become reliant on electrification. One of the key components in the powertrain of hybrid electric vehicles (HEVs) and battery electric vehicles (BEVs) is the electric motor [3]. Performance is highly dependent on the mass of vehicle components. Consequently, maximizing power and torque density is an important objective in the development of electric drives for transportation applications [4,5]. Traction applications are driving the limits of high speed and power density with breakthroughs in cores, magnets, and winding designs [6]. Nevertheless, while higher speed means more power for a given torque, it also means additional losses in cores and windings, thereby reducing overall efficiency. Therefore, designing an

electric machine that meets all the above objectives is a very complex task. In that respect, the selection of a proper winding structure plays a key role. Overall, there is not one optimal winding frame, but it depends on the application. In today's perspective of prioritizing torque density, permanent magnet synchronous machines (PMSMs) are extensively utilized as propulsion motors in traction applications [7]. Most notably, internal PM machine (IPM) provides high power density, high efficiency, and a wide speed range, all of which are requirements for traction applications [8].

## **1.2 Traditional windings**

When operating at a comparatively low frequency, the current distribution in the armature conductors is normally uniform. In higher frequency ranges, if proper precautions are not taken, skin and proximity effects may appear, resulting in higher conductor resistances and losses. Various winding techniques, such as Litz wires, have been introduced to alleviate these phenomena. Nevertheless, these are characterized by a low copper-to-insulation ratio within the slot (fill factor), high manufacturing expense, and complicated forming and impregnation operations, making them appropriate only for applications at very high frequencies. Applications in the area of transportation, and particularly the automotive sector, are rather economical and therefore the most favourable solution is random winding, which is featured by strands of larger cross-sections than those utilized in Litz wire [9]. The active sides of each coil turn are arranged randomly against each other. One of the main merits of this type of winding is flexibility. Random winding varies from integer-slot windings to fractional windings, from single-layer to multiple-layer structures, from distributed to concentrated configurations, and from full-pitch to short-pitch layouts. While the random winding is a good compromise between cost and performance, its fill factor is low, and the volume and mass of the motor would be greater, so depending on the application, the power density is relatively low. Also, the random distribution of conductors

within the slots can cause the winding voltage distribution to be uneven, undermining overall reliability [10].

### 1.3 Hairpin windings

The stator winding of traction machines also can be with form-wound windings or hairpin winding consisting of flat rectangular conductors [11]. In high-power density traction applications, hairpin windings are widely spreading and currently seeing an ever-increasing interest in several documents [12–15]. The most noticeable advantage of form-wound windings over random windings is the rise in the slot fill factor, i.e., the ratio of conductive to insulating materials within the slot. Rectangular flat wires can fit the shape of the slot perfectly when it is also rectangular, i.e., when the slot has parallel sides along the radial direction of the machine. To reinforce this concept, Figures 1-1(a) and (b) show the "layered" round wire winding methods, while Figure 1-1(c) shows a rectangular wire winding arrangement [16].

In this case, a flat rectangular copper wire is pre-formed into a hairpin shape and inserted into the slot, then the open sides are properly twisted and welded to form a coil. In comparison with round windings, the length of the end-winding is shortened and, as a result, the DC copper loss is reduced [17].

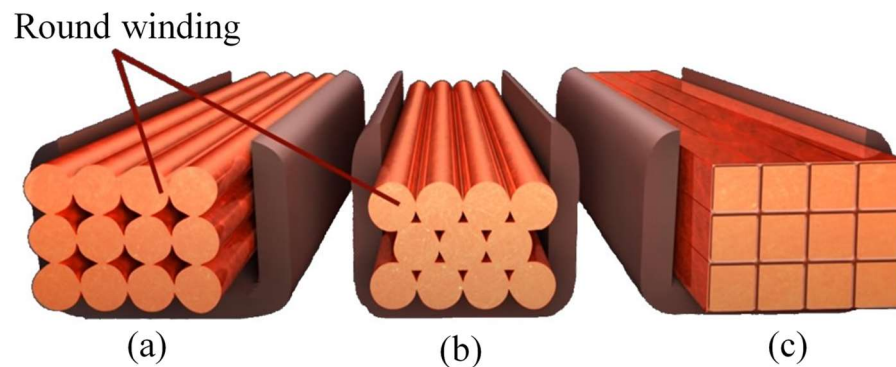


Figure 1.1 A qualitative view of a slot cross section for (a) regular round winding, (b) modified round winding, and (c) rectangular winding.

In addition to this characteristic of the final winding, the flat and "massive" shape of each hairpin leg reduces the DC copper loss generated by the active parts compared to their round-wound counterparts. Furthermore, in a mass production context, the production of hairpin windings can be favorable in terms of cost and cycle time compared to the traditional, often manual, random winding method [18]. Its main inherent advantages are a higher fill factor, better thermal slot conductivity, lower DC resistance, better voltage distribution and an automated fabrication process, which make hairpin windings suitable for the automotive industry [19-22]. For all these reasons, in traction applications, hairpin techniques are increasingly gaining attention due to their potential in reaching higher power and torque densities [23-26]. Nevertheless, this technology also has some drawbacks. One major outstanding issue is power loss at higher frequencies, which limits the applicability of hairpin winding machines to high-speed applications. Many methods have already been suggested to surmount this major challenge, [2], [27-30] and ongoing research is focusing on this point.

## **1.4 Optimization**

On the other hand, since the technology is relatively recent, not much research is available on the design optimization of machines equipped with this type of winding, while several studies concentrating on optimization techniques have been proposed for electrical machines with random windings. For instance, the analysis, design, and optimization of a PMSM destined for a campus patrol electric vehicle were reported in [31]. Its optimization objectives included the minimization of voltage harmonic content and torque ripple. The optimum stator inductances and resistance of a PMSM were calculated in [32] using a particle swarm optimization (PSO) method. Furthermore, the maximization of the flux-weakening region was pursued in [33], where a surface-mounted PMSM was optimized. In [34], the torque ripple of a PMSM under both transient state and steady-state conditions was minimized through an analytical solution. A multi-

physics optimization program based on a multi-objective genetic algorithm was developed in [35], to achieve a trade-off solution among the electromagnetic, mechanical, and thermal aspects.

Regarding hairpin windings, a design optimization was performed in [36], where the objective of the optimization study was to minimize torque ripple, while little consideration was given to the most crucial challenge of hairpin windings, i.e., high copper losses in the high-frequency operation. This is in consequence of skin and proximity effects, in which the AC supply current flows in a fraction of the conductor's cross-sectional area. These phenomena are accentuated in high-frequency operation and lead to an increase in the effective conductor resistance (and thus losses) [37].

A simple motor design for traction applications was presented in [38] but with no optimization strategy being implemented. In [39], an induction motor equipped with hairpin winding was optimized aiming at a low-cost and rare-earth-free design. However, the number of hairpin layers in the slot was kept fixed, thus limiting the degrees of freedom of the design optimization. Additional work has been recently published on hairpin windings, but they focus either on modelling aspects (e.g., AC loss estimation [30]) or preliminary calculations [40] or sensitivity analyses [41].

## 1.5 Skin and proximity Effects

Considering the above, the combination of PMSM with hairpin windings maximizes the torque density of the motor itself and, therefore, of the powertrain and vehicle. However, the biggest issue with hairpin windings is the high-frequency losses (i.e., AC losses). Figure 1.2 shows an instance of a current density map in 6 fork windings within a motor slot. As it turns out, the current density is not uniformly distributed in some conductors, thus causing an increase in equivalent resistance and losses. In the general example below, the frequency was set to a relatively high value, i.e., 1 kHz, aiming to highlight the

abovementioned high-frequency phenomena. Several methods have been recently proposed to mitigate these phenomena in hairpin windings, especially the use of unconventionally shaped conductors near the slot opening. However, all these studies assume the effect of the rotor field is negligible on skin and proximity effects, and thus the rotor usually is not modelled in the relevant analysis tools. In addition, the positive effects of having reduced losses on the operating temperatures have been shown, as well as investigations on the cooling systems to be implemented when hairpin windings are adopted. On the other hand, for a given hairpin layout, the effects of the operating temperature on the losses have not been investigated so far. In fact, while the result is known for the DC losses, i.e., the resistivity increases with temperature, the impact on AC losses is not obvious, especially for variable speed/frequency operations. Therefore, although the importance of ohmic loss evaluation and thermal analysis for PMSMs equipped with hairpin windings has already been highlighted in previous studies, the effect of temperature variation in hairpin conductors on AC losses at different working frequencies is not detailed.

## **1.6 Continuous Hairpin winding**

Concerning the production complexity, machine structure and performance, the insertion direction of the rectangular wire windings can be in two methods, including the radial direction and the axial direction.

where the radial insertion direction is the same as the traditional stranded wire windings inserted from the slot opening to the slot bottom. Therefore, due to the larger cross-sectional area of the copper conductors, the slot shape of the rectangular wire winding machine is always the parallel slot structure consisting of the open slot. However, the twisting can only be accomplished after the rectangular wires have been inserted in the slots, which furtherly raises the production difficulty [42].

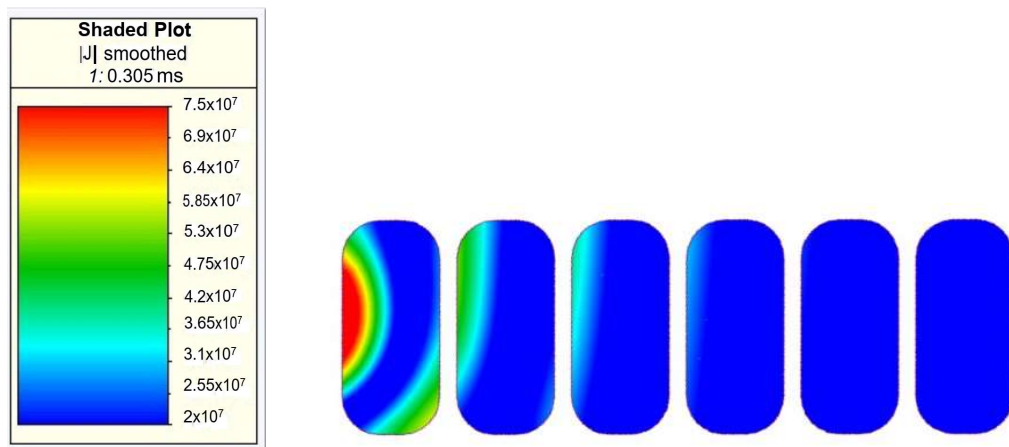


Figure 1.2 A general example showing the non-uniform current density distribution in hairpin conductors during high-frequency operations.

There are several methods to avoid the welding points of conductors in end-winding. The most rational way for rectangular hairpin winding is using continuous hairpin winding [43,44]. This method consists of performed elements that build more than one coil. This reduces the number of welding spots. The cycle time is also reduced, and the winding process is easier compared to conventional hairpins. However, open slot structures or novel stator arrangements are required to allow continuous insertion into the slots. Such concepts are associated with new electromagnetic and production challenges. Manufacturing of PMSMs equipped with continuous hairpin winding allows for easier and faster insertion of the conductors into the slots radially, which have to be open, with several drawbacks including an Increase in the Carter factor and the equivalent length of the airgap, with a consequently greater reluctance of the magnetic path, a Worsening of the harmonic content of the magnetic field, and an increase in the torque ripple, due to the significant discontinuity of the magnetic permeability of the stator core [45]. Open and closed slot openings have been ever a parameter to control the electromagnetic performance of different types of motors [46,47].

## 1.7 Summary of research

On the other hand, only a few works deal with a comparison in terms of design procedure between random and hairpin windings [48-49]. Therefore, in chapter 2, the aim is to use the classical sizing equations typically used for random-wound electric machines and also for the preliminary design of machines equipping hairpin windings. As a case study, a surface-mounted PM motor intended for a traction application is considered and a comprehensive comparison between random and hairpin winding designs is provided. Finite element (FE) evaluations are also performed for validation purposes, finally highlighting the limits of applicability of the classical sizing equations to the design of electrical machines with hairpin windings.

In Chapter 3, the goal is to use dedicated optimization strategies for the design of an electrical machine with hairpin windings intended for a race car application. As a case study to further explore the above concepts, a surface-mount PMSM designed "roughly" in [50] is considered. The design realized in [50] is based on a stator with random winding, so the initial goal of this work is to transform the random winding into a hairpin winding, while the second step is to move from a "rough" machine design to an optimal one. For this purpose, two objective functions were selected: maximization of the volume power density and minimization of the power losses. These are indeed the most critical and conflicting figures to achieve when hairpin windings are involved. Before implementing the optimization process, first, a sensitivity analytical study is carried out on the number of poles and slots per pole per phase. This led to defining a starting machine design which is used to validate the analytical sizing approach through the FE methodology. Once validated, the analytical tool is first used to perform a study on the parameters mostly affecting the selected objectives, and then to run the optimization to achieve an optimal solution. The

use of the analytical sizing equations ensures a limited computation burden compared to numerical-based (e.g., FE) approaches.

The fourth chapter tries to: (a) analyse the effect of temperature on the overall losses, (b) investigate the impact of different PM rotor topologies on the overall losses, and (c) analyse the effects on losses of both temperature and rotor topologies. The benchmark machine considered for the investigations at hand is a traction motor intended for racing car applications, whose full design process was proposed in [51], including a multi-objective optimization carried out aiming to maximize power density and minimize power losses. In this research, first, the design of this benchmark motor is refined considering the realistic and commercial dimensions of hairpin conductors. Then, the focus is on the temperature and topology impact on DC and AC losses, which is the main aim of this research. To carry out validation of the comparison between different conditions, experimental parameters were tested at different temperatures and frequencies for a motorette.

In the fifth chapter, investigations on the continuous hairpin winding are carried out. To overcome the problems arising from the design of the stator slot opening, it is possible to use magnetic or semi-magnetic wedges (M-W). In studies on the use of the M-W, parameters included of torque average, motor efficiency, and torque ripple are based on the motor geometry, rotor topology, air gap size, and the permeability of M-W [52-54]. However, a motor equipped with a continuous hairpin winding and suitable M-W has not yet been surveyed. In this research, it is tried to have a comparison between a verified prototypes motor with a semi-closed standard slot opening, an open slot with continuous winding and continuous with M-W with a different permeability and find a proper one.

# Chapter 2

## Hairpin versus Round windings

### 2.1 Introduction

Although the standard preliminary sizing of electrical machines equipping random windings is well consolidated and is worldwide acknowledged to be a good starting point for the design, there is no proof of accuracy and confidence when it comes to hairpin windings. In this chapter, a comparative design is done using the classical sizing tools available in the literature between two surface-mounted PMSMs, one featuring a random winding and one with a hairpin layout. The study aims at highlighting the hairpin winding challenges at high-frequency operations and at showing the limits of applicability of these standard approaches when applied to this technology. For verification purposes, FE evaluations are also performed.

### 2.2 Preliminary Design Process

#### 2.2.1 Starting requirements and assumptions

The design process is initialized by defining some basic machine performance requirements, such as output power, speed, voltage, and desired efficiency. The values of such input parameters are listed in Table 2.1.

The second step is making some assumptions about the materials and the cooling system. M330-50A and NdFeB are used for cores and PMs respectively, whereas

natural convection is hypothesized as a heat extraction method. This permits defining magnetic and electric loadings and the maximum flux density values allowed in the various parts of the motor. Some additional choices on the outer rotor diameter to axial length ratio, airgap thickness, PMs' span, number of slots-per-pole-per-phase and number of poles are initially made. The choice of the expected speed and the pole number is based on the desired operating frequency chosen for the design exercise, i.e., 200 Hz. For a fully fair comparison between round and hairpin windings, the same number of slots-per-pole-per-phase, i.e.  $q=3$ , is assumed and the stator structure is based on a distributed full-pitch, single-layer winding. Given the low degrees of freedom allowed by hairpin windings, the number of conductors per slot  $z_q$  in both random and hairpin winding designs is set to 4. A summary of all these parameters is provided in Table 2.2.

Considering the above and assuming the number of phases  $m$  equal to 3, the slot number is calculated as  $Q=q \cdot m \cdot 2p=72$  and the number of winding turns per phase as  $N= z_q \cdot q \cdot p=48$ . Also, given the type of winding structure initially assumed, the short pitch factor  $k_{cp}$  is equal to 1, while the distribution factor  $k_d$  is calculated as (2.1), where  $\beta$  is the slot pitch angle. The total winding factor  $k_w$  is given by the product of  $k_{cp} \cdot k_d$ .

$$k_d = \frac{\sin\left(\frac{q\beta}{2}\right)}{q \cdot \sin\left(\frac{\beta}{2}\right)} \quad (2.1)$$

It must be mentioned that some of the design parameters which were considered here as input design choices could be envisioned as output variables to be refined according to design requirements and constraints. However, for the sake of this chapter, the described design process is reasonable.

### 2.2.2 Sizing calculations

Having preliminarily selected the D/L ratio, the starting point for the motor sizing, either with random or hairpin windings, is the torque expression given in (2.2). In

(2.2)  $B$  is the RMS value of the fundamental airgap flux density  $B_{\max}$  obtained from (2.3) using the Fourier series decomposition of a square wave waveform. Equation (2.2) permits finding the values of  $D$  and  $L$ . Then, hypothesizing in the PMs the same flux density as in the airgap, (2.4) can be used to determine the thickness  $l_m$  of the PMs.

The total area of  $S_{\text{all-slots}}$  to be dedicated to the three machine phases can be calculated using (2.5), where  $k_{\text{ff}}$  is the slot fill factor. Yoke thickness  $W_y$  and tooth width  $W_t$  can be calculated using (2.6) and (2.7), respectively. In (2.6),  $\Phi_p$  is the physical flux per pole, whereas in (2.7)  $\lambda_s$  is the stator slot pitch in meters. It should be noticed that, so far, the sizing equations for both random and hairpin winding designs are basically the same.

The only step where the hairpin design played a role was related to the decision of fixing the number of conductors per slot, which is usually derived from the rated voltage  $V_{\text{LL}}$  instead. However, the major difference in the calculations is dictated by the choice of the fill factor. While for round windings  $k_{\text{ff}}$  is relatively low and, thus, this is taken equal to 0.5, in hairpin windings the fill factor is higher, and it is then assumed equal to 0.8 in this design exercise. These choices make the hairpin design inherently more compact than the round design, i.e., the outer stator diameter is smaller. Another important difference to mention is the slot shape. As recalled in Section 2.1, a trapezoidal slot shape is envisioned for the machine with random windings, whereas a rectangular shape is considered for the machine with hairpin windings.

$$T = \frac{\pi}{2} D^2 L B A \quad (2.2)$$

$$B_{\max} = \frac{4B_{ag}}{\pi} \cdot \sin\left(\frac{p \alpha_{PM}}{180} \cdot \frac{\pi}{2}\right) \quad (2.3)$$

$$l_m = \frac{\mu_r l_g}{\frac{B_r}{B_{ag}} - 1} \quad (2.4)$$

$$A = \frac{J \cdot S_{\text{all slots}} \cdot k_{\text{ff}}}{\pi D} \quad (2.5)$$

Table 2.1 Expected performance from prototype design

Parameter	Symbol	Amount
Output power	P	37.7 kW
Speed	nm	3000 rpm
Voltage	V <sub>LL</sub>	370 V
Efficiency	η	95 %

Table 2.2 Expected performance from prototype design.

Parameter	Symbol	Amount
Linear current density	A	40 kA/m
Current density	J	5 A/mm <sup>2</sup>
Airgap flux density	B <sub>ag</sub>	0.8 T
Teeth flux density	B <sub>t</sub>	1.6 T
Yoke flux density	B <sub>y</sub>	1.4 T
The residual flux density of PMs	B <sub>r</sub>	1.05 T
Relative permeability of PMs	μ <sub>m</sub>	1.05
Outer rotor diameter / axial length	D / L	1.1
Air-gap thickness	g	1 mm
Pole number	2p	8
Pole span	α <sub>PM</sub>	33°
Number of slots-per-pole-per-phase	q	3
Number of conductors per slot	Z <sub>q</sub>	4

$$W_y = \frac{\phi_p}{2B_y L} \quad (2.6)$$

$$W_t = \frac{B_{avg} \lambda_s}{B_t} \quad (2.7)$$

### 2.2.3 Power losses

Besides the design aspects, the most important factor to consider when designing an electrical machine with hairpin windings is the AC Joule losses. In random windings with stranded conductors, the AC losses can be neglected. Contrarily, in hairpin windings, AC losses need to be carefully considered and determined. Copper loss: In (2.8), the DC resistance  $R_{DC}$  of a machine phase depends on the total length of one coil  $L_c$ , the number of turns in series  $N$  and parallel paths per phase, the cross-sectional area of the conductor  $S_c$  and the conductivity of the conductive material  $\sigma_c$ , as the Pouillet's<sup>1</sup> law. Resistance is highly dependent on

<sup>1</sup> Claude Pouillet

the running temperature of the machine. Generally, machine resistances are first analyzed at the design temperature or the maximum allowable temperature for the selected winding type [6]. Likewise, the inverse of conductivity which has been called resistivity ( $\rho$ ), with a linear approximation has a relation with temperature as (2.9). where  $\alpha$  is called the temperature coefficient of resistivity,  $T_0$  is a fixed reference temperature (usually room temperature), and  $\rho_0$  is the resistivity at temperature  $T_0$ . Alpha ( $\alpha$ ) is a temperature coefficient of resistance representing the change in resistive change for each degree Celsius increase in temperature. Materials' specific resistance changes with temperature, just as it does for all materials at 20° C. It is a positive value for pure metals, increasing temperature resistance.

$$R_{DC} = \frac{L_c}{aS_c\sigma_c} \quad (2.8)$$

$$\rho(T) = \rho_0(1 + \alpha(T - T_0)) \quad (2.9)$$

Considering a uniform current distribution at any frequency in stranded conductors, the losses associated with the DC resistance are the only contribution to the random winding design. In hairpin conductors, skin and proximity effects and the ensuing AC losses are usually determined through the ratio between  $R_{AC}$  and  $R_{DC}$ . For each layer  $k$ , this ratio ( $k_{Rk}$ ) is determined using (2.10), where  $\varphi$ ,  $\psi$  and  $\xi$  are expressed as in (2.11), (2.12) and (2.13), respectively. In (2.14),  $h_{c0}$  and  $b_{c0}$  are the height and width of the sub-conductors, respectively;  $\omega$  is the supply frequency;  $\mu_0$  is the permeability of vacuum and with an approximation, the average resistance factor  $K_{Ru}$  over the slot could be found from (2.14) [6].

$$k_{Rk} = \varphi(\xi) + k(k - 1)\psi(\xi) \quad (2.10)$$

$$\varphi(\xi) = \xi \frac{\sinh 2\xi + \sin 2\xi}{\cosh 2\xi - \cos 2\xi} \quad (2.11)$$

$$\psi(\xi) = 2\xi \frac{\sinh \xi - \sin \xi}{\cosh \xi + \cos \xi} \quad (2.12)$$

$$\xi = h_{c0} \sqrt{\frac{1}{2} \omega \mu_0 \sigma_c \frac{b_c}{b}} \quad (2.13)$$

$$k_{Ru} = \frac{P_{AC}}{P_{DC}} = \varphi(\xi) + \frac{z_t^2 - 1}{3} \psi(\xi) \quad (2.14)$$

Iron loss: the laminations' manufacturers usually give the loss density in W/kg, at a specific frequency and flux density values. This includes both eddy current and hysteresis losses. Analytically, iron losses can be found by dividing the magnetic circuit of the machine into  $n$  sections, in which the flux density is approximately constant. Once the masses  $m_{Fe,n}$  of the different  $n$  sections are calculated from the volumes and mass densities, the losses  $P_{Fe,n}$  in these parts can be approximated as in (2.15). Here,  $k_{Fe,n}$  are "loss" coefficients that, for a synchronous machine, can be imposed equal to 2 in teeth and 1.6 in the yoke;  $P_{10,f}$  is the loss density at 1T and the designed frequency of 200 Hz;  $(\widehat{B}_n)$  is the maximum flux density in the  $n$ -th section (see Table 2.2).

$$P_{Fe} = \sum_n k_{Fe,n} P_{10} \left( \frac{\widehat{B}_n}{1T} \right)^2 m_{Fe,n} \quad (2.15)$$

Mechanical and additional losses: a preliminary approximation of the mechanical losses can be also obtained using (2.16), where  $P_B$  and  $P_w$  are the friction and windage losses, respectively;  $k_m$  is an empirical coefficient achieved from the Reynolds constant for an Aluminum coolant that is set equal to 2816 at 200 Hz;  $m_{Fe,r}$  is the rotor mass. Measurement methods to determine the additional load losses  $P_{add}$  under sinusoidal supply conditions are given in the IEC 60034-2-1[55]. This loss value for a non-salient-pole synchronous machine is between 0.05 and 0.15 times the input power. For the sake of completeness, the formula for the calculation of the volume power density is reported in (2-16). This is found through the ratio between the output power  $P$  and the machine volume  $Vol$ , which is defined once the main dimensions are all calculated.

$$P_{mech} = P_B + P_w = k_m \cdot m_{Fe,r} \cdot n_m \cdot 10^{-6} + \quad (2.16) \\ + 2D^3 \cdot n_m^3 L \cdot 10^{-14}$$

$$P_{Density} = \frac{P_{out}}{Vol} \quad (2.17)$$

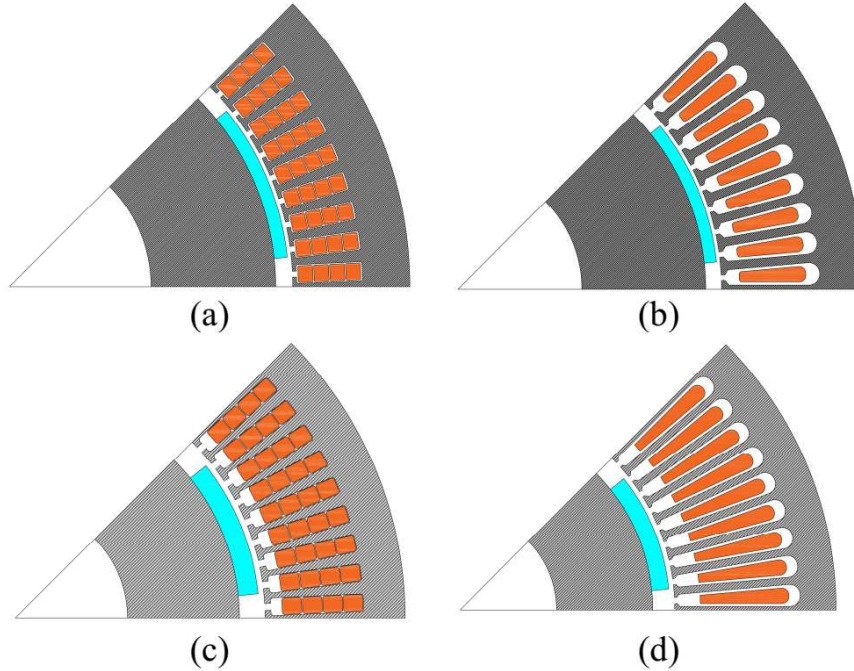


Figure 2.1 Machine geometries resulting from the preliminary analytical design with (a) hairpin windings at 200Hz; (b) round winding at 200Hz; (c) hairpin winding at 1000Hz; (d) round winding in 1000Hz

### 2.2.4 Design at increased frequency operation

To emphasize the high-frequency challenges of hairpin windings, the same design exercise described above is performed by selecting an operating frequency of 1000 Hz. To do so, a rated speed of 15000 rpm is initially assumed and the rated voltage value is increased up to 630 V. Other quantities like flux densities, current density, expected output power and efficiency, materials, etc. are the same as the design carried out at 200 Hz. This design should result in a smaller motor with higher AC losses in the hairpin winding, thus eventually lowering the efficiency. It is expected that the parameter  $\xi$  would be significantly increased at higher frequency values in the hairpin winding machine design. Referring to (2.13), a higher value of  $P_{10,f}$  is selected to take into account the frequency dependence of iron losses.

### 2.2.5 Summary of results

The geometries resulting from the preliminary analytical design process introduced above are illustrated in Figure 2.2, where random and hairpin winding machine designs at 200 Hz and 1000 Hz can be observed. A summary of the results obtained through the formulas introduced above is provided in Table 2.4 for all the considered case studies. In general, smaller machine designs are achieved by increasing the operating frequency, for both random and hairpin windings. Consequently, volumes and masses are reduced at 1 kHz. Also, for a given frequency, the core size decreases from round to hairpin. This causes a reduction of iron losses by 24.6% at 200 Hz and by 24.2% at 1000 Hz. Unlike the volume, it is irrefutable that with the choice of using a higher slot fill factor in the hairpin winding designs the mass density in round winding becomes higher than the hairpin one. The mass density in the round winding design is higher than in the hairpin one by 8.4% at 200 Hz and 28.8% at 1000 Hz. The higher fill factor also results in higher DC copper loss in the hairpin winding.

On the other hand, according to the hypotheses done above, the AC copper losses are considered only for hairpin conductors and as expected, these are much higher at high frequencies. The next section aims to validate the analytical results through purposely built FE models of the machines and, most importantly, to provide a critical analysis of the limits of applicability of the analytical sizing tool for hairpin windings.

## 2.3 FE Analysis- Validation and Discussion

The geometries resulting from the preliminary sizing tool shown in Figure 2.2 are imported into the FE-based MagNet software for validation purposes and for carrying out in-depth critical analyses. A major difference in terms of modelling consists of using “stranded” and “solid” conductors for random and hairpin windings, respectively.

Table 2.3 Summary of the analytical designs for Random and Hairpin winding

Main parameter	unit	200 Hz		1 kHz	
		Round winding	Hairpin winding	Round winding	Hairpin winding
$l_m$ (PM thickness)	mm	3.36	3.36	3.36	3.36
$D$ (outer rotor diameter)	mm	144.6	144.6	84.6	84.6
$L$ (stack length)	mm	159.1	159.1	93	93
$w_t$ (tooth width)	mm	2.3	2.3	1.4	1.4
$w_y$ (stator yoke thickness)	mm	12	12	7	7
$D_s$ (outer stator diameter)	mm	222.6	204.3	148.1	132
Stator core mass	kg	15.36	12.47	3.96	3.12
Rotor core mass	kg	20	20	4	4
Copper mass	kg	17.72	25.3	6.96	16.16
PM mass	kg	1.316	1.316	0.45	0.45
$P_{Cu}$ (DC copper losses)	W	141	194	53	83.68
$P_{Cu,AC}$ (AC copper losses)	W	138	307	53	322.5
$P_{Fe}$ (iron losses)	W	471.4	355.47	1809	1350
PM losses	W	19.3	13.92	15.6	12.88
$P_{mech}$ (mechanical losses)	W	194	194	361.4	361.4
$P_{ad}$ (additional losses)	W	47	47	47	47

This allows taking skin and proximity effects into account when the machines equipped with hairpins are analyzed. Also, when evaluating different frequency operations, the frequency of the current sources used to feed the three machine phases, as well as the speed imposed on the rotating components, are opportunely set. A suitable transposition in the hairpin winding models is used to avoid the presence of circulating currents among conductors [19].

### 2.3.1 Validation of analytical results

Before discussing the comparison between analytical and FE results in terms of global output quantities, such as those reported in Table 2.3, the conditions in Table 2.2 for flux densities should be fulfilled. From Figure 3 to Figure 6 plot the flux densities hypothesized for the analytical sizing (see Table 2.2) as constant quantities in red, whereas the FE results are shown in blue as a function of the angular coordinate on a stator reference frame at a fixed rotor position. The three subplots of these figures report the flux density absolute values in the teeth, stator yoke and airgap of all the considered machines. In particular, the results for the

motor with round windings at 200 Hz and 1000 Hz are shown in Figures 2.3 and 2.5 respectively, while those for the motor with hairpin windings at 200 Hz and 1000 Hz are shown in Figures 2.4 and 2.6. The match in any part of the studied machines is acceptable when the analytical findings are compared to the maximum flux density values obtained via FE analyses.

Regarding the output torque, Figure 2.7 plots the relevant trends for random and hairpin designs at 200 Hz obtained via the FE model, whereas Figure 2.8 shows the same quantities but at 1000 Hz. These torque evaluations are relatively close to the values assumed in the analytical calculations, with errors ranging from 2.3% to 7.22%.

The exact average values are reported in Table 2.4, where also a comprehensive summary of the two methods for both random and hairpin designs is provided, at both 200 Hz and 1000 Hz. Most of the analytical values differ by 10% compared to FE results. However, the AC losses present the highest inaccuracy when comparing the two methods. For the hairpin design, the error for  $k_{Ru}$  is  $\approx 60\%$  at 200 Hz and  $\approx 63.6\%$  at 1000 Hz. Consequently, the comparison in terms of overall copper losses and efficiency is not accurate for hairpin windings, whereas for random windings is reasonable. In Table 2.4, power, and torque densities for all the motors have been also compared for the sake of completeness. Figure 2.8 shows the line-to-line voltage for both winding methods for 200Hz frequency under full-load conditions and corresponding harmonic orders. The total harmonic distortion (THD) for hairpin winding is 13.42% and for round, the winding is 14.6%. At this frequency, the 3<sup>rd</sup> and 5<sup>th</sup> harmonic orders for the round winding are higher than the hairpin ones by 7.5% and 7.8%. Furthermore, Figure 2.9 illustrates the line-to-line voltage for both winding methods for 1000Hz frequency under full-load conditions and corresponding harmonic orders. The THD for hairpin winding is 14.12 % and for round, the winding is 14.6%. At this frequency also in lower harmonic orders i.e., 3<sup>rd</sup> and 5<sup>th</sup> for round winding are higher than hairpin one by 3% and 17%. The higher THD back electromotive force (EMF)

voltage causes frequent motor failure. Thus, the elimination of lower harmonic orders for hairpin winding is easier than round winding suggested methods in [56] with a multi-proportional resonant filter.

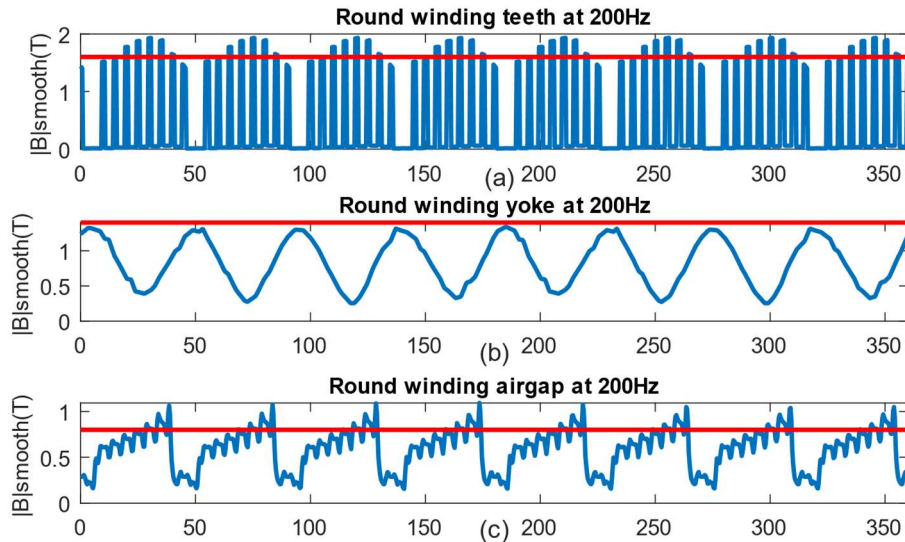


Figure 2.2 Comparison of analytical (in red) and FE (in blue) flux density values for the motor with round winding at 200 Hz in (a) teeth, (b) yoke and (c) airgap

Table 2.4 Comparison between Analytical and FE results

Main parameter	unit	200 Hz				1 kHz			
		Round winding		Hairpin winding		Round winding		Hairpin winding	
		Analytical	FEM	Analytical	FEM	Analytical	FEM	Analytical	FEM
$P_{\text{stator}}$ (stator power losses)	W	471.4	414	355.47	375	1809	1503	1350	1160
$P_{\text{cu}}$ (DC copper loss)	W	141	170.9	194	193	53	60	83.68	83.78
$k_{\text{Ru}}$ ( $R_{\text{ac}}/R_{\text{dc}}$ )	-	1	1	1.6	4	1	1	3.9	10.7
$P_{\text{cu,ac}}$	W	138	170.9	307	763	53	60	322.5	892.8
Torque Mean value	N.m	120.85	117.5	122.7	113.5	23.78	23.48	23.7	22.13
Volume power density	MW/m <sup>3</sup>	6.25	5.69	7.4	6.88	23.3	22.7	29.2	27.9
Mass power density	W/kg	728.35	708.1	666.9	616.9	2503.24	2472.5	1781.4	1663
Volume torque density	KN.m/m <sup>3</sup>	19.8	19.3	23.55	21.79	14.8	14.65	18.6	17.36
Mass torque density	N.m/kg	2.32	2.25	2.12	1.96	1.59	1.57	1.13	1.06
Output power	KW	37.97	36.91	38.55	35.66	37.35	36.90	37.23	34.77
Efficiency	(%)	95.67	93.02	97.14	89.85	94.13	92.97	93.81	87.61

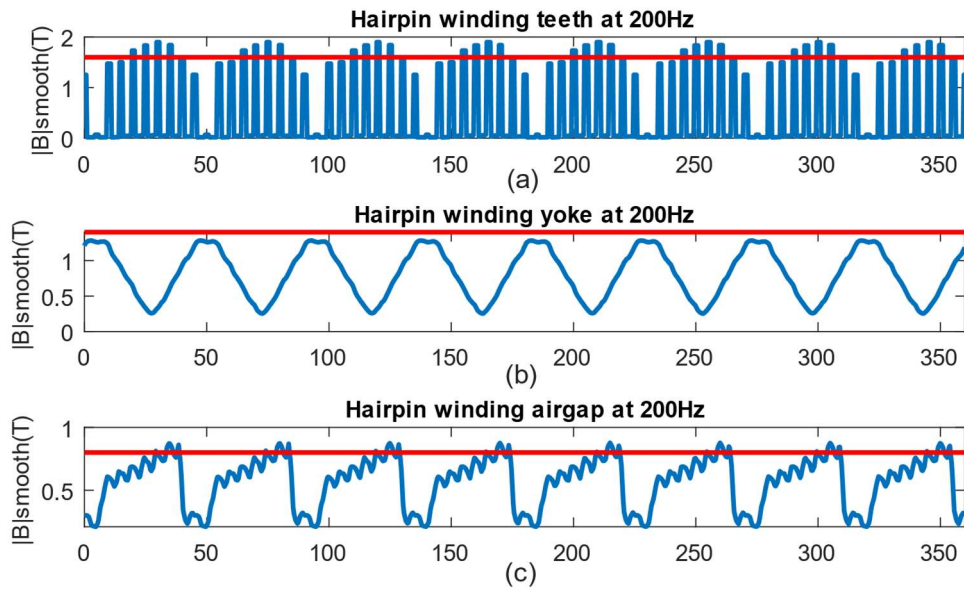


Figure 2.3 Comparison of analytical (in red) and FE (in blue) flux density values for the motor with hairpin winding at 200 Hz in (a) teeth, (b) yoke and (c) airgap

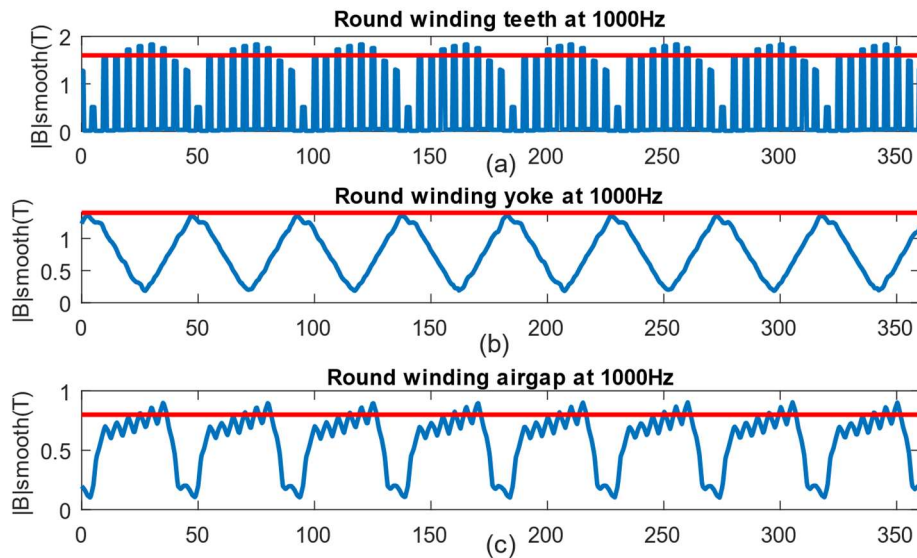


Figure 2.4 Comparison of analytical (in red) and FE (in blue) flux density values for the motor with round winding at 1000 Hz in (a) teeth, (b) yoke and (c) airgap

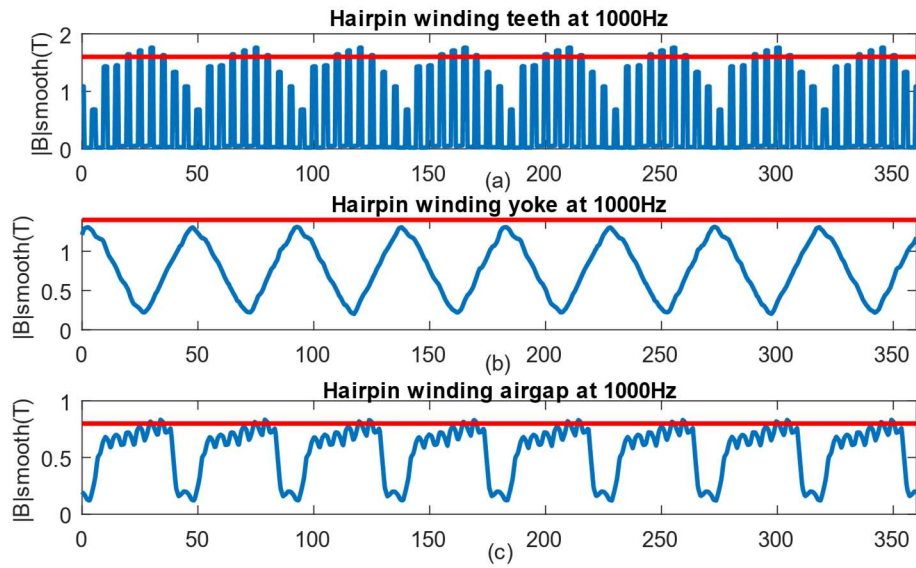


Figure 2.5 Comparison of analytical (in red) and FE (in blue) flux density values for the motor with round winding at 1000 Hz in (a) teeth, (b) yoke and (c) airgap

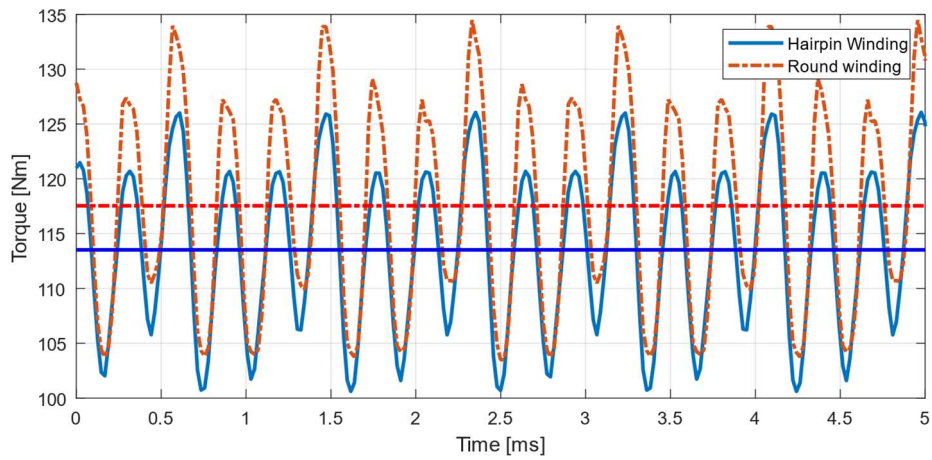


Figure 2.6 Output FE torque in the hairpin and round winding designs at 200Hz

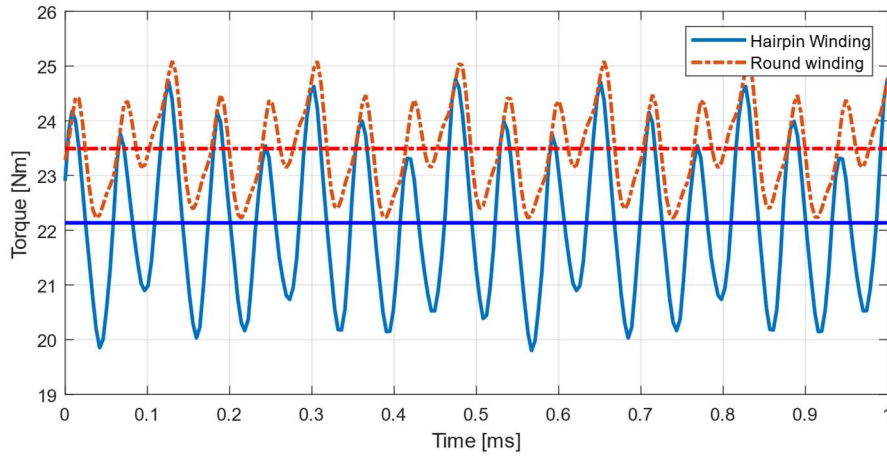


Figure 2.7 Output FE torque with the hairpin and round winding designs at 1000Hz

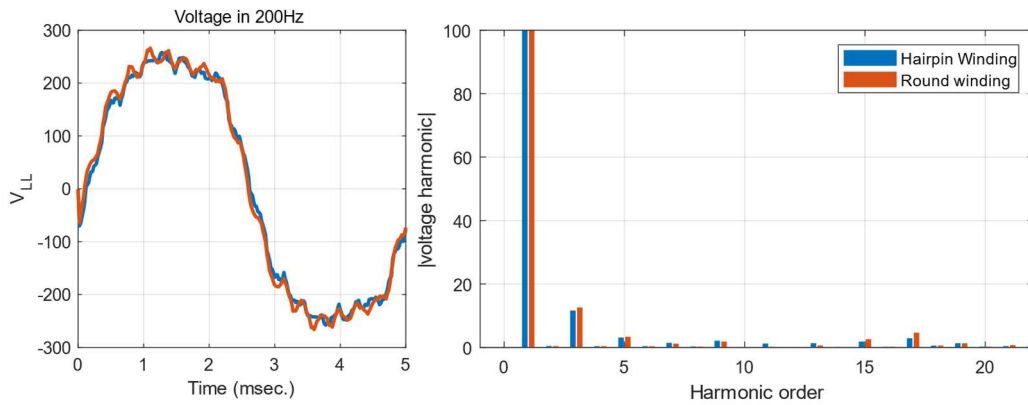


Figure 2.8 Line-to-Line voltage with the hairpin and round winding in 200 Hz and its harmonic orders

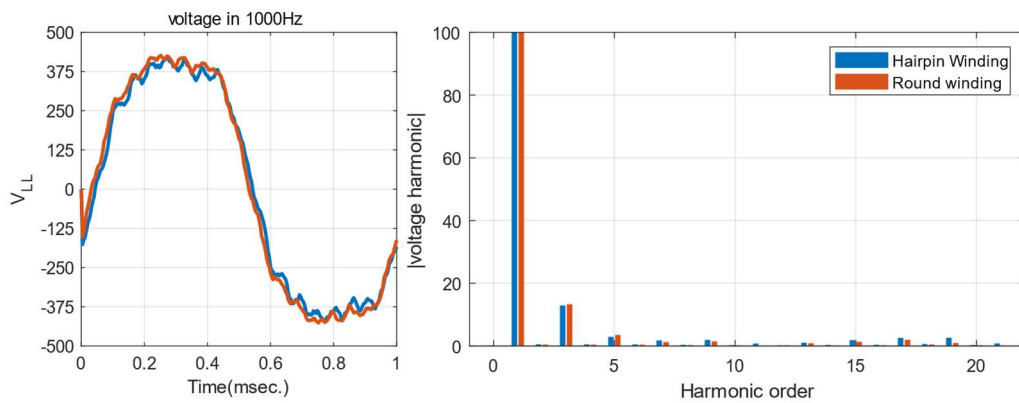


Figure 2.9 Line-to-Line voltage with the hairpin and round winding in 1000 Hz and its harmonic orders

### **2.3.2 Further considerations and discussion**

Always for the sake of clarity and completeness, comparing the overall performance of random and hairpin winding designs, it can be concluded that at low frequency (200 Hz) the round winding design presents higher efficiency, mass torque and power density than the hairpin winding. This is due to the larger amount of copper used for the design of the latter. On the other hand, the hairpin winding designs have higher volume torque and power densities than the random winding ones at both the investigated frequencies.

Recalling that this work aims to prove the applicability of the classical preliminary sizing equations also for machines equipping hairpin technologies, it can be concluded that for an accurate estimation of AC copper losses and efficiency, the analytical sizing tool cannot be used, regardless of the frequency at which the machine is designed. On the other hand, this classical sizing approach can be used for accurately estimating quantities, such as the output torque and power, as it shows an acceptable accuracy (or at least similar to that achieved when the sizing equations are applied to the design of machines with random windings).

## **2.4 Conclusion**

In this chapter, a comparative analysis was carried out between two surface-mounted PMSMs for traction applications, one featuring a random-wound winding with round conductors and the other one equipping a hairpin winding. These two machine preliminary designs were performed at two different frequencies, i.e. 200 Hz and 1 kHz, to highlight the high-frequency challenges associated with hairpin conductors.

After the preliminary design process, carried out leveraging on the classical sizing equations for electrical machines, FE models were built for validation purposes. The comparative analysis showed acceptable accuracy for most of the

electromagnetic quantities of interest. However, when it came to AC losses and efficiency, the validity of the preliminary sizing tool highlighted significant limitations, although an AC losses prediction model was implemented for hairpin windings. Therefore, while for random-wound windings the classical sizing equations could be used with a certain level of “safety”, hairpin windings require more accurate and in-depth analyses and the relative sizing tools need to be improved.

# Chapter 3

## Optimization Process

### 3.1 Introduction

The electrical machine, as already pointed out in the first chapter, is seeing an ever-increasing development and extensive research is currently being dedicated to the improvement of its efficiency and torque/power density. However, they also have some drawbacks, such as high losses at high-frequency operations due to skin and proximity effects. The optimal value or the best solution can be found through the optimization process. The optimization problems include looking for maximum or minimum value or using one objective or multi-objective. The state-of-the-art multi-objective optimization method has made a strong motivation to create a normal procedure to activate a new algorithmic contribution. This allows us to find the most appropriate algorithm for the multi-objective problem. It is desirable to have only a few solutions available for ease of decision-making. This chapter uses general mathematical definitions to design a motor with a multi-objective evolutionary algorithm (MOEA). This leads to find several members of the Pareto optimal set in a single “run” of the algorithm, instead of having to perform a series of separate runs as in the case of the traditional mathematical programming techniques. In this chapter, a multi-objective design optimization is proposed aiming to provide a fast and useful tool to enhance the exploitation of the hairpin technology in electrical machines. Efficiency and volume power

density are considered as main design objectives. Analytical and FE evaluations are performed to support the proposed methodology.

## 3.2 Preliminary Design Process

### 3.2.1 Assumptions and Constraints

In [50], the whole propulsion system of a Formula SAE [57] car was designed, with a detailed focus on the propulsion motor being the case study of this research. The selection of the system architecture, i.e., a two-motor layout implemented onto the rear non-steering axle, was based on budget considerations. Additional constraints, such as the overall dimensions of the chassis and those imposed by the race regulations were accounted for. When it came to the motor torque-speed usage during an endurance event, the resulting reduced flux-weakening region led to select the popular surface-mounted PMSM layout as the most suitable for this application, also considering lower production costs in a customized case, compared to interior PM or synchronous reluctance machine layouts.

The Formula SAE car project must meet a series of technical constraints imposed by the regulation. These are summarized as follows:

- The diameter of the wheels must be  $\geq 203.2$  mm.
- The maximum power  $P$  required from the battery must not exceed 80 kW.
- The maximum allowed DC-link voltage  $V_{DC}$  must not exceed 600 V.
- There are no limitations concerning the number and the type of electric motors.

A summary of the choices done in [50] is listed in Table 3.1. These are used as starting points for re-designing the motor with hairpin conductors and applying an optimization strategy to it. The main design parameters of the machine obtained in [50], used as a benchmark here, are listed in Table 3.2. These are used as starting

conditions for the analytical sizing tool implemented as the basis for the multi-objective optimization, and equations are reported in the next subsection.

The design process is initialized by defining some basic machine performance requirements, such as output power, speed, voltage, and desired efficiency [50]. The values of such input parameters are listed in Table 3.2. The second step is that of making some assumptions about the core materials and the cooling system, which are listed in Table 3.3, where also the main parameters used during the design process are described.

Table 3.1 Design choices and requirements.

Parameter	Condition
Motor topology	Surface-mounted PM
Motor's location	Rear-axle
Maximum torque to wheels	600 Nm
Reduction ratio	10
Motor rated torque	30 Nm
Base speed	12740 rpm

Table 3.2 Motor design parameters.

Parameter	Value
Mechanical power P	40 kW
Line-to-line Voltage V	540 V
Surface current density J	13 A/mm <sup>2</sup>
Airgap flux density $B_{ag}$	0.85 T
Maximum tooth flux density $B_t$	1.6 T
Maximum yoke flux density $B_y$	1.4 T
Linear current density A	70 A/mm
Targeted efficiency	95%

Table 3.3 Design choices and symbols.

Parameter	Condition
Core material	M330-50A
PM material	N28AH
Cooling system	Natural convection
Stator winding	Distributed, full-pitch, single layer
Fill factor	$k_{ff}$
Outer rotor diameter [mm]	$D$
Axial length [mm]	$L$
PM span [deg]	$\alpha_{PM}$
Number of phases	$m$
Number of slots-per-pole-per-phase	$q$
Pole pair number	$p$

Core materials and cooling system allow for defining magnetic and electric loadings and the maximum flux density values allowed in the various parts of the motor. Assuming the number of phases  $m$  is equal to 3, the slot number is calculated as  $Q = q \cdot m \cdot 2p$ , and the number of turns per phase as  $N = zq \cdot q \cdot p$ . Given the type of winding structure initially assumed, the short pitch factor  $k_{cp}$  is equal to 1, while the distribution factor  $k_d$  is calculated using (2.1). As the process to have a preliminary design in chapter 2, the starting point for the motor sizing is the torque expression given in (2.2) with a selected D/L ratio. Then, hypothesizing in the PMs the same flux density as in the airgap leveraging on Gauss' law, (2.4) can be used to determine the thickness  $l_m$  of the PMs. This means that the PMs are initially sized to meet the no-load requirements. In (2.4),  $B_r$  and  $\mu_r$  are the residual flux density and relative permeability of the PMs. The total area of  $S_{\text{all-slots}}$  to be dedicated to the three machine phases can be calculated using (2.5). Besides these design aspects, the most crucial factor to consider when designing an electrical machine with hairpin windings is the AC Joule losses. As mentioned in chapter one, in hairpin windings, AC losses need to be carefully considered and determined. For ohmic losses (2.8) and (2.14) are the main equations to determine the DC and AC losses for any slot.

### 3.3 Optimization Process

As mentioned in chapter 1, there are two objectives, i.e., the maximization of the volume power density (see (2.17)) and the minimization of power losses (see section 2.2.3), which are equivalent to maximizing efficiency. There are four input variable parameters, i.e., pole pair number, slot per pole per phase number, conductors' number in the slots ( $N$ ), and motor's axial length. Additionally, several constraints must be met for the optimization process. Therefore, an MOEA could be used, which needs to set the weight of the input parameters based on their effect on the two objectives, and a starting point for initializing the first population. Using the equations introduced in chapter 2, a sensitivity analysis is

first carried out to understand the dependence of the two objectives on the four variable parameters. To define a sequential task decomposition, the outline of an EA is needed. The detailed related outline, sequence, mutation, and recombination processes have been provided in [58] as definitions 19 and 20.

The MOEA expects a single fitness value with which to perform the selection. Additional processing is sometimes required to transform MOEA solutions' fitness vectors into a scalar. Its sequential task decomposition includes initialized population, fitness evaluation, which has a sub-level as vector transformation, recombination, mutation, and selection. Figure 3.1 shows these decomposition tasks in five sections which has the main loop for selecting the data between the third and fifth levels [58].

$$2 \leq 2p \leq 8 \quad (3.1)$$

$$1 \leq q \leq 8 \quad (3.2)$$

$$10\text{mm} \leq L \leq 100\text{mm} \quad (3.3)$$

$$V_{L-L} \leq 540 \text{ V} \quad (3.4)$$

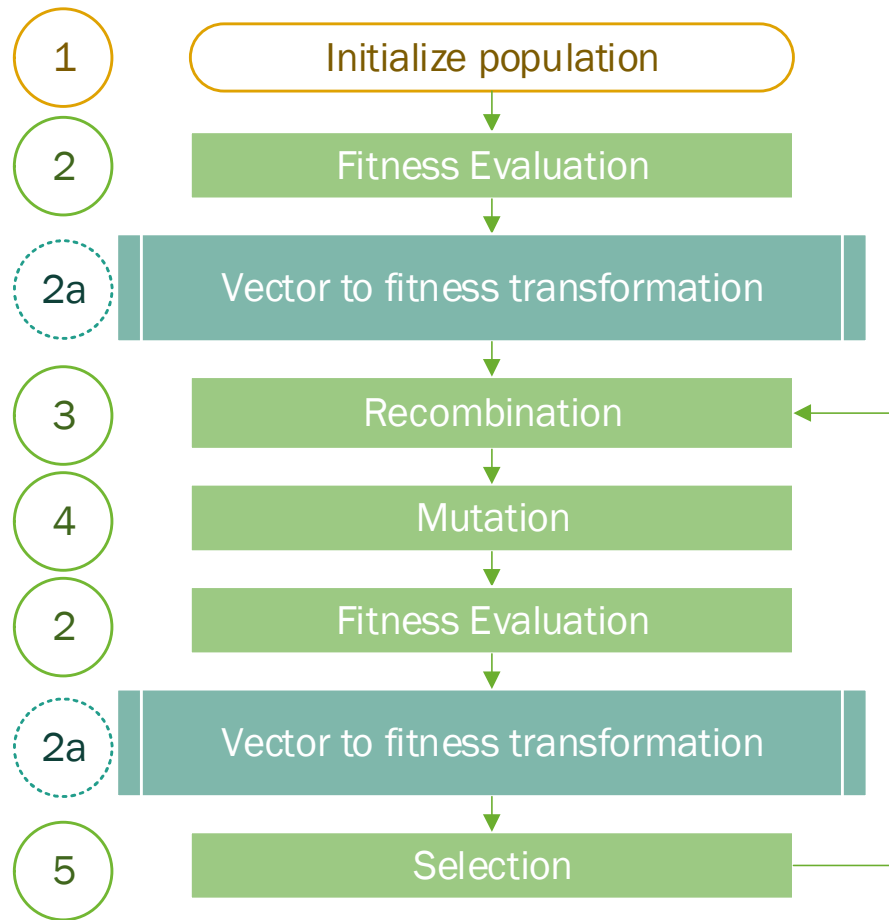


Figure 3.1 Sequential task decomposition for MOEA.

## 3.4 Results

### 3.4.1 Preliminary Sensitivity Analysis and Validation of the Analytical Model

Before using the analytical model for optimization purposes, it needs to be validated against the more accurate FE method. Once validated, it can be safely used for optimizations, thus saving computation time as opposed to FE. An initial sensitivity analysis could be carried out by varying the number of poles and slots per pole per phase while keeping the other parameters constant. The sensitivity analysis results are illustrated in Figure 3.2, where power losses and volume power density are taken as indicators to suitably select  $q$  and  $p$ . The best solution

is achieved with  $p = 4$  and  $q = 2$ . The selected  $p$ - $q$  combination represents the best trade-off in terms of maximum power density and minimum power losses. In fact, only two machines (referred to as “A” and “B” in the figure) achieve higher power density values, but these feature much larger losses (by 8.9% and 23.9%, respectively).

The dimensions analytically obtained are used to build the machine geometry and a corresponding model within the FE-based software MagNet. Figure 3.3 shows the FE model of the motor, enriched with a flux density map and field lines distribution. Figure 3.4 plots the output torque obtained with the currents in phase with the corresponding back electromotive forces, with an average value equal to 30.1 Nm being obtained. This matches well the torque value of 30 Nm assumed in the analytical sizing. Besides the torque, the analytical and FE no-load voltage and flux density values in the various parts of the motor are compared. Figure 3.5 shows a comparison between the fundamental harmonic of the line-to-line voltage (red line) obtained from FE simulations and the corresponding sinusoidal waveform assumed for the analytical sizing (in green), with an error lower than 1% being achieved. For completeness, the FE voltage waveform evaluated via FE is also observed in Figure 3.5. In addition, Figure 3.6 illustrates the flux densities in the airgap and the main iron parts of the motor, with the blue lines referring to FE results and the red text relative to the analytical assumptions (see Table 3.2). Good matching is observed, with an error ranging from 3% to 8%, thus allowing us to conclude that the analytical sizing equations, although suitable for preliminary sizing only, can be safely used for optimization purposes. In the next subsection, the effect of some machine parameters on power density and power losses are investigated before proceeding with the optimization. This study allows weighting any of the input parameters in the multi-objective optimization process which will be the focus of Section 3.4.3.

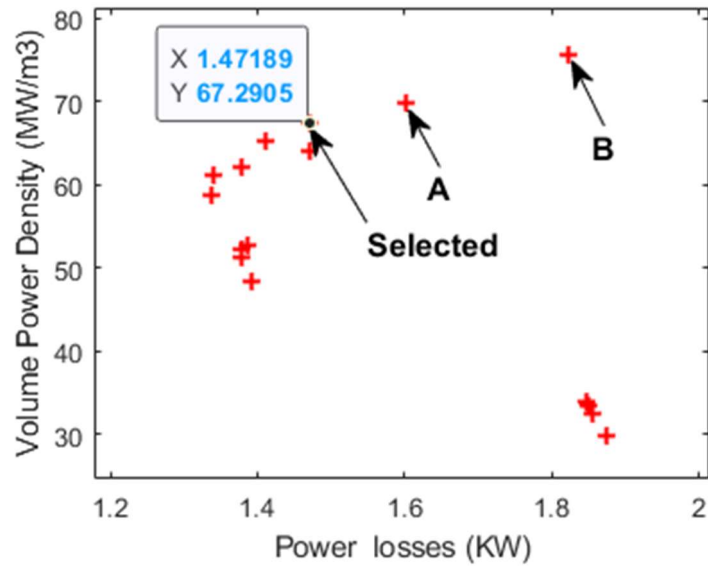


Figure 3.2 Preliminary sensitivity analysis.

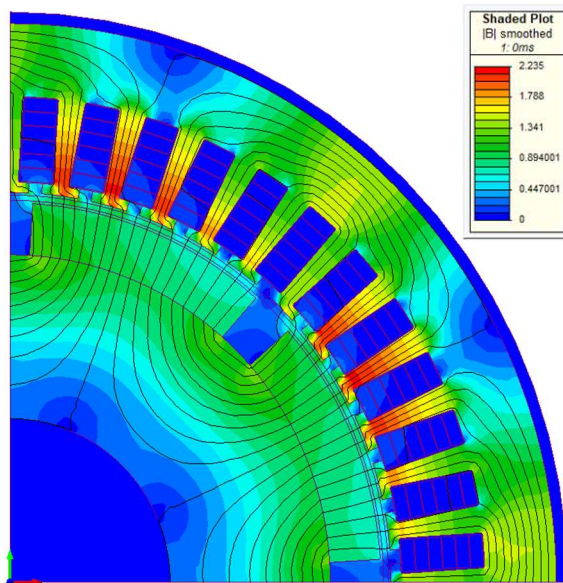


Figure 3.3 FE one pole pair model of the motor with the hairpin winding, highlighting flux density map (T) and field lines distribution at full-load operation.

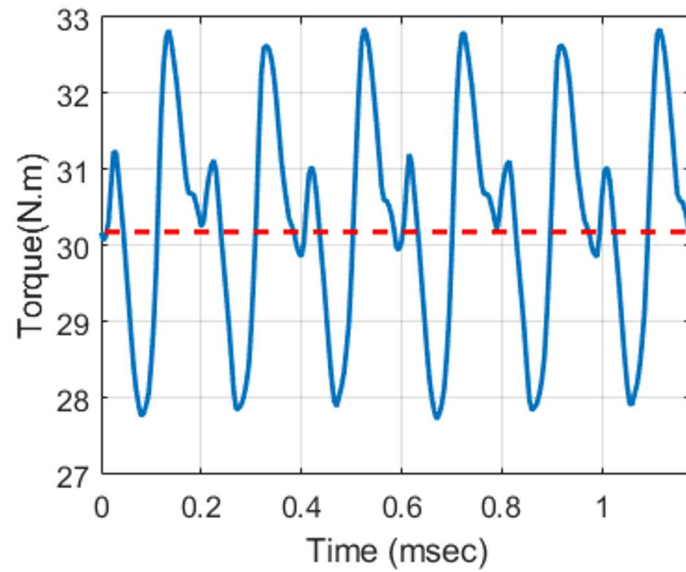


Figure 3.4 Output torque (in blue) and its average value (in red) were obtained via FE analysis.

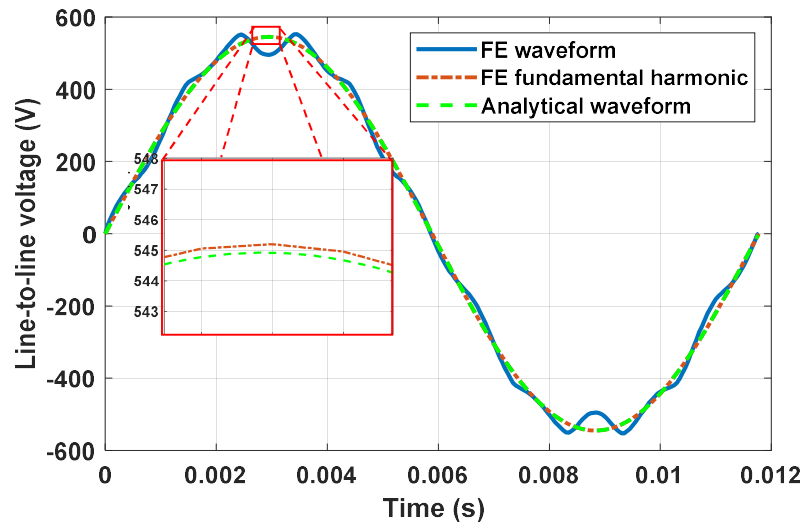


Figure 3.5 FE no-load line-to-line voltage (in blue) and its fundamental harmonic (in red) vs. analytical no-load line-to-line voltage (in green).

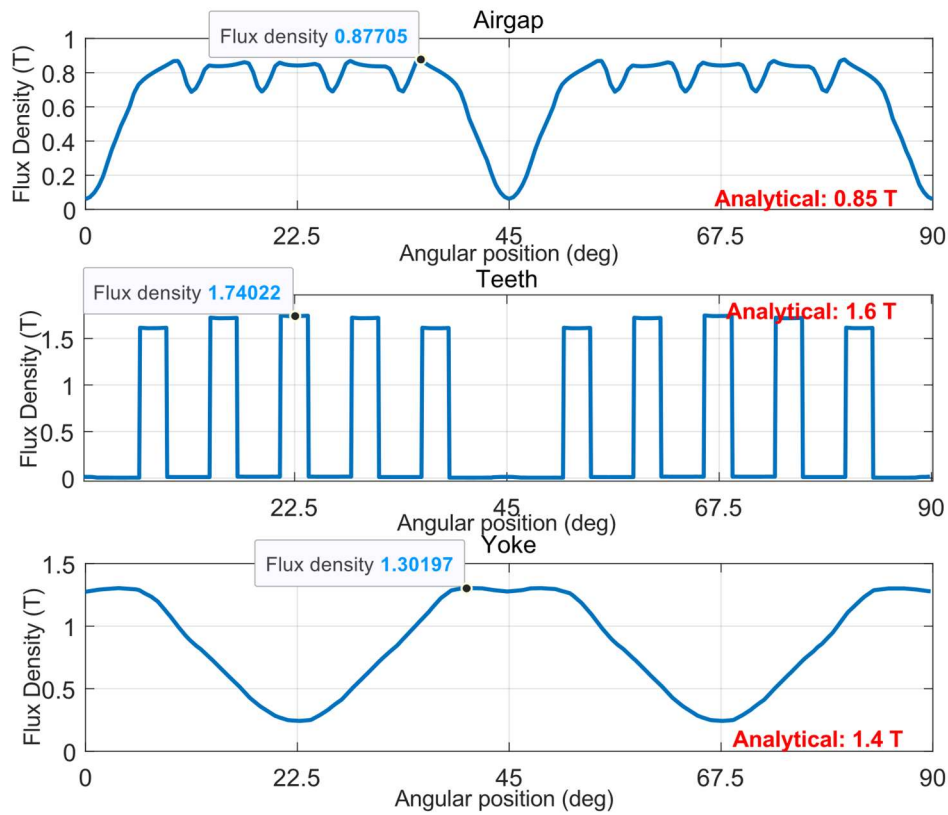


Figure 3.6 Comparison in terms of flux density in the airgap, teeth, and yoke.

### 3.4.2 Effective parameters

Considering the analytical equations reported in chapter 2 for motor design, several parameters can be utilized to achieve the main design objectives of this work, i.e., power density maximization and power loss minimization. Thus, a sensitivity analysis is performed. While the results of this study can vary depending on the power range, the geometrical and magnetic features, the airgap thickness, etc., of the PMSM motor under analysis, for the case study considered in this research the sensitivity study can provide useful information for a first exploration of weight allocation during optimization. Assuming the hairpin motor of the previous section as the benchmark, the parameters used for the sensitivity study are normalized over the corresponding values of the benchmark machine. Figures 7 and 8 show the total power losses and volume power density for the

four input parameters, i.e., pole pair number, slot per pole per phase number, conductor per slot number, and axial length. These parameters are changed “1-by-1” in this first exploration. All the curves meet at 1 p.u., corresponding to the benchmark machine. All the parameters have a non-negligible effect on both power losses (Figure 3.7) and power density (Figure 3.8). According to the methodology described in [58], the weight of each input parameter to be imposed in the optimization can be found through these figures. Using a coefficient equal to 1 for  $N$ , the pole pair number, the slot per pole per phase number and the axial length feature coefficients equal to 1.38, 1.1 and 1.15, respectively.

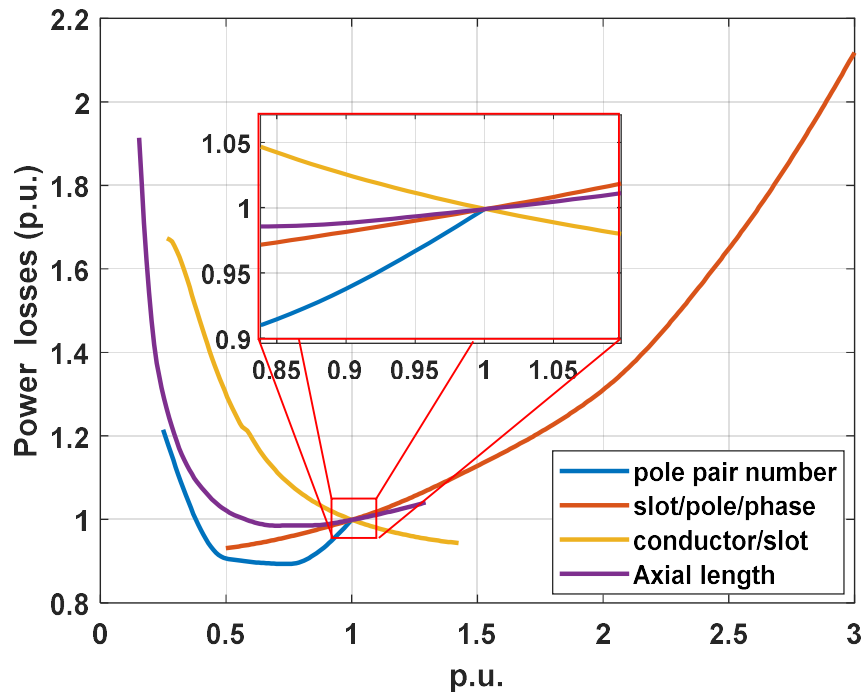


Figure 3.7 Effect of the input parameters on the total power losses.

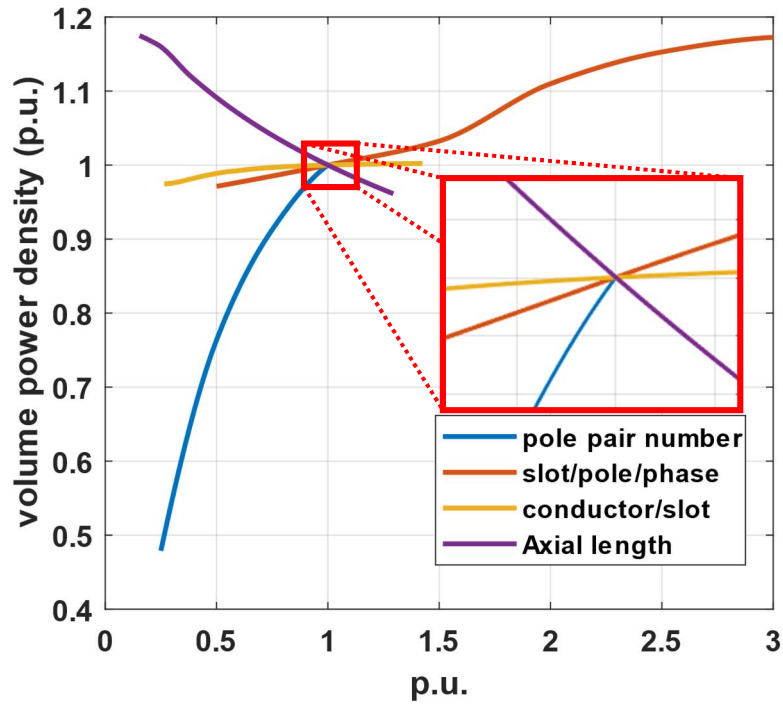


Figure 3.8 Effect of the input parameters on the volume power density.

### 3.4.3 MOEA Results and Comparison

Regarding the mentioned sequential task decomposition of the optimization method (see Figure 1), before any mutation, the constraints (3.1)– (3.4) should be carefully considered. After running the optimization algorithm using 500 generations and 50 individuals per generation, the Pareto front shown in Figure 3.9 is finally obtained, where the last 50 designs are observed. Every sequential task of the optimization process shown in Figure 3.1 has been implemented in the Matlab environment. The optimal machine design is also highlighted in Figure 3.9, and its geometry is illustrated in Figure 3.9b, whereas in Figure 3.9a the machine design resulting from the first sensitivity analysis is shown for the sake of comparison. Table 3.4 compares the analytical results obtained for the motor with round winding designed in [50], the motor with hairpin winding resulting from the first sensitivity analysis, and the optimum one. With a focus on the motors with hairpin windings, the main indexes such as efficiency, volume power

density, volume torque density, and power losses have been improved by 0.15%, 10.55%, 12.3%, and 3.4%, respectively. For completeness, the full-load output torque of the optimum motor obtained using FE is reported in Figure 3.10, with the mean value being highlighted in red and equal to 30.2 Nm. Figure 3.11 shows the comparison between three main characteristics i.e., total power loss, efficiency, mass and volume power densities for equivalent round winding, the first sensitive analysis designed motor and the motor designed with multi-objective optimization. These improvements are highlighted in Table 3.4 in detail.

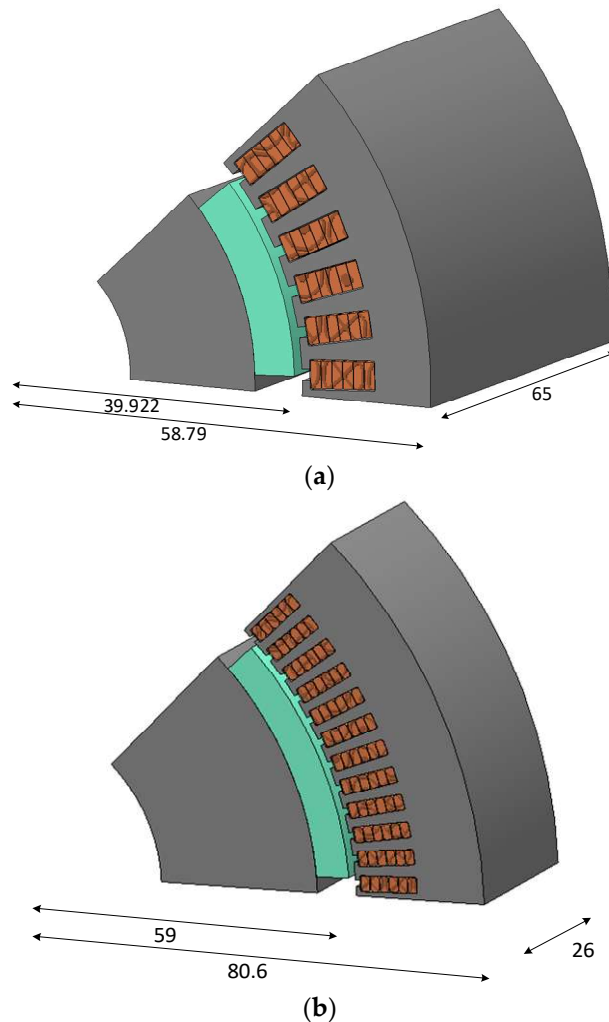


Figure 3.9 Comparison between the geometries of (a) the first analyzed motor and (b) the optimal motor.

Table 3.4 Summarizing comparison among the benchmark motor [50], the hairpin motor obtained through the first sensitivity analysis and the optimum hairpin motor.

Parameters	Round	Hairpin 1st Design	Hairpin Optimal	Improvement
pole number	6	8	8	-
slot/pole/phase	1	2	4	-
axial length	65	65	26	-
conductors/slot)	11	6	6	-
rotor radius	45	39.922	59	-
Tooth width	10	2	1.635	-
Yoke thickness	14	7.7	13.35	-
outer radius	85	58.79	80.6	-
Fill factor	60%	85%	85%	-
Peak current (A)	140	80.56	63.7	-
Torque ripple (%)	16%	17%	8.97%	9.03%
Power loss (kW)	2	1.47	1.42	10.55%,
Efficiency	95.2%	96.45%	96.6%	0.15%
volume power density (MW/m <sup>3</sup> )	16.75	67.3	74.4	12.3%
volume torque density (kNm/m <sup>3</sup> )	13.21	49.65	55.76	3.4%

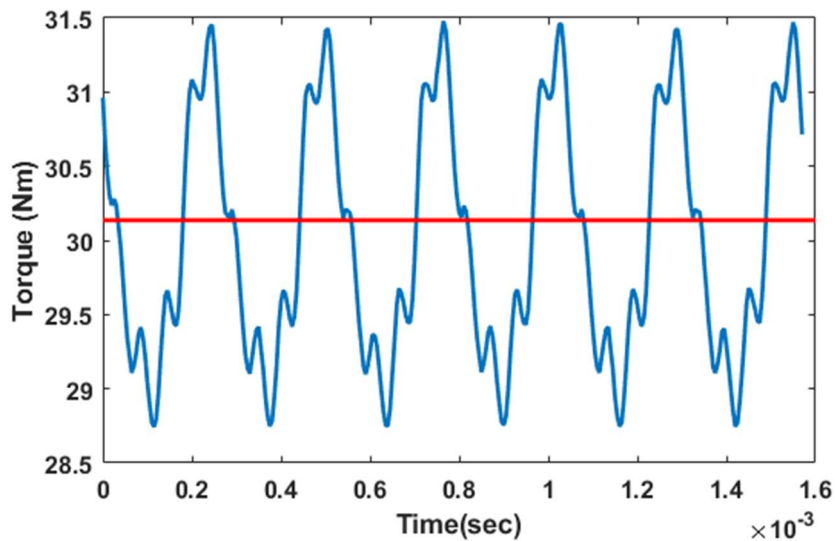


Figure 3.10 Comparison between the geometries of (a) the first analyzed motor and (b) the optimal motor.

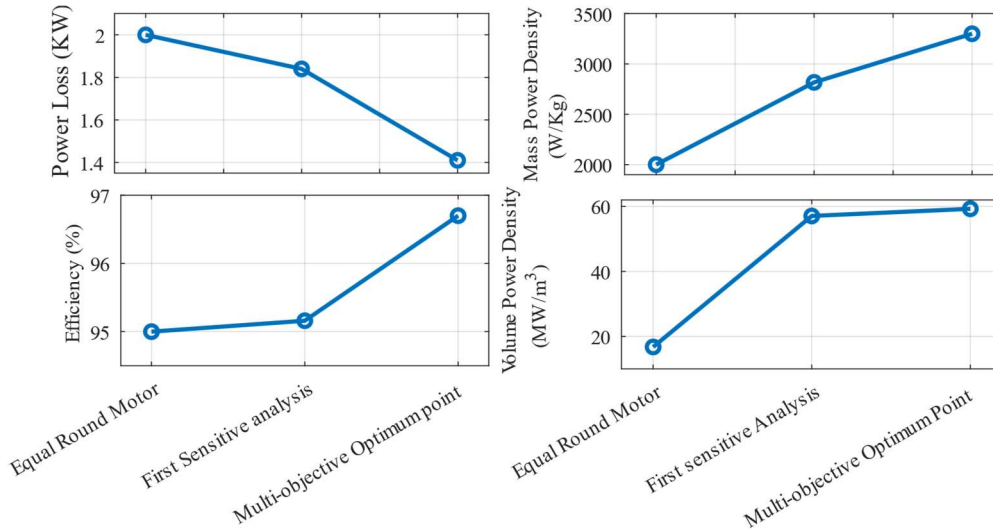


Figure 3.11 Comparison between the main parameters for three designed motors in this chapter

### 3.5 Conclusion

In this chapter, a fast and accurate optimization tool was introduced for the optimal exploitation of hairpin technologies in electrical machines intended for traction applications. The optimization tool is aimed at maximizing power density and efficiency, which are key figures for the application at hand. In addition, given the challenges featured by hairpin conductors at high-frequency operations, these two objectives are rather conflicting, thus making the machine design complex. The optimization strategy, based first on a “one-by-one” sensitivity study and then on the application of a multi-objective evolutionary algorithm, proved that these two objectives can be pursued and achieved simultaneously, with excellent performance enhancement being obtained.

As a benchmark case study, a surface-mounted PMSM equipping random windings previously designed for a Formula SAE car was considered. Therefore, the first exercise consisted of replacing the random winding with hairpin conductors. A preliminary sizing was first carried out based on the requirements of the application at hand. Then, the analytical sizing tool was validated against FE evaluations, with a maximum error of  $\approx 8\%$ , thus making the analytical

equations a safe means for the optimization procedure. A sensitivity analysis was performed to suitably weight the optimization input parameters and, finally, the optimization algorithm was run. The optimal motor, which was selected for comparative purposes against the benchmark motor with random windings and a non-optimal hairpin motor, showed very promising results and significant performance improvements. In particular, the main indexes such as efficiency, volume power density, and power losses, were improved by 0.15%, 10.55%, and 3.4%, respectively.

# Chapter 4

## AC and DC loss Analysis

### 4.1 Introduction

As already mentioned, the hairpin winding's bottleneck is the high ohmic losses at high-frequency operations due to skin and proximity effects (AC losses), resulting in a negative impact on the temperature map of the machine. Nevertheless, while it is well-known that DC losses increase linearly with the operating temperatures, the AC losses trend needs further insight. By using the optimization process introduced in chapter 3 for the design of hairpin winding, this chapter demonstrates that operating the machine at higher temperatures could be beneficial for overall efficiency, especially at high-frequency operations. This suggests that a paradigm shift is required for the design of electric motors equipped with hairpin windings, which should therefore focus on a temperature-oriented approach. In addition, the effect of the rotor topology on AC losses, which is often overlooked, is also considered in this research. The combination of these effects is used to carry out observations and, Analytical and FE models are

first used to assess the high-frequency losses in the proposed winding concept. After providing design recommendations and FE electromagnetic and thermal evaluations, eventually, an experimental test is also performed on a motorette comprising different frequencies and temperatures to prove the findings of this research.

## 4.2 Practical design

In chapter 3, an analytical model was used for optimization purposes, as it presents a reduced computation time as opposed to an FEA. In this chapter, the same analytical model was used, together with the multi-objective optimization, to further improve the surface PMSM. The same objectives were set, i.e., minimization of power loss and maximization of power density as in (2.17). The main difference between the design proposed in chapter 3 and that presented here is that practical considerations were carried out here, while these were previously neglected. First, the fill factor was updated from  $\approx 85\%$  to  $\approx 65\%$ , which is a more realistic value accounting for the conductors' corner radius, the insulation materials with their typical thicknesses, etc. Then, a higher operating frequency was considered, which was obtained by increasing the number of pole pairs from 4 to 5. After the implementation of the MOEA, whose results are reported in the Pareto front of Figure 4.1, a new optimal motor was achieved. This is shown in Figure 4.2 for the sake of completeness. A comparative summary between the optimally designed motor presented in Table 3.4 and the one carried out in the present contribution is shown in Table 4.1. Although the newly assumed fill factor was decreased, the power density and the overall losses (and thus the efficiency) remained basically the same as in the previous design. It is worth mentioning that all the comparative results reported in Table 4.1 were found without considering the end windings, as the estimations of their length, weight, losses, etc., were difficult to estimate analytically. However, the comparative exercise between the two motors is fully consistent. The dimensions analytically obtained were used to

build the machine geometry and a corresponding model within the FE-based software Simcenter MagNet.

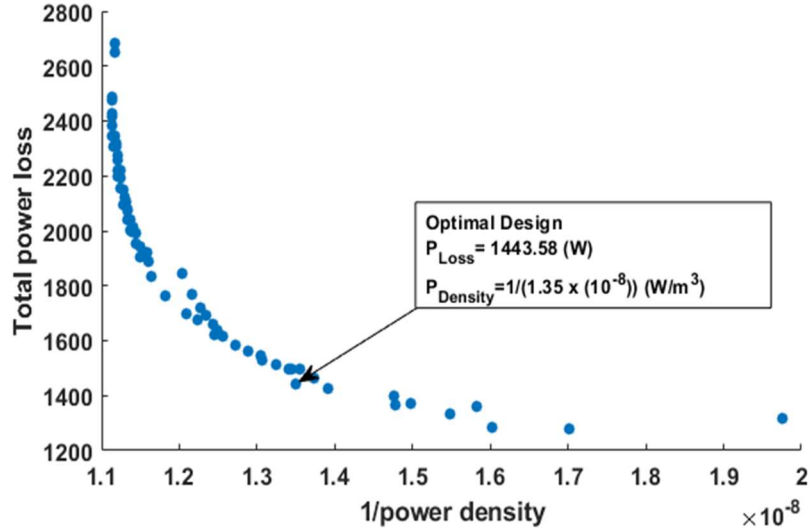


Figure 4.1 Optimization results for the design of the surface PMSM with hairpin winding.

Table 4.1 Design summary of the PMSM and comparison versus the previous design in chapter 3

Parameter	New Optimal Motor	The Motor in [12]
Fill factor (%)	65	85
Outer stator diameter (mm)	173.27	161.2
Rotor diameter (mm)	124.8	118
Axial length (mm)	26	26
Slot-pole-phase	2	4
Pole number	10	8
Number of conductors per slot	6	6
Max. frequency (Hz)	1061.7	849.33
Efficiency (%)	96.1	96.6
Power density ( $MW/m^3$ )	74.1	74.5

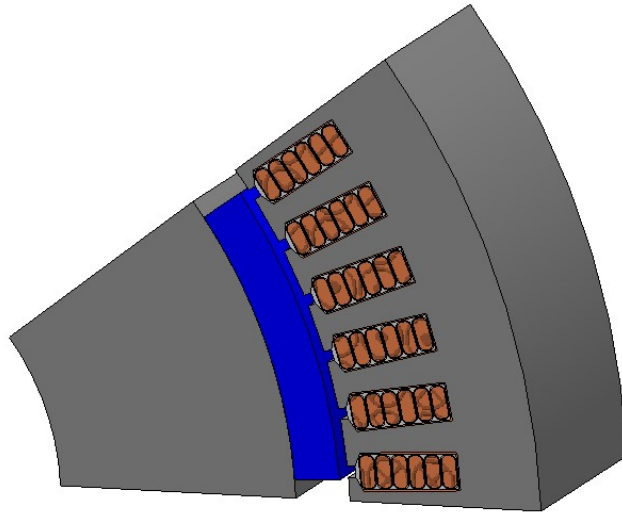


Figure 4.2 The geometry of the newly designed optimal motor.

### 4.3 Analysis of Ohmic Losses versus Temperature

As mentioned in the previous sections, one of the most critical challenges of hairpin windings is the high AC losses in the conductors, with that nearest to the slot opening being the most stressed (see Figure 1.2). This phenomenon is particularly evident at high operating frequencies. While the effect of frequency on AC losses is well-known and studied, the impact of the temperature has not been widely investigated, and thus this is the main target of this section.

First, considering the parameter  $k_{Ru}$ , a value equal to 2 was taken as an acceptable index in terms of the amount of AC losses against DC ones. Considering this, the designed PMSM was analyzed via an FEA model, where the total DC and AC losses in the hairpin conductors were calculated at various frequency values, ranging from 0 Hz to  $\approx 1.75$  kHz. Figure 4.3 shows the DC and AC losses, where the frequency at which  $k_{Ru} = 2$  is highlighted, i.e.,  $\approx 650$  Hz. Furthermore, for the sake of completeness, PM losses and core losses were also evaluated which, added to the ohmic losses, contribute to the total power losses of the machine. These results are plotted in Figure 4.4. It is worth highlighting that these losses were found by considering an ambient temperature of 20 °C. However, all these loss contributions are temperature-dependent, especially the ohmic losses. In fact,

according to (2-8) and (2-9), the electrical resistivity of conductors changes linearly with temperature. It was therefore expected that, when the steady-state temperature was imposed on the conductors, the DC power loss would increase. In contrast, as (2.13), the AC losses would not increase linearly as the AC resistance depends on the current distribution, and thus the overall losses at the steady-state temperature should be carefully investigated.

Therefore, a thermal analysis was carried out considering the power losses found through the FEA (see Figures 4 and 5). The FE-based software Simcenter MagNet Thermal was used for such purposes. Nomex 430 was used as slot insulation, while Kapton was used as conductor insulation [59], and the slot was filled with Epoxy resin. Furthermore, as boundary conditions, the outer stator environment was covered by a water jacket at a temperature of 50 °C, an additional convective heat transfer coefficient of 100 W/ (m<sup>2</sup>. °C) was assumed for the airgap, and a perfect insulator was considered for the shaft. Figure 4.5 illustrates the temperature map of the designed surface PMSM. It is worth highlighting that, although the PM temperature was ≈120 °C, no demagnetization challenges were expected as the selected PMs have the demagnetization knee in the third quadrant of the B-H curve up to 150 °C.

All the temperatures in the various parts of the machine were then recorded and transferred to the electromagnetic FEA model to calculate the losses at such temperatures, which are considered steady-state ones. As expected, the DC loss in the motor at steady-state was higher than that at ambient temperature, as observed in Figure 4.6. Compared to the ambient case, the DC loss increased by ≈50%, but the slope of AC losses (red line) decreased by ≈45% when a linear approximation was performed around the point where  $k_{Ru} = 2$ . This resulted in an increase of the frequency value at which the AC-to-DC loss ratio,  $k_{Ru}$ , was equal to 2, i.e., it went from ≈650 (at ambient temperature) to ≈1200 Hz (at steady-state temperature). The changes in the core and PM losses from ambient to steady-state were not significant. Therefore, the total power loss significantly depends on ohmic losses.

Figure 4-7 shows the total power losses in both conditions. In fact, it informs that the total power losses at the thermal steady state were higher than those at ambient temperature up to  $\approx 640$  Hz, where the intersection between the two curves occurred (see point 'M' in the figure). Above this intersection point, the total power losses at steady-state temperature become lower than those at ambient conditions. This finding leads to conclude that the operating temperature can play a very important role in the overall losses in hairpin windings, thus suggesting that a “temperature-oriented” motor design could enable higher efficiency levels in such types of electrical machines.

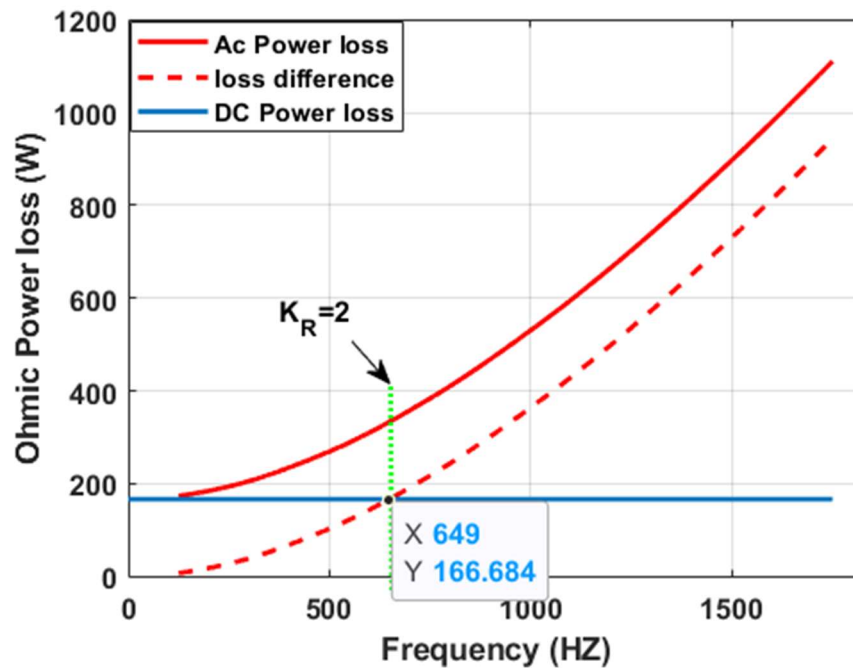


Figure 4.3 DC and AC losses versus frequency at ambient temperature (20 °C).

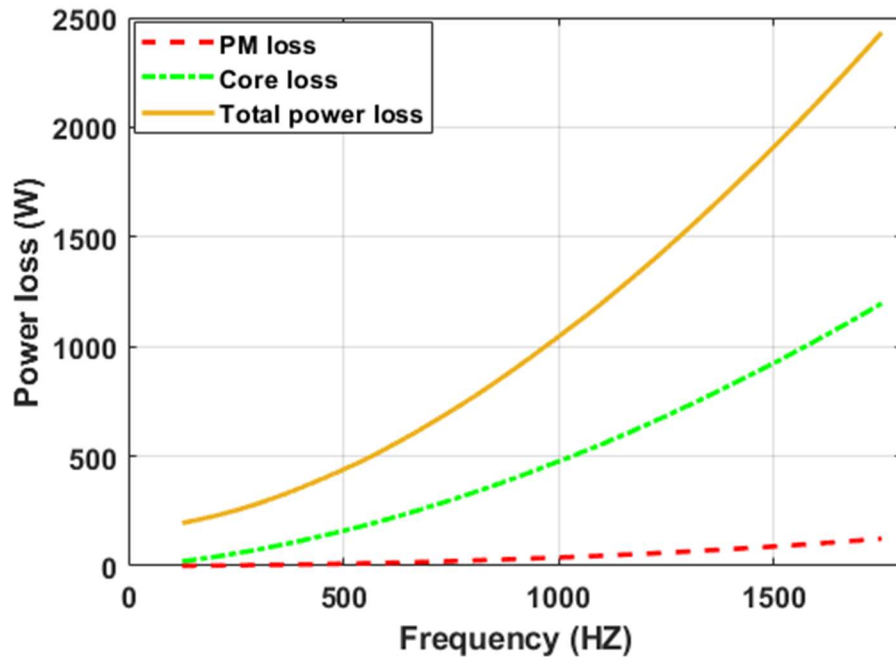


Figure 4.4 PMs, core, and total losses versus frequency at ambient temperature (20 °C).

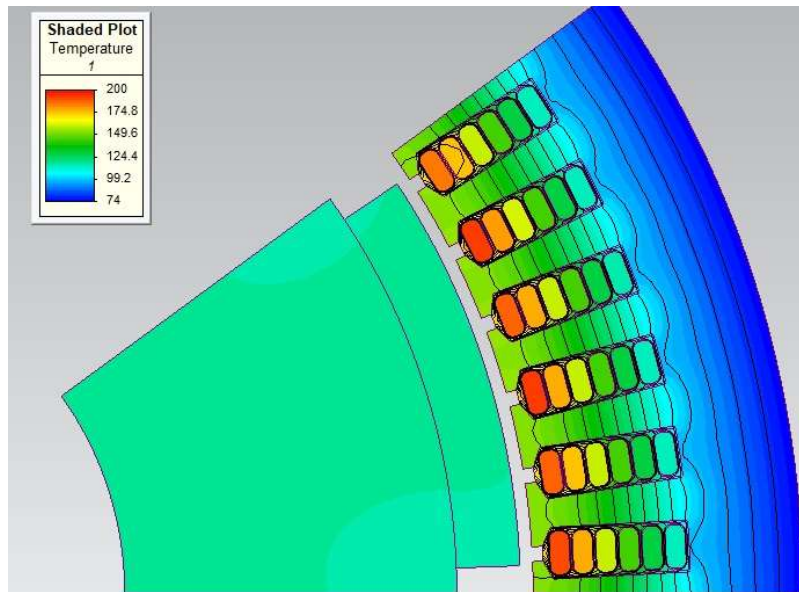


Figure 4.5 The FEA temperature map of the considered surface PMSM.

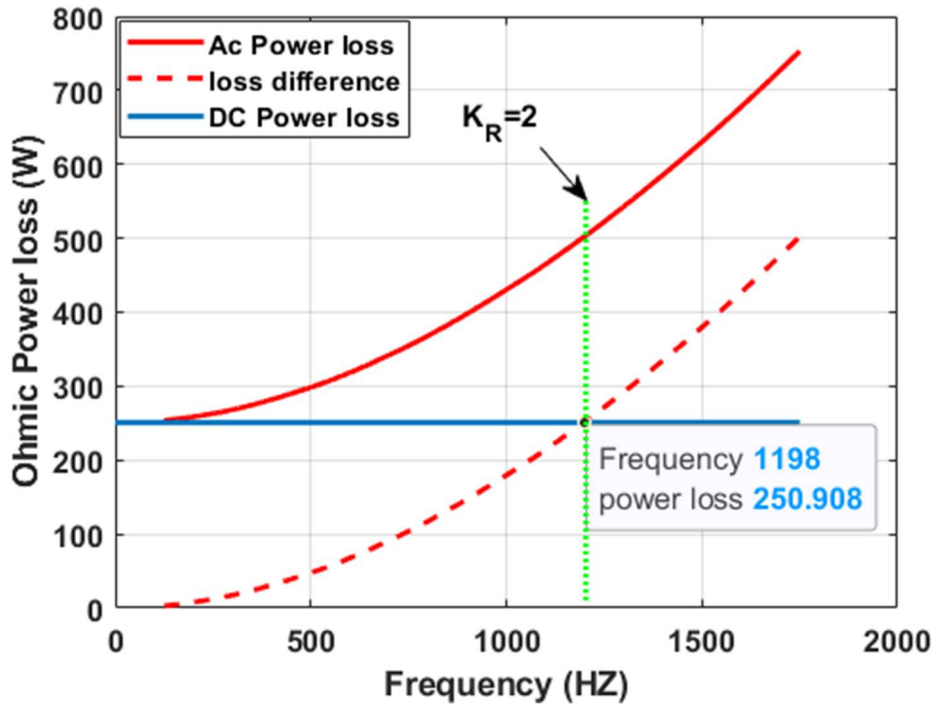


Figure 4.6 DC and AC losses versus frequency at the steady-state temperature.

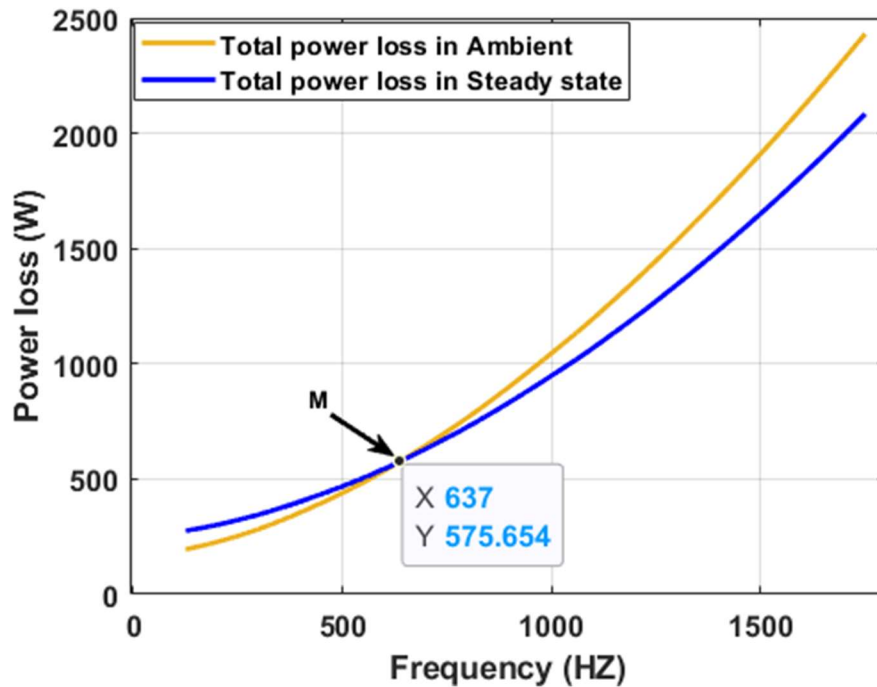


Figure 4.7 Comparison in terms of total losses versus frequency between ambient and steady-state temperature operation.

## 4.4 Analysis of Losses versus Rotor Topologies

### 4.4.1 Ohmic Losses versus Different Rotor Topologies

Besides the phenomena related to the temperature, another important aspect which is often overlooked when analyzing losses in hairpin windings is the effect of the rotor field. In this section, an analysis is carried out considering different rotor topologies while keeping the same stator as the designed PMSM. Figure 4.8 shows the four-rotor topologies investigated, where the PM volume was kept the same as the surface case. As seen, Topology 2 (Figure 4.8a) and Topology 3 (Figure 4.8b) were directly obtained from the surface layout (namely Topology 1) by embedding the magnets into the core. Figure 4.8c shows an interior PM rotor with the classical V shape (Topology 4), while Figure 4.8d shows an interior PM rotor with the classical  $\Delta$  shape (Topology 5). It is worth mentioning that these topologies are not optimized as this would be out of the scope of this research. The four considered topologies were investigated using the existing electromagnetic FEA model as per the surface PMSM. Figure 4.9 shows PM loss, total ohmic loss, and core loss versus frequency for the five rotor topologies. The temperature, initially, was set at the assumed ambient value of 20 °C. Topologies 4 and 5 featured lower overall losses, while Topology 2 was the one with higher losses, especially those in the core. This is true at any studied frequency value. It is also possible to observe that the motor frequency had no significant effect on PM losses in Topologies 3, 4, and 5. Concerning ohmic losses, Topologies 1 and 2 had no differences, while Topologies 3, 4, and 5 had a non-negligible effect, with the last one being the more efficient. In summary, focusing on the ohmic losses and taking as an example the losses at 800 Hz, the difference between Topology 1 and Topology 5 was 27.8%, thus proving that these aspects cannot be neglected in machines equipping hairpin windings. For the sake of completeness, the field maps at full-load conditions for all five topologies at 800 Hz are illustrated in Figure 4.9.

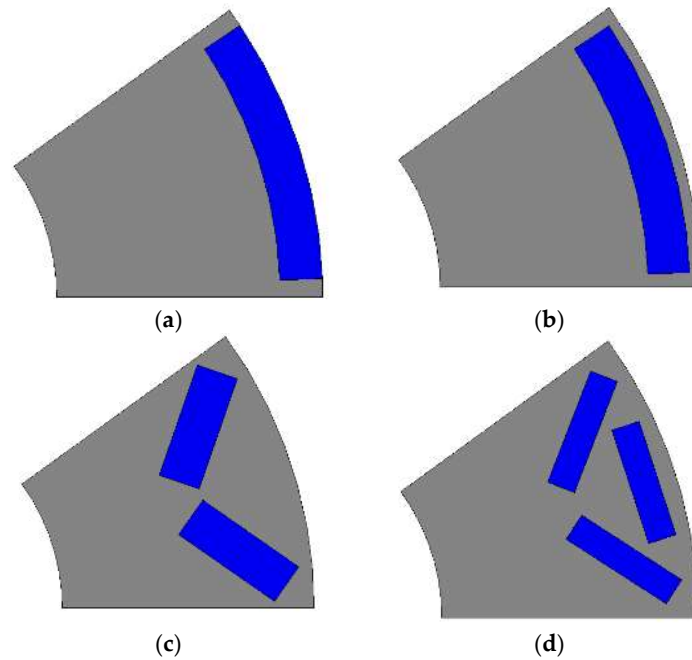


Figure 4.8 Rotor topologies: (a) Topology 2, (b) Topology 3, (c) Topology 4, and (d) Topology 5.

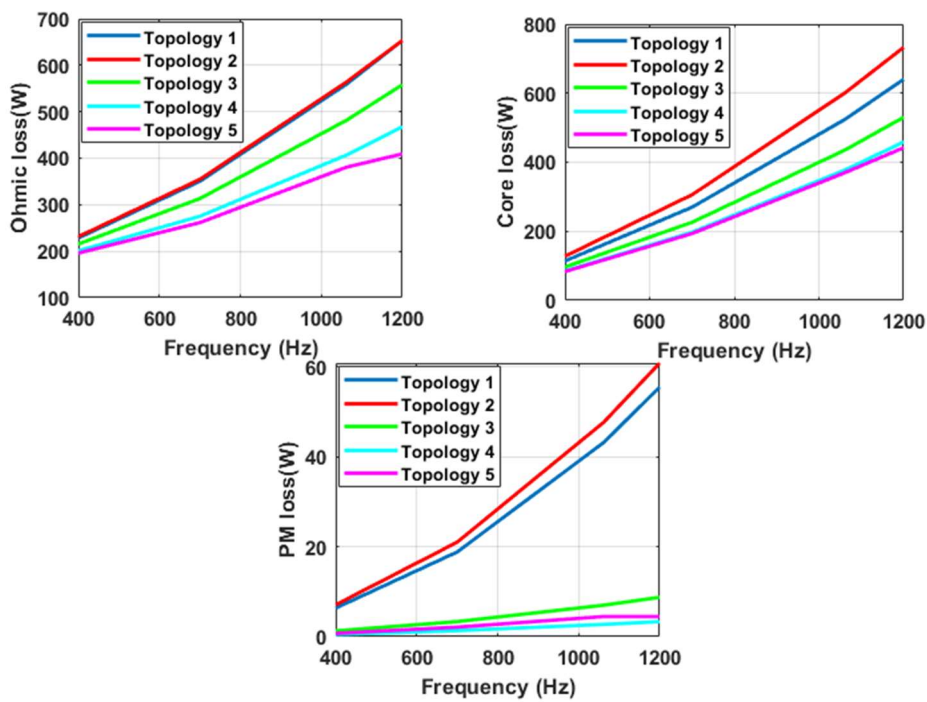


Figure 4.9 Comparison in terms of losses versus frequency among the five topologies considered.

#### 4.4.2 Analysis of Ohmic Losses versus Both Temperature and Rotor Topologies

In this last section, the comparison among the rotor topologies is carried out considering the steady-state operating temperatures of the machines. To do so, the same procedure performed in Section 4 for Topology 1 was also carried out for the remaining four topologies. This consisted of running a thermal analysis using the losses at 20 °C, obtaining an accurate temperature map, and recalculating the losses at these (steady state) temperatures. Figure 4.10 illustrates the DC power losses at ambient and steady-state temperature conditions for the five different rotor topologies. For Topology 1, the amount of DC loss was equal to that in Figures 4.3 and 4.6. The DC losses at ambient temperature were the same for all the topologies, as expected. On the other hand, a non-negligible difference was registered at steady-state temperature due to the different steady-state temperatures among the topologies. In Figure 4.11 the curves equivalent to Figure 4.7 for the other four topologies and their intersection points could be seen.

Figure 4.12 shows, for all five topologies, three frequency values: (1) the frequency at which  $k_{Ru} = 2$  at ambient temperature, (2) the frequency at which  $k_{Ru} = 2$  at steady-state temperature, and (3) the frequency intersection point where the total ohmic losses at steady-state temperature become lower than those at ambient temperature. It can be observed that this intersection point changed from one topology to another.

In particular, the interior PM rotor layouts (Topologies 4 and 5) presented a higher-frequency intersection point, thus highlighting reduced room for improvement when a temperature-oriented design was adopted. For the sake of completeness, Figure 4.13 shows the current density maps for all five topologies at their corresponding frequency intersection points. Figure 4.14 reports the instantaneous current density in the conductors within one slot, considering the worst-case scenario. Topologies 4 and 5 present higher values of current density

for the conductors closest to the slot opening (first, second, and third conductors), whereas they feature lower current density values in the remaining ones.

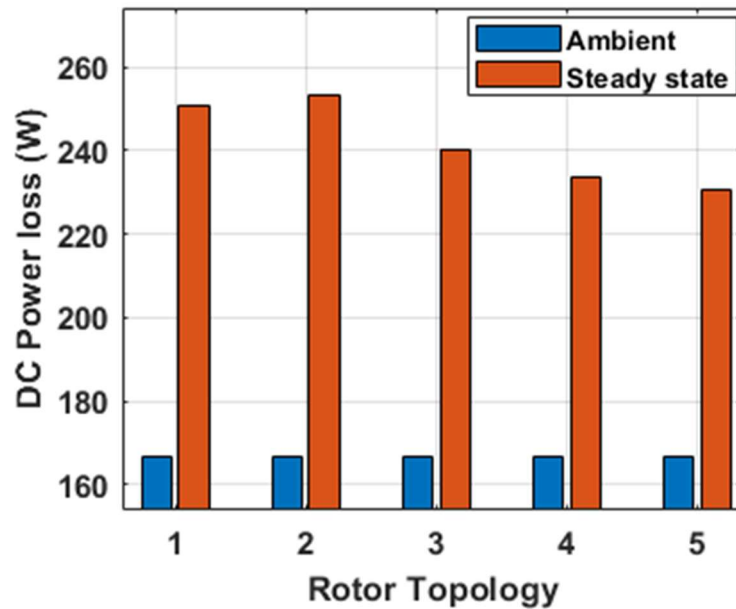


Figure 4.10 Comparison in terms of DC power losses among the five considered topologies, at both ambient and steady-state temperature conditions.

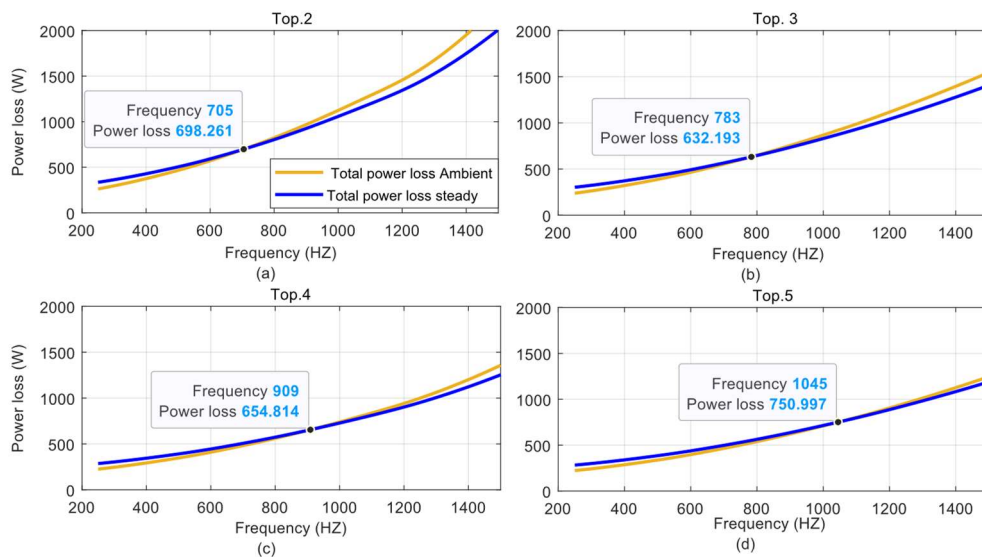


Figure 4.11 Comparison in terms of total losses versus frequency between ambient and steady-state temperature operations for all investigated topologies

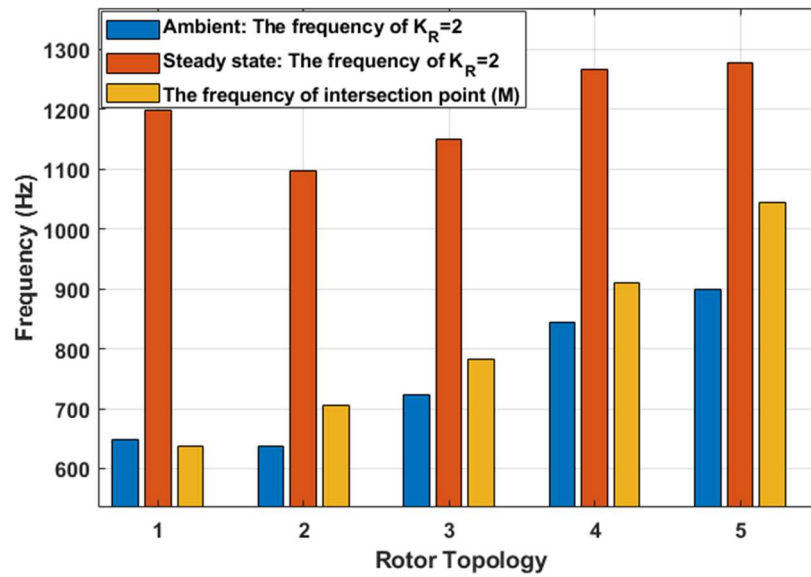
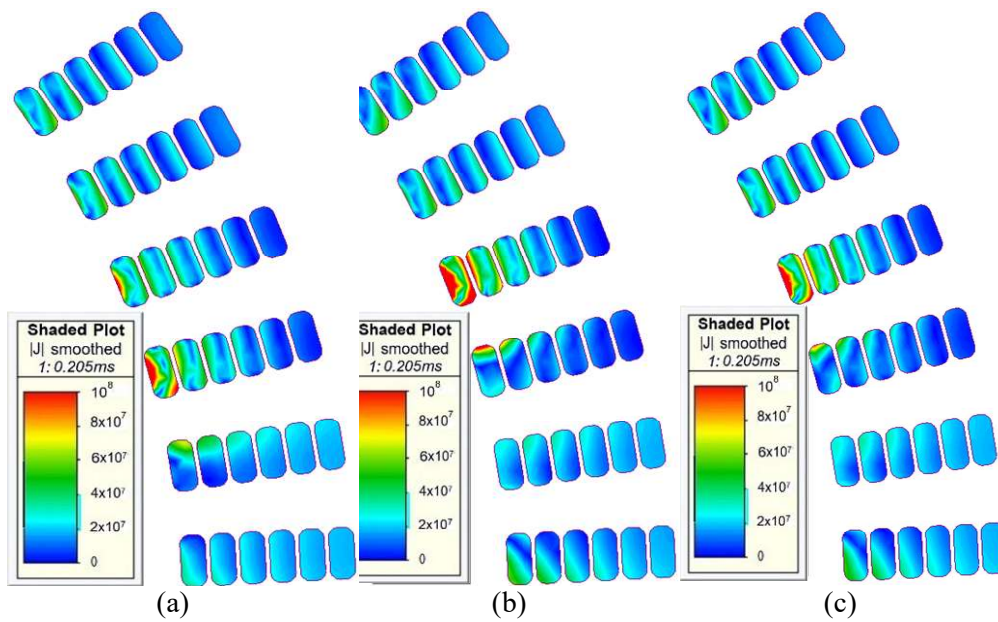


Figure 4.12 Comparison among the five considered topologies in terms of (1) the frequency at which  $k_{Ru} = 2$  at ambient temperature (in blue), (2) the frequency at which  $k_{Ru} = 2$  at steady-state temperature (in red), and (3) the frequency of intersection point where the total ohmic losses at steady-state temperature become lower than those at ambient temperature (in yellow).



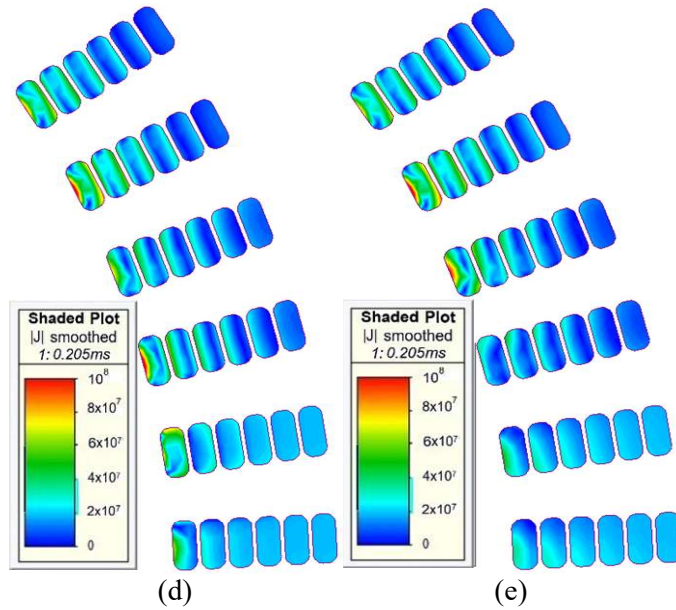


Figure 4.13 Instantaneous current density at the intersection frequency point in steady-state condition for the five rotor topologies, (a)First topology (SMPMSM), (b) Second topology, (c) Third topology (magnets embedded in the core), (d) fourth topology (the classical V shape), fifth topology (the classical  $\Delta$  shape).

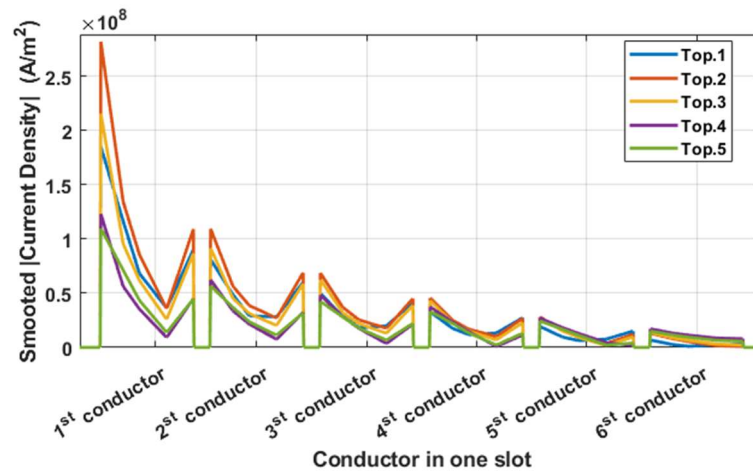


Figure 4.14 Instantaneous current density in the conductors within one slot of all five considered topologies, in the worst-case scenario.

### 4.5 Experimental test

As seen in Figure 4.7, the total loss at higher temperatures is lower than in ambient conditions. To validate the above findings, an experimental campaign is

carried out on a motorette wound with one-phase winding, made by pre-formed conductors emulating the hairpin winding. A picture of the motorette is shown in Figure 4.17. The motorette is manually wound for the sake of simplicity, i.e., to minimize costs, resulting in oversized end-windings as observed in the figure. Detailed specific parameters for the Motorette are in Table 4.3.



Figure 4.15 Motorette wound as  $q=2$  as load equipped with hairpin

Table 4.2 Motorette's specific parameters used as a load for the test

Parameters	Description
Stator Inner Radius (mm)	70
Stator Outer Radius (mm)	111
Stack length (mm)	92
Slot width (mm)	9.1
Slot height (mm)	23
Conductor width (mm)	8.2
Conductor height (mm)	8.3
Slot per pole per phase	2

For the sake of consistency with the sinusoidal supply assumptions used in both analytical and FE evaluations, the signal feeding the motorette is first produced by a SiC voltage pulse generator with a 60 kHz switching frequency and then, filtered by a low pass LC filter with a cut-off frequency at 2 kHz to obtain an output signal as close as possible to a pure sinusoidal waveform. The power loss is measured by a precision power analyzer (PPA 5530) and an oscilloscope is used to double-check the losses value and the signal waveforms. All measurements are taken at the same temperatures which are set by the thermal chamber used for this purpose. The whole test setup is shown in Figure 4.18 where the power analyser and oscilloscope, and the tests are performed at various frequency values. As an example, Figure 4.19 shows the current waveform which has a THD equal to 1.79% at 200Hz, which confirms that assuming a sinusoidal distribution is rather reasonable.

Table 4.4 illustrates the results which have been achieved from the precision power analyser at different frequencies and temperatures. It can be observed that, for the highest frequency values (up to 1.2 kHz), the ohmic loss at low temperatures is higher than that at higher temperatures, as per the FE results reported in the previous sections (see Fig. 4.7). With the simulation of the motorette in the FE-based MagNet software, the ohmic loss at different temperatures and frequency values is shown in Figure 4.20a. It can be observed that the power loss curves have a crossing point at 246 Hz. The result from the experimental setup (Table 4.4) is illustrated in Figure 4.20b that the intersection point is around 230 Hz. Therefore, in addition to confirming the simulation results with a relatively slight error of 6 %, it physically and quantitatively justifies the results of the motor ohmic loss curves.

Table 4.3 Power loss (W) results achieved from the experimental test bench at different frequencies and temperatures.

Temperature (°C)	20	50	80	100	120
<b>Frequency (Hz)</b>					
0	0.46	0.52	0.57	0.6	0.61
200	0.576	0.595	0.605	0.611	0.618
250	0.6912	0.674	0.651	0.637	0.626
500	1.4112	1.376	1.321	1.301	1.279
1000	3.0528	2.978	2.876	2.815	2.767
1200	3.7152	3.624	3.511	3.426	3.368

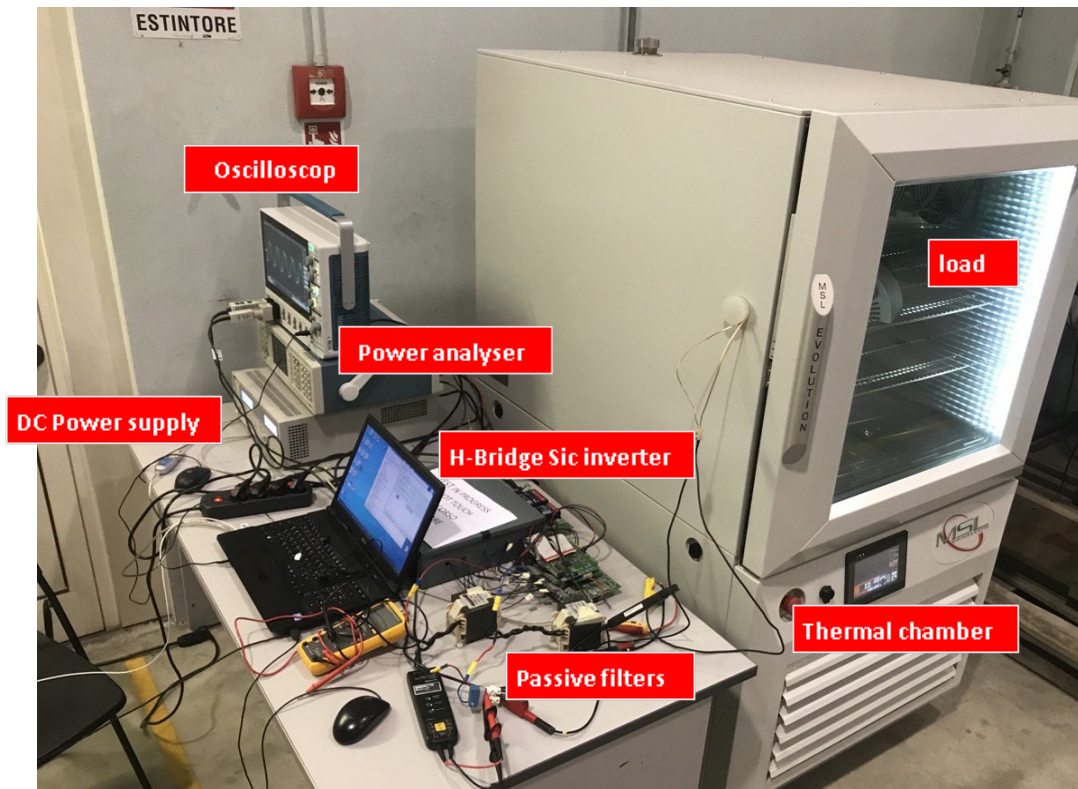


Figure 4.16 Experimental setup testbench

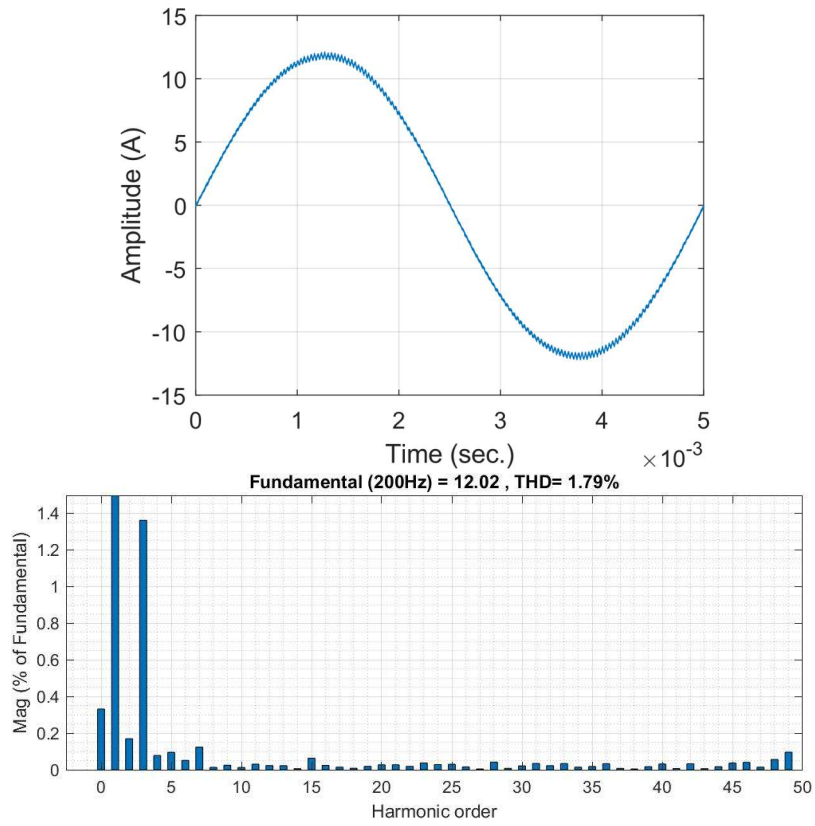
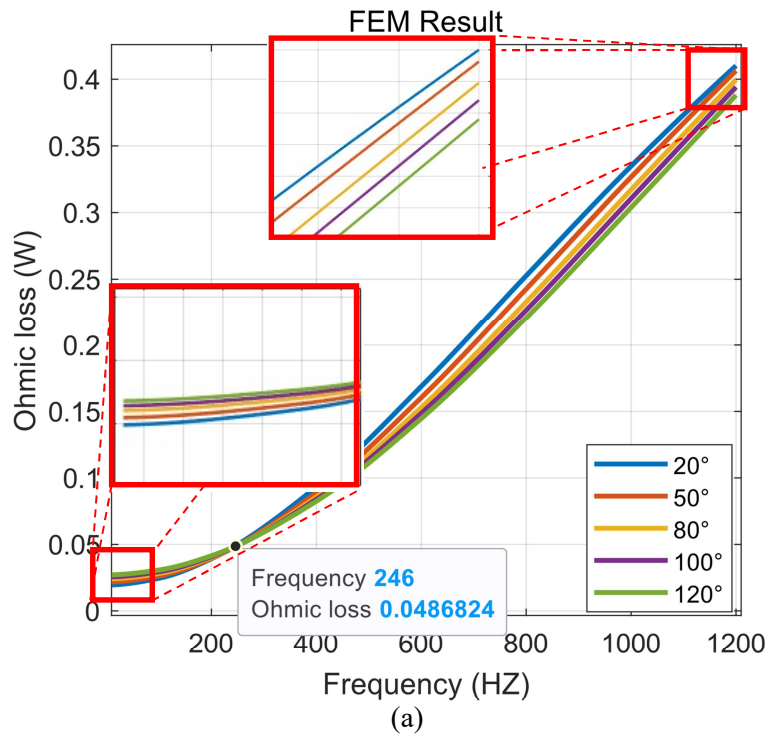


Figure 4.17 Current waveform and its amplitude harmonic spectrum at 200Hz



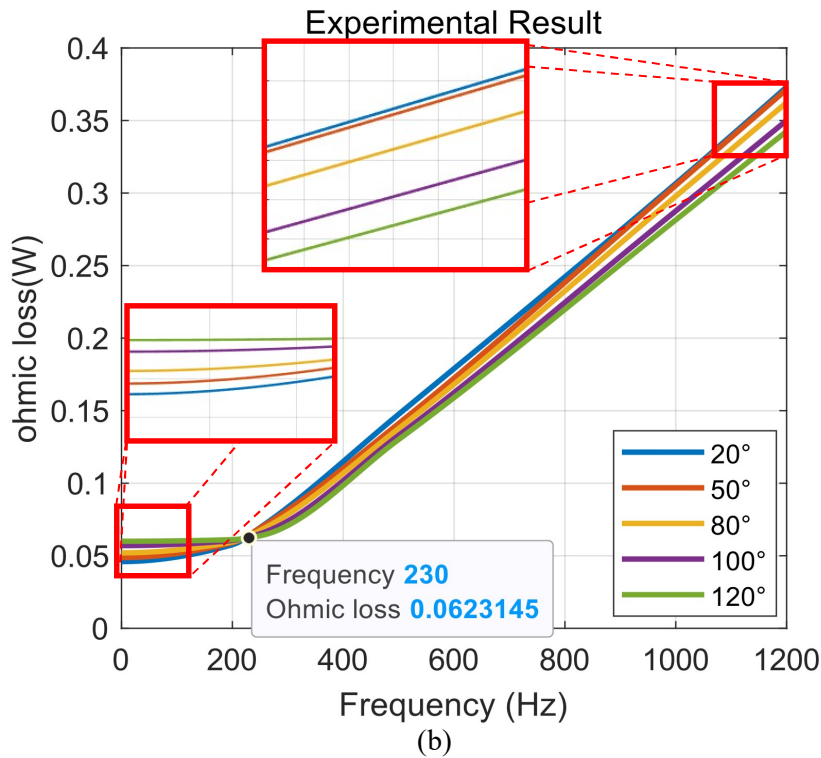


Figure 4.18 Ohmic power loss of motorette in five different temperatures (a) FEM result (b) Experimental result

## 4.6 Conclusion

In this section, the focus was on ohmic losses in hairpin windings. The effects of both operating temperatures and rotor topologies were analyzed in detail, taking a surface-mounted PMSM intended for racing car applications as a case study.

The methodology consisted in:

- (1) Evaluating the loss performance of the considered motor at an assumed ambient temperature of 20 °C via the electromagnetic FEA model.
- (2) Evaluating the temperature map of the considered motor via the thermal FEA model considering the losses determined in (1).
- (3) Evaluating the loss performance of the considered motor via the electromagnetic FEA model at the temperatures determined in (2).
- (4) Repeating the above tasks for motors featuring different rotor topologies.

The main outcomes of this research are summarized in Figures 4.7 and 4.12, where it can be seen that there exists a frequency value at which the losses at higher temperatures than the ambient ones are lower. This is especially true for the benchmark case study, where this frequency value was equal to 637 Hz. A higher frequency value was found for the other four rotor topologies investigated, i.e., 704.7, 782.44, 909.25, and 1045.25 Hz, but still higher operating temperatures seem to be beneficial when AC losses are involved. The findings of this research indicated that a temperature-oriented design process for machines equipping hairpin conductors would be worthwhile in the context of reducing AC losses in this winding technology. To experimentally validate these findings, a motorette has been tested with different frequencies and temperatures. Besides the experimental results that validated the accuracy of the simulation results on the motorette, it justified the high-frequency behaviour of the AC loss of the motor at the ambient and steady-state conditions in different frequencies.

# Chapter 5

## Continuous Hairpin winding

### 5.1 Introduction

One of the challenges of hairpin windings is the high number of welding spots needed for guaranteeing the electric continuity among conductors. This also makes the welding process critical from a reliability point of view. One possible solution could be adopting continuous hairpin windings. However, these result in open slot designs or special stator arrangements, which can produce undesirable effects in motors, such as ripple torque, increased permanent magnet losses, etc. This chapter aims at comparing the main electromagnetic performance metrics for a conventional hairpin winding, wound onto a benchmark stator with a semi-closed slot opening design, and a continuous hairpin winding, where the slot opening is open. Finally, the adoption of semi-magnetic slot wedges is investigated and aimed at improving overall motor performance.

### 5.2 The benchmark motor

The EM which is used as a benchmark for the investigations of this research is a 3-pole pair interior permanent magnet (IPM) synchronous motor preliminary designed at the University of Nottingham. An angular sector of a 2D cross-section of this motor is seen in Figure 5.1, where the main rotor and stator features can be observed. The number of slots per pole per phase is 4 and the number of conductors per slot is 8. The material used for the stator and rotor cores is NO20, while N42UH is the permanent magnet material. The active stack length is 80mm,

the outer diameter is 200mm and the airgap thickness is 1mm. The assumed rated and overload current density values are 10 and 20 Arms/mm<sup>2</sup> respectively. The base and maximum speeds are 5500rpm and 18000rpm. Figure 5.2a shows the slot opening geometry of the benchmark motor, while Figure 5.2b and 2c respectively show the open slot opening without and with M-W, aimed at hosting the continuous hairpin winding.

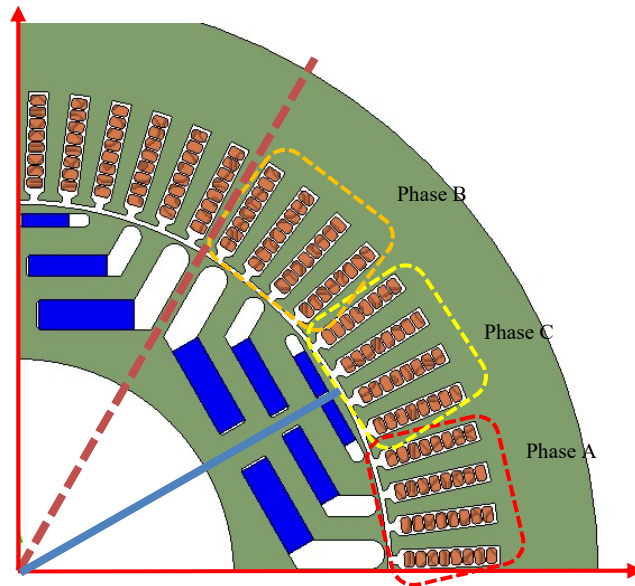


Figure 5.1 An angular sector of a 2D cross-section of the benchmark motor.

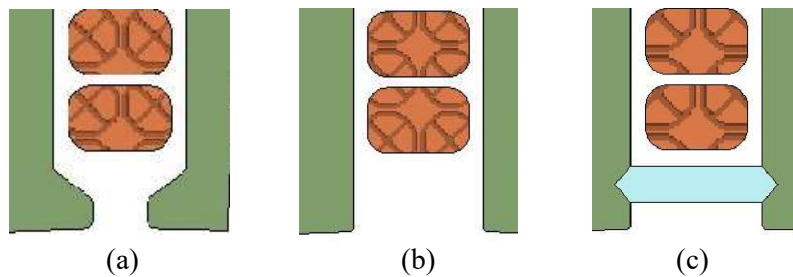


Figure 5.2 The slot opening geometry: a) semi-closed, (b) open, (c) open with M-W.

## 5.3 Conventional vs. continuous hairpin winding performance comparison

### 5.3.1 First rotor position

In this section, a comparison is carried out between the benchmark motor equipping a conventional hairpin winding (i.e., with a semi-closed slot opening) and the modified motor with an open slot opening and continuous hairpin winding. The comparison is made considering the main electromagnetic performance only, i.e., those which are expected to be most sensitive to the change from semi-closed to open slot opening. In other words, average torque and torque ripple vs. loading and current angle are studied. In particular, the loading is modified ranging from no-load to maximum overload capability (i.e. from 0 p.u. to 2 p.u.) and the current angle from  $0^\circ$  to  $90^\circ$ , corresponding to the combinations  $I_q=I_L, I_d=0$  and  $I_q=0, I_d=I_L$ , respectively. The above  $I_d$  and  $I_q$  symbols refer to the d-axis and q-axis currents respectively, while  $I_L$  is the current value referring to a specific load condition.

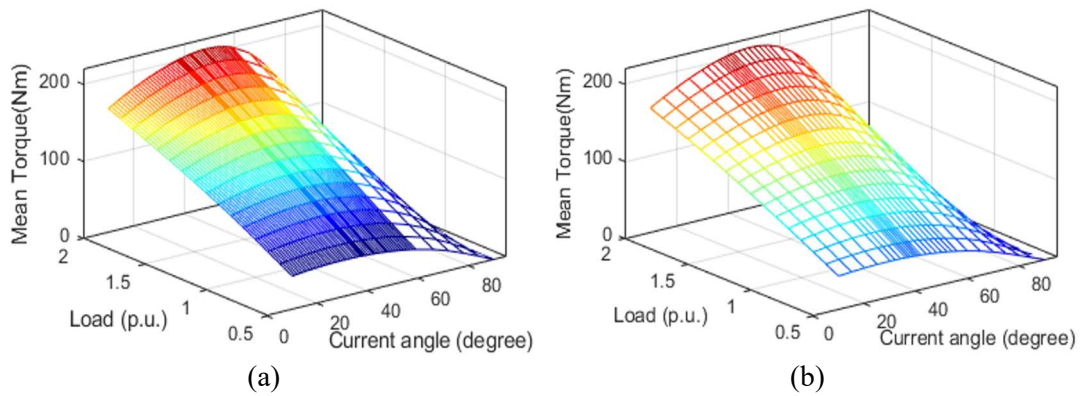
Based on the FE model shown in Figure 5.1 and built in Magnet software, the results relative to the mean torque vs. loading and current angle are shown in Figure 5.3a for the motor with the semi-closed slot (conventional hairpin winding), and in Figure 5.3b for the motor with the open slot (continuous hairpin winding). For better clarity, the torque maps for both motors are reported in Figure 5.3c and Figure 5.3d, where the torque values are highlighted at rated load conditions (1 p.u.) and at a current angle which maximises the output torque. A small difference is registered, while the whole set of differences at various loads and at maximum torque operation are reported in Table 5.1, where the deviation ranges from 0.12% to 1.88%, confirming the limited impact of opening the slot on the output torque.

In Figure 5.4a and Figure 5.4b, the torque ripple in % is plotted vs. current angle and loading for the motors with semi-closed slot and open slot, respectively. As

expected, the impact on the torque ripple is significant. For example, as reported in Figure 5.4, at 1 p.u. load, the torque ripple increases from  $\approx 11.9\%$  to  $\approx 19.3\%$  when moving from the semi-closed slot design to an open one. Therefore, a continuous hairpin winding layout may significantly deteriorate this performance metric. In Table 5.1, these differences are referring to the control angle related to the Maximum mean torque value for any load value.

Figure 5.5 shows the differences in % in terms of torque ripple between the motor with a semi-closed slot opening and that with an open slot opening. It can be noticed that, as expected, the torque ripple for the semi-closed slot opening design is smaller than the open slot design for most of the analysed loading conditions and current angles (positive values of the torque ripple difference).

However, under heavy loading operations ( $>1$ p.u.) and high values of the current angles, the trend is inverted (negative values of the torque ripple difference) due to saturation.



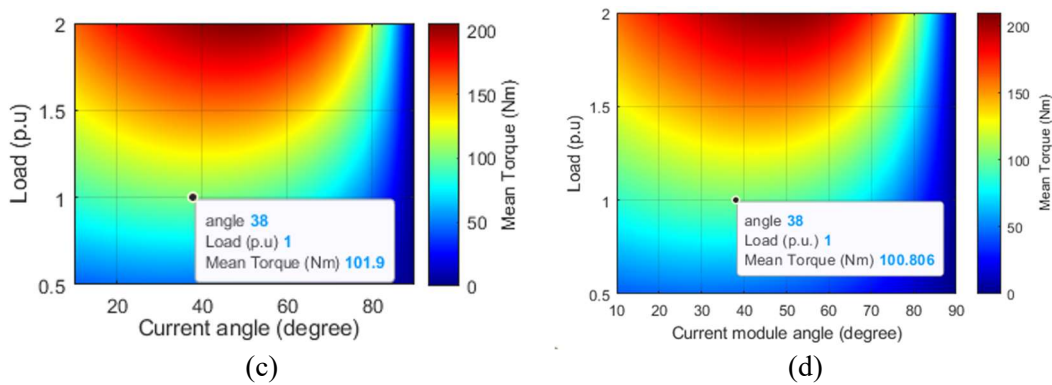


Figure 5.3 3D mean torque values vs. current angle and loading for the motor with (a) a semi-closed slot, (b) an open slot; (c) mean torque heat map for the motor with a semi-closed slot and (d) with an open slot.

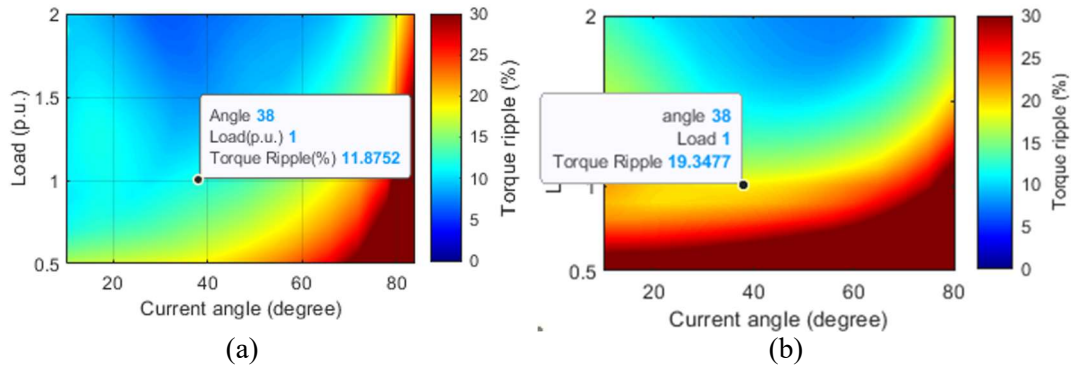


Figure 5.4 Torque ripple heat map vs. current angle and loading for the motor with (a) semi-closed slot and (b) open slot.

Table 5.1 Maximum mean torque value and their control angles for both semi-open slot and open slot

Load (p.u)	0.5	0.6	0.7	0.8	0.9	1	1.1	1.2	1.3	1.4	1.5	1.6	1.7	1.8	1.9	2
<b>For the semi-open slot stator</b>																
Angle (°)	30	33	35	35	38	38	39	40	42	43	44	45	46	47	48	49
Max. T	47.8	58.5	69.3	80.1	91	101.9	112.6	123.5	134.3	144.8	155.5	165.8	176.1	186.3	196.4	206.3
<b>For the open slot stator</b>																
Angle (°)	30	30	32	34	36	38	39	41	42	42	44	44	46	46	48	48
Max. T	46.9	57.5	68.2	79	90	100.8	111.5	122.4	133.3	144.2	155.3	166	176.8	187.3	197.8	208
<b>Torque difference (%)</b>																
	1.88	1.7	1.6	1.4	1.1	1.1	0.98	0.89	0.74	0.41	0.13	0.12	0.4	0.53	0.71	0.82

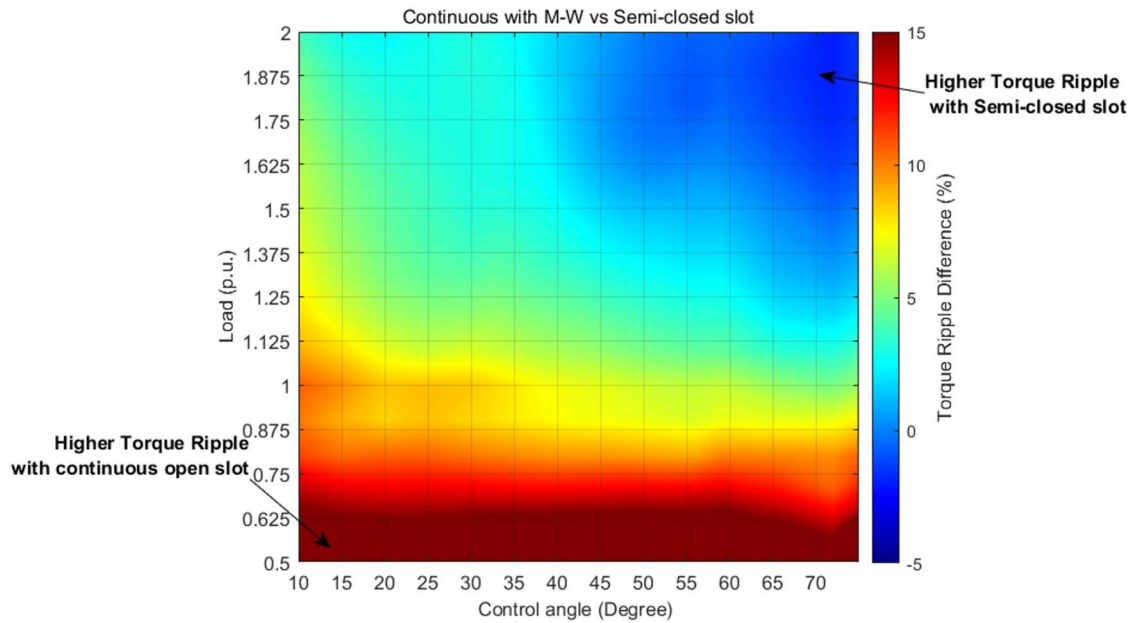


Figure 5.5 The Torque ripple difference between semi-closed slot opening motor (conventional hairpin winding) and open slot opening motor (continuous hairpin winding)

## 5.4 Investigation with Magnetic Wedge

The previous section has highlighted that the continuous hairpin winding, which leads to the adoption of the open slot design, has a detrimental impact on the torque ripple at various load and current angle values. To overcome this challenge, M-Ws could be used. The choice of a suitable material for the M-W is critical here, as the higher its relative permeability the lower the torque ripple is expected to be. On the other hand, a too-high value of the relative permeability increases the leakage fluxes and, in turn, output torque and high-frequency losses in the windings can be negatively affected. The maximum mean torque value that has been obtained with different control angles for any motor with six different permeability amounts was obtained and is shown in Table 5.2. The results are illustrated in Figure 5.6 when the control angle of equivalent to the maximum torque value for different loads. Considering the above, M-Ws with relative permeability values ranging from 1 to 20 are inserted in the proximity of the slot opening as shown in Figure 5.1c. Mean torque and torque ripple are investigated

vs. loading and current angle, as done in the previous comparative studies. The results relative to the mean torque are illustrated in Figure 5.7 and can be directly compared to those in Figure 5.3. The mean torque value for permeability values between 5 and 10 is higher than in other situations, while it is 1% lower than in the semi-closed slot case. Regarding the torque ripple, as expected, higher permeability values lead to lower values of it, as shown in the corresponding heat maps of Figure 5.8. In addition, at 1 p.u. and at a current angle which maximises the output torque, the semi-closed slot has a 2% lower torque ripple than the best case of continuous hairpin winding with M-W.

Table 5.2 Maximum mean torque value and their control angles with different permeability

Load (p.u)	0.5	0.6	0.7	0.8	0.9	1	1.1	1.2	1.3	1.4	1.5	1.6	1.7	1.8	1.9	2
Angle	30	32	34	36	36	38	40	40	42	42	45	45	45	45	45	50
Perm=1	46.3	56.6	67.1	77.6	88.2	99.4	109.7	120.4	131.2	141.9	152.6	163.3	173.8	184.2	194.4	204.6
Angle	30	32	34	36	36	38	40	40	42	42	45	45	45	45	50	50
Perm=2	46.8	57.3	67.9	78.5	89.3	100.1	110.9	121.7	132.6	143.3	154.1	164.8	175.3	185.6	195.8	206.2
Angle	30	32	34	36	36	38	40	42	42	42	45	45	45	45	50	50
Perm=5	47.4	58	68.6	79.3	90.1	100.9	111.8	122.6	133.4	144.1	154.8	165.4	175.7	185.9	196.1	206.2
Angle	30	32	34	36	38	39	40	42	42	42	45	45	45	45	50	50
Perm=10	47.6	58.2	68.8	79.5	90.1	100.8	111.6	122.2	132	143.4	153.9	164.1	174.2	184.1	194	203.8
Angle	30	32	34	36	38	38	40	40	42	42	45	45	45	45	50	50
Perm=15	47.6	58.1	68.7	79.2	89.8	100.4	111	121.5	132	142.4	152.6	162.8	172.7	182.4	192.1	201.7
Angle	30	32	34	36	36	38	40	40	42	42	45	45	45	45	50	50
Perm=20	47.6	58	68.4	78.9	89.4	99.9	110.4	120.9	131.2	141.5	151.6	161.6	171.5	181	190.5	200

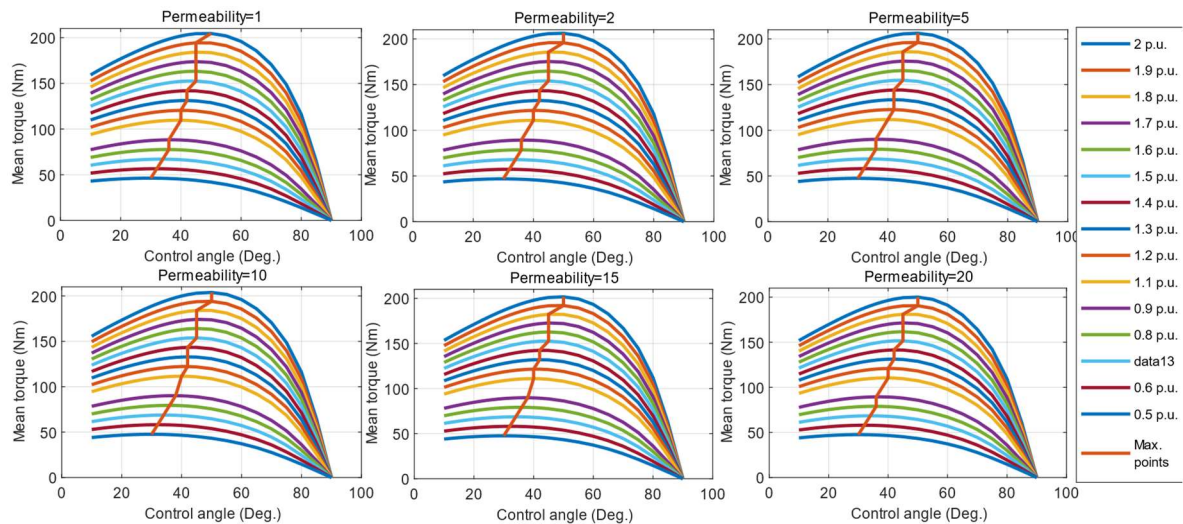


Figure 5.6 The mean torque curves versus control angle (Deg.) for any individual load (p.u.) in different M-W permeabilities and the specified control angle equivalent to the maximum mean torque value

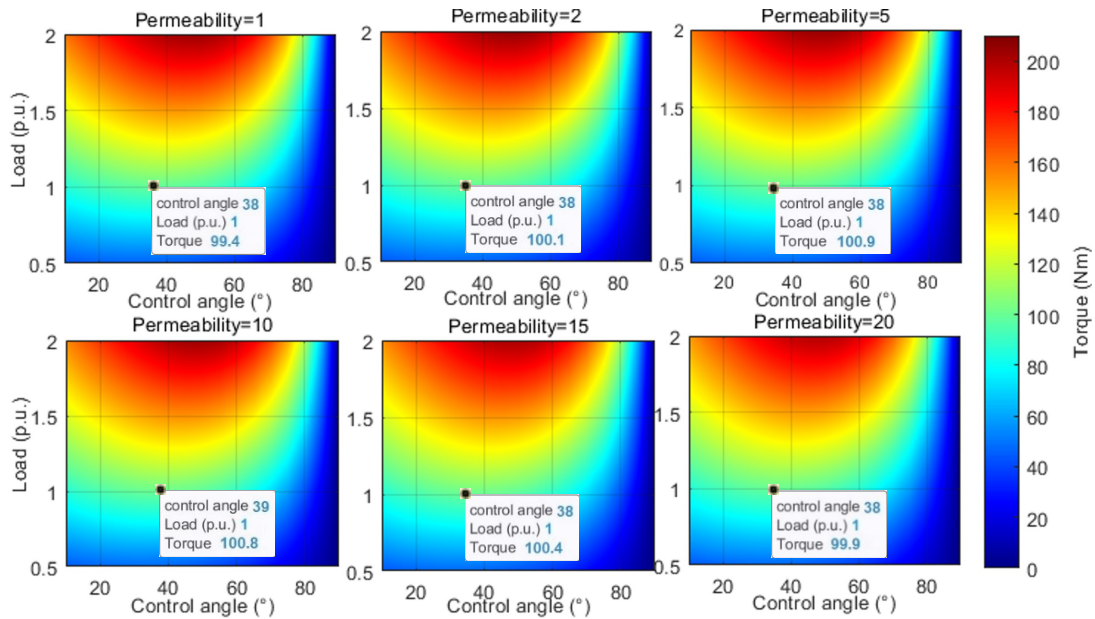


Figure 5.7 The Mean torque heat map vs. load and control angle using different permeability values for the M-W

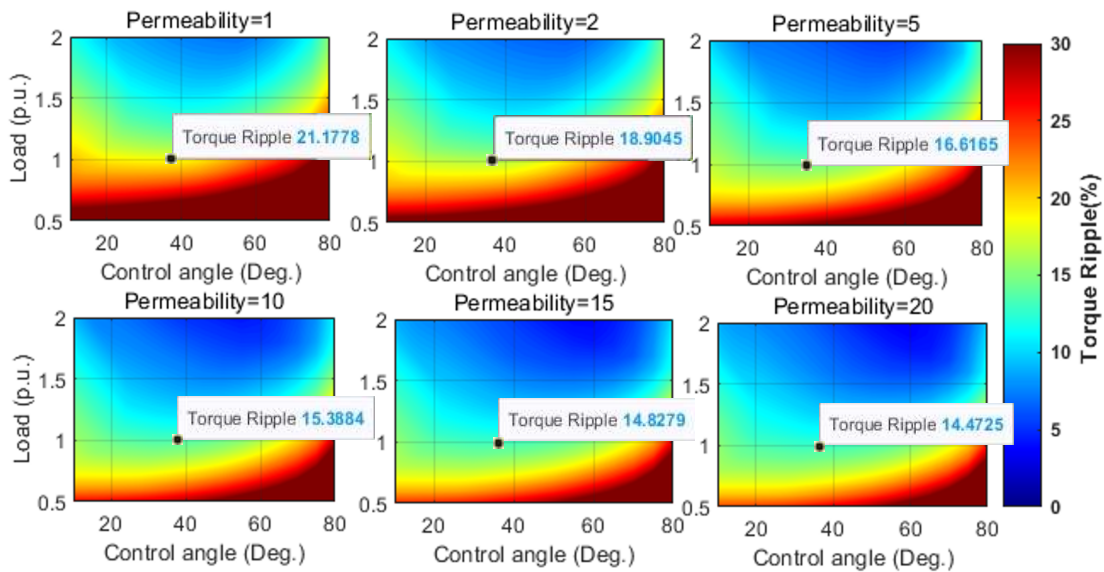


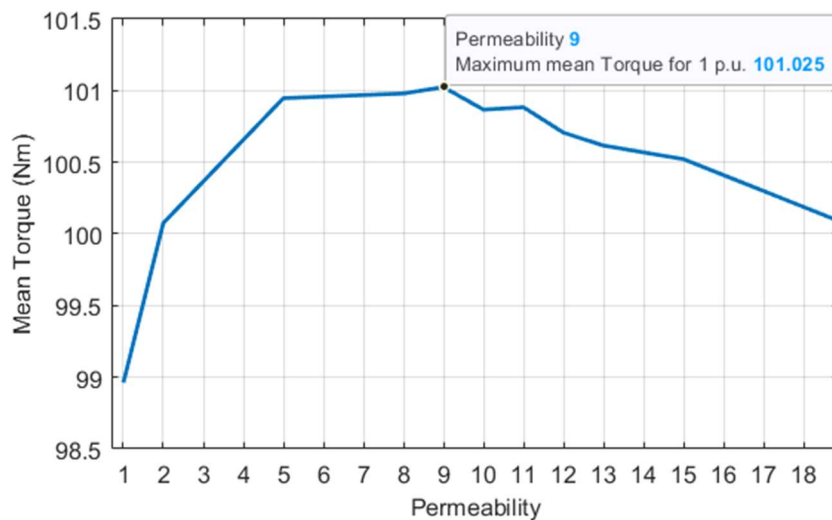
Figure 5.8 Torque ripple heat map vs. load and control angle using different permeability values for the M-W

### 5.4.1 Selection of the M-W permeability and comparison

To select the most suitable M-W permeability value for the motor under investigation, mean torque and torque ripple are studied under rated conditions (1 p.u.) and using a control angle which maximises the output torque. Figure 5.9a

shows the mean torque vs. M-W relative permeability, while the torque ripple is reported in Figure 5.9b. An M-W permeability value equal to 9 is chosen, as this corresponds to the maximum mean torque value with an acceptable torque ripple being achieved (i.e. 13.5%). In fact, increasing the permeability up to 20 does not lead to significant benefits, i.e. the torque ripple decreases by 0.5% only when moving from 9 to 20 (as highlighted in Figure 5.9). Comparing these results with the open slot opening design without M-W (see Figure 5.4), the torque ripple is reduced from  $\approx 19.3\%$  to  $\approx 13.5\%$ , while the semi-closed slot opening still presents the lowest torque ripple ( $\approx 11.9\%$ ). On the other hand, the mean torque remains basically the same.

As done in Section 5.3, the difference in % in terms of torque ripple between the motors with semi-closed slot opening and that with open slot equipping the M-W (with relative permeability equal to 9) is plotted below in Figure 5.10. While for most of the operating points under 1 p.u. the torque ripple is lower for the semi-closed slot design (positive values of the torque ripple difference), above 1 p.u. the trend is inverted due to saturation (negative values of torque ripple difference), i.e. torque ripple is lower in the motor with M-W.



(a)

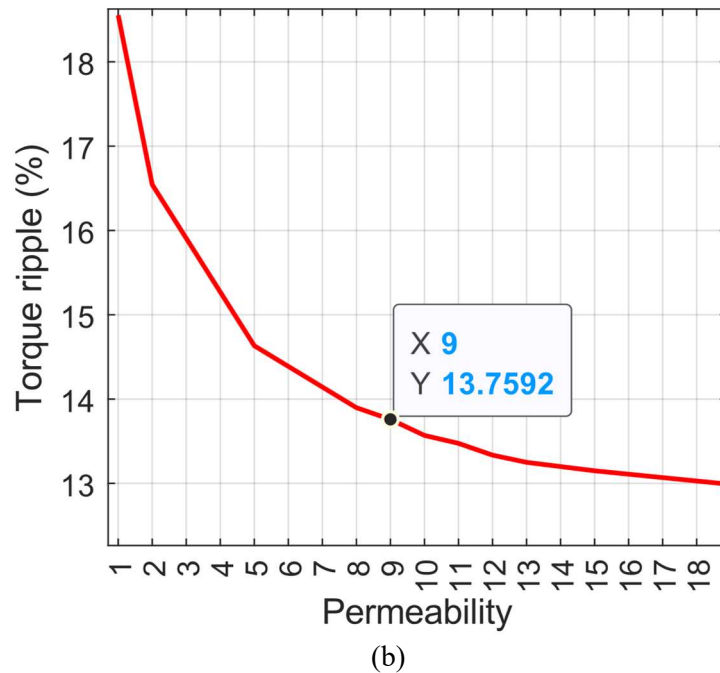


Figure 5.9 With a different permeability of M-W for a 1 p.u. load (a) Mean torque value, (b) Torque ripple percentage (%)

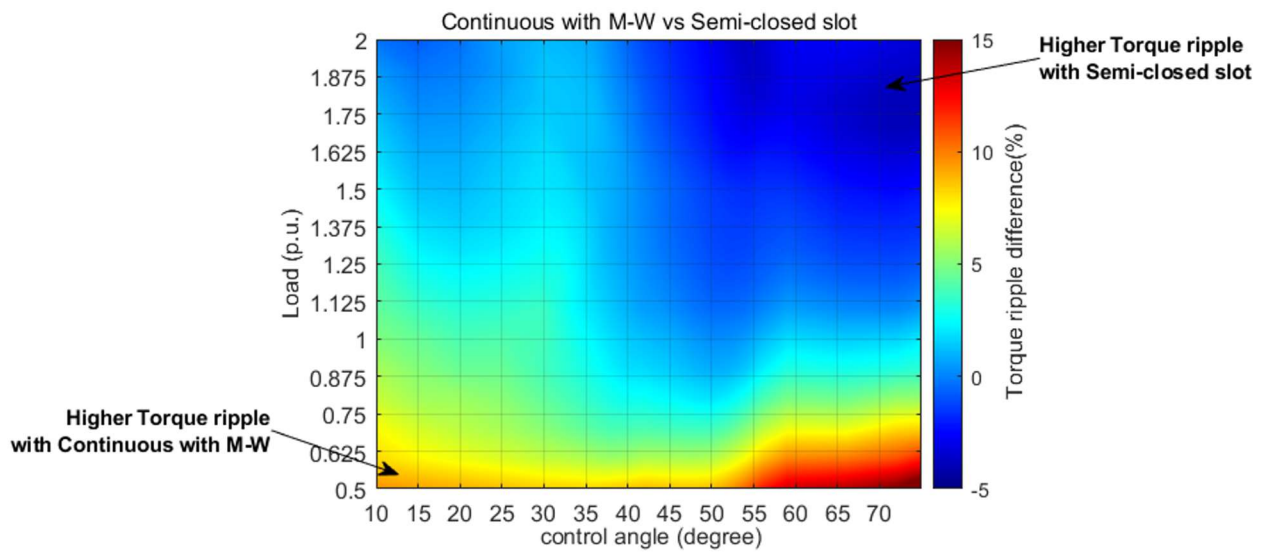


Figure 5.10 The Torque ripple difference between semi-closed slot opening motor (conventional hairpin winding) and open slot opening with an M-W motor (continuous hairpin winding)

### 5.4.2 Analysis of ohmic loss and efficiency

As already mentioned, the bottleneck of hairpin windings is the high losses at high-frequency operation (namely AC losses) due to skin and proximity effects. Introduced in (2.14) as the AC-to-DC loss ratio rather than different frequencies, the  $K_{Ru}$  could be analysed from point-to-point FEM simulation for a comparison between three stator slot opening topologies (i.e. semi-closed, open and open with M-W). In this subsection, the AC-to-DC loss ratio  $K_{Ru}$  for the three-stator slot opening topologies (i.e. semi-closed, open and open with M-W) is analysed. In Figure 11, the comparison in terms of  $K_{Ru}$  at various frequency values is illustrated at 1 p.u. loading. It can be seen that the motor with M-W has the lowest  $K_{Ru}$  value in the whole frequency range, while the open slot motor has the highest  $K_{Ru}$  values. It is to be borne in mind that the DC loss (i.e. the denominator of the  $K_{Ru}$  ratio) is the same for the three motors, meaning that an identical trend is expected if the total winding losses were to be plotted vs. frequency.

The other important characteristic is the efficiency map in the whole Torque-Speed curve. For these PMSM motors, the heat map plot of efficiency has been achieved. Figure 5.12 shows the efficiency percentage difference between the semi-closed slot and open slot opening with M-W motors until the rated speed has the same efficiency value. Higher than that speed, the efficiency of the semi-closed slot motor would be more. Besides, Figure 5.13 illustrates the Efficiency-Torque-Speed map while showing the motor efficiency in lower frequencies approximately is equal and at higher speeds, the open slot opening with M-W has more efficiency rather than the open slot opening motor. These two figures show that semi-closed slot has greater efficiency than or equal to the equivalent speed and torque amount open slot opening with M-W permeability equal to 9. This difference at the worst case is not higher than 1% in higher speed and 3 times of rated speed and torque lower than 10 Nm. Also, this happens for this open slot opening with M-W rather than the equivalent open slot opening motor.

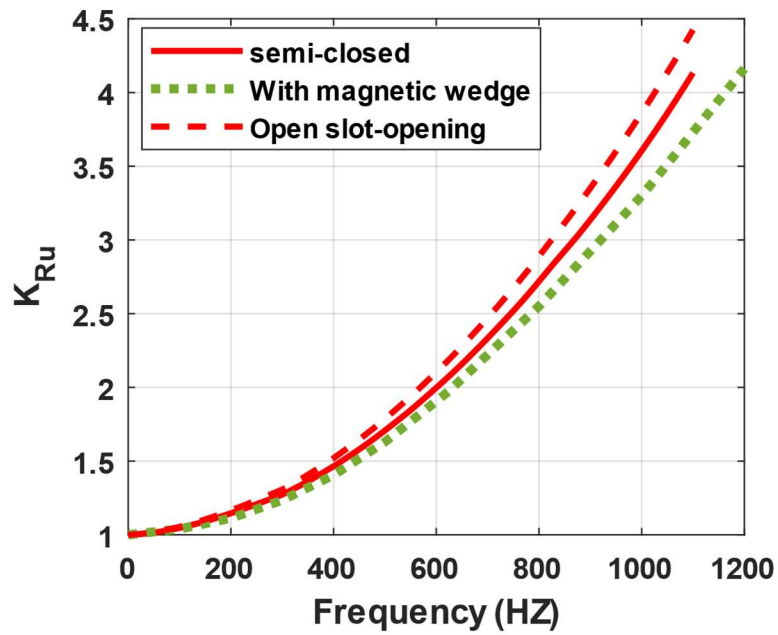


Figure 5.11 The AC-to-DC loss ratio vs. frequency for the motors with different slot opening designs.

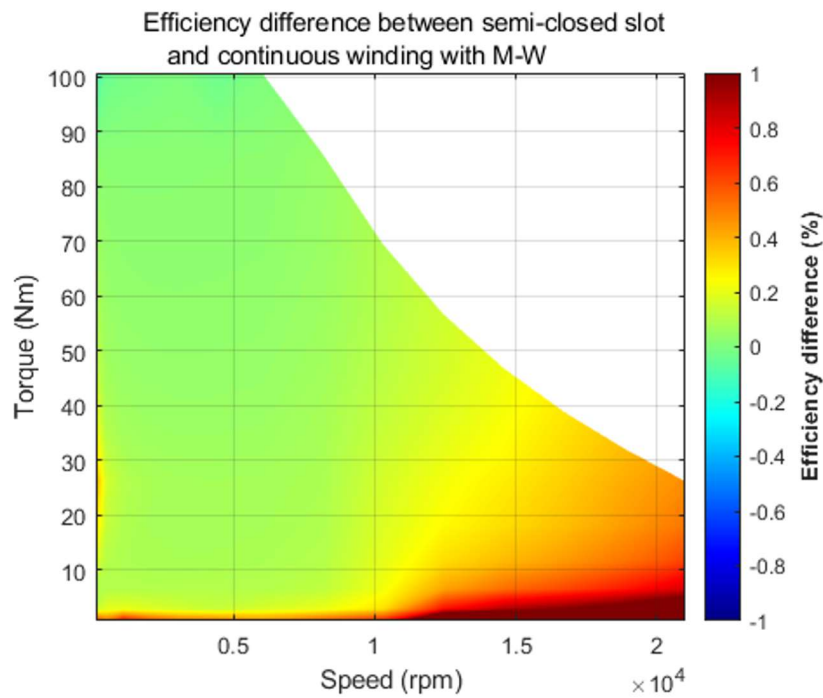


Figure 5.12 Efficiency Difference in Torque-speed map for semi-closed slot versus open slot opening with M-W

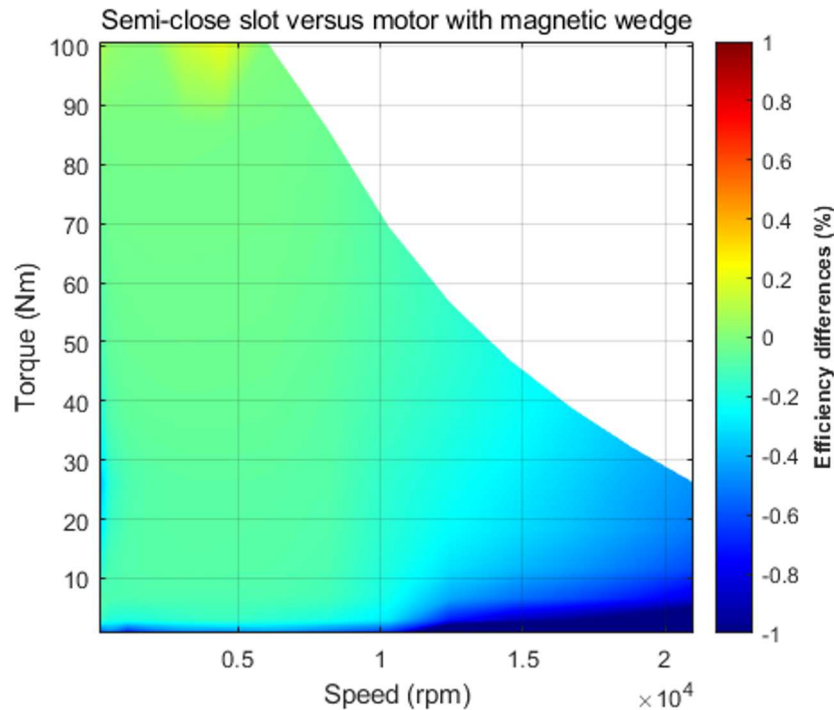


Figure 5.13 Efficiency Difference in Torque-speed map for open slot opening versus open slot opening with M-W

## 5.5 Conclusion

In this chapter, an IPM was taken as a case study to investigate the adoption of a continuous hairpin winding. In particular, this research presented a comparison between conventional and continuous hairpin windings. The study was based on the rationale that a continuous hairpin winding needs an open slot opening design for its radial insertion, while the conventional counterpart can be inserted axially, keeping the slot opening in its standard semi-closed arrangement. Considering the above, the investigation was on the electromagnetic performance metrics which were expected to be most sensitive to this slot opening layout change. In other words, output torque and torque ripple were studied at different values of the loading and current angle, while the AC losses were reported against the operating frequency under rated load conditions. It was found that the open slot design significantly deteriorates the torque ripple of the motor, but with minimal impact on the output torque. However, under heavy saturation conditions, the overall

situation improved. It was also found that the open slot design increases the winding losses at high-frequency operation. To improve these performance metrics without renouncing the continuous hairpin winding, the use of semi-magnetic wedges was proposed, with excellent results being achieved with a value of the wedge material's permeability equal to 9. With such a precaution, the torque ripple passes from  $\approx 19.3\%$  to  $\approx 13.5\%$ , against the 11.9% registered for the semi-closed slot opening case. Regarding the winding losses, the open slot design presented the lowest values in the whole frequency range. In conclusion, while further studies need to be carried out, this preliminary research proved the potential applicability of continuous hairpin windings in electric motors for transport applications.

# Chapter 6

## Conclusions

Traction applications are driving the limits of high speed and power density with breakthroughs in cores, magnets, and winding designs. In today's perspective of prioritizing torque density, PMSMs are extensively utilized as propulsion motors in traction applications. In addition, hairpin windings are a key technology in this direction, despite being characterized by high ohmic losses at high frequencies.

In this thesis, first, a comparative analysis was conducted between preliminary designs of two machines with random and hairpin windings, with the study being focused on investigating the performance at two different frequencies, i.e. 200 Hz and 1 kHz. After the preliminary design process utilizing classical sizing equations, FE models were built for validation purposes. The comparative analysis showed acceptable accuracy for most of the electromagnetic quantities of interest. Regarding the AC losses and efficiency in higher frequencies, the comparative results illustrated that for random-wound windings the classical sizing equations could be used with a certain level of “safety”, while hairpin windings require more accurate and in-depth analyses and the relative sizing tools need to be improved.

Based on the above conclusion, the next step was developing a fast and accurate optimization procedure for the optimal exploitation of hairpin technologies in PMSMs. The optimization tool was aimed at maximizing power density and efficiency, which are key figures for transport applications. The optimization strategy, based first on a “one-by-one” sensitivity study and then on the

application of a multi-objective evolutionary algorithm, proved that these two objectives can be pursued and achieved simultaneously, with excellent performance enhancements being obtained. The optimal motor which was selected for comparative purposes against the benchmark motor (intended for racing car applications) with random windings and a non-optimal hairpin motor, showed that efficiency, volume power density, and power losses, were improved by 0.15%, 10.55%, and 3.4%, respectively.

A major contribution of this research was based on the studies of the effects of both operating temperatures and rotor topologies on hairpin winding losses. The main outcomes showed that there exists a frequency value at which the losses at higher temperatures are lower than those registered at lower temperatures (specifically at ambient temperature). For the benchmark case study, this frequency value was equal to 637 Hz. A higher frequency value was found for the other four rotor topologies investigated, i.e., 704.7, 782.44, 909.25, and 1045.25 Hz, but still higher operating temperatures seem to be beneficial when AC losses are involved. Experimental results were also carried out to validate this concept. A motorette wound with pre-formed conductors was used and tested in a thermal chamber, and the ohmic losses were recorded at different frequencies and temperatures. The experimental results confirmed the simulation findings, highlighting that a temperature-oriented design process for machines equipping hairpin conductors would be worthwhile in the context of reducing AC losses in this winding technology.

The last step of this research was to investigate the feasibility of continuous hairpin windings in place of standard hairpin layouts, to reduce or even remove the welding spots. This part of the research featured a comparison between conventional and continuous hairpin windings in terms of electromagnetic performance only. The output torque and torque ripple were studied at different values of the loading and current angle, while the AC losses were reported against the operating frequency under rated load conditions. The results showed that the

continuous hairpin winding, enabled by an open slot design, significantly worsens the torque ripple of the motor, but with minimal impact on the output torque. However, under heavy saturation conditions, the overall situation improved. It was also found that the open slot design increases the winding losses at high-frequency operation. To improve the performance, a semi-magnetic slot wedge was proposed, and the torque ripple was improved passing from  $\approx 19.3\%$  to  $\approx 13.5\%$ , against the  $11.9\%$  registered for the semi-closed slot opening case (i.e. standard hairpin winding). Regarding the winding losses, the open slot design presented the lowest values in the whole frequency range. In conclusion, while further studies need to be carried out, this preliminary research proved the potential applicability of continuous hairpin windings in electric motors for transport applications.

# References

- [1] Hossein Ranjbar; Mahdi Sharifzadeh, "Electrification of Transportation," in *Industry 4.0 Vision for the Supply of Energy and Materials: Enabling Technologies and Emerging Applications*, Wiley, 2022, pp.269-296, doi: 10.1002/9781119695868.ch10.
- [2] N. Swaminathan, S. R. P. Reddy, K. RajaShekara and K. S. Haran, "Flying Cars and eVTOLs—Technology Advancements, Powertrain Architectures, and Design," in *IEEE Transactions on Transportation Electrification*, vol. 8, no. 4, pp. 4105-4117, Dec. 2022, doi: 10.1109/TTE.2022.3172960.
- [3] M. Esmacili, A. Anvari-Moghaddam, S. M. Muyeen and V. S. Perić, "On the Role of Renewable Energy Policies and Electric Vehicle Deployment Incentives for a Greener Sector Coupling," in *IEEE Access*, vol. 10, pp. 53873-53893, 2022, doi: 10.1109/ACCESS.2022.3176012.
- [4] T. Petri, M. Keller and N. Parspour, "The Insulation Resilience of Inverter-Fed Low Voltage Traction Machines: Review, Challenges, and Opportunities," in *IEEE Access*, vol. 10, pp. 104023-104049, 2022, doi: 10.1109/ACCESS.2022.3210348.
- [5] G. Venturini, M. Carbonieri, L. Di Leonardo and M. Popescu, "Hairpin Windings for Traction Machines: Analysis and Comparison," 2022 International Conference on Electrical Machines (ICEM), Valencia, Spain, 2022, pp. 1655-1661, doi: 10.1109/ICEM51905.2022.9910905.
- [6] J. T. J. a. V. H. Pyrhonen, *Design of rotating electrical machines*, John Wiley & Sons, 2013.
- [7] A. Kadavergu, A. K and N. Krishna Kumari, "Development of Motor Gear Powertrain System for Electrical Vehicle," 2021 Innovations in Power and Advanced Computing Technologies (i-PACT), Kuala Lumpur, Malaysia, 2021, pp. 1-6, doi: 10.1109/i-PACT52855.2021.9697055.
- [8] A. Hebala et al., "Feasibility Design Study of High-Performance, High-Power-Density Propulsion Motor for Middle-Range Electric Aircraft," 2020 IEEE 29th International Symposium on Industrial Electronics (ISIE), Delft, Netherlands, 2020, pp. 300-306, doi: 10.1109/ISIE45063.2020.9152551.
- [9] T. Dimier, M. Cossale and T. Wellerdieck, "Comparison of Stator Winding Technologies for High-Speed Motors in Electric Propulsion Systems," 2020 International Conference on Electrical Machines (ICEM), Gothenburg, Sweden, 2020, pp. 2406-2412, doi: 10.1109/ICEM49940.2020.9270943.
- [10] M. Pastura et al., "Partial Discharges in Electrical Machines for the More Electric Aircraft—Part I: A Comprehensive Modeling Tool for the Characterization of Electric Drives Based on Fast Switching Semiconductors," in *IEEE Access*, vol. 9, pp. 27109-27121, 2021, doi: 10.1109/ACCESS.2021.3058083.
- [11] H. -J. Park and M. -S. Lim, "Design of High Power Density and High Efficiency Wound-Field Synchronous Motor for Electric Vehicle Traction," in *IEEE Access*, vol. 7, pp. 46677-46685, 2019, doi: 10.1109/ACCESS.2019.2907800.
- [12] A. Arzillo et al., "An Analytical Approach for the Design of Innovative Hairpin Winding Layouts," 2020 International Conference on Electrical Machines (ICEM), Gothenburg, Sweden, 2020, pp. 1534-1539, doi: 10.1109/ICEM49940.2020.9270927.

- [13] S. Nuzzo, D. Barater, C. Gerada and P. Vai, "Hairpin Windings: An Opportunity for Next-Generation E-Motors in Transportation," in *IEEE Industrial Electronics Magazine*, vol. 16, no. 4, pp. 52-59, Dec. 2022, doi: 10.1109/MIE.2021.3106571.
- [14] M. S. Islam, I. Husain, A. Ahmed and A. Sathyan, "Asymmetric Bar Winding for High-Speed Traction Electric Machines," in *IEEE Transactions on Transportation Electrification*, vol. 6, no. 1, pp. 3-15, March 2020, doi: 10.1109/TTE.2019.2962329.
- [15] F. Scuiller, H. Zahr and E. Semail, "Maximum Reachable Torque, Power and Speed for Five-Phase SPM Machine With Low Armature Reaction," in *IEEE Transactions on Energy Conversion*, vol. 31, no. 3, pp. 959-969, Sept. 2016, doi: 10.1109/TEC.2016.2542581.
- [16] A. Arzillo et al., "Challenges and Future opportunities of Hairpin Technologies," 2020 IEEE 29th International Symposium on Industrial Electronics (ISIE), Delft, Netherlands, 2020, pp. 277-282, doi: 10.1109/ISIE45063.2020.9152417.
- [17] J. Hagedorn, F. S. Blanc, and J. Fleischer, "Handbook of Coil Winding: Technologies for efficient electrical wound products and their automated production", Springer, 2017.
- [18] F. Wirth, T. Kirgör, J. Hofmann and J. Fleischer, "FE-Based Simulation of Hairpin Shaping Processes for Traction Drives," 2018 8th International Electric Drives Production Conference (EDPC), Schweinfurt, Germany, pp. 1-5, 2018.
- [19] Y. Zhao, D. Li, T. Pei and R. Qu, "Overview of the rectangular wire windings AC electrical machine," in *CES Transactions on Electrical Machines and Systems*, vol. 3, no. 2, pp. 160-169, June 2019.
- [20] M. Soltani, S. Nuzzo, D. Barater, G. Franceschini, "A Multi-Objective Design Optimization for a Permanent Magnet Synchronous Machine with Hairpin Winding Intended for Transport Applications" *Electronics* 2021, 10, 3162. <https://doi.org/10.3390/electronics10243162>
- [21] M. Soltani, S. Nuzzo, D. Barater, G. Franceschini. "Considerations on the Preliminary Sizing of Electrical Machines with Hairpin Windings" In *Proceedings of the 2021 IEEE Workshop on Electrical Machines Design, Control and Diagnosis (WEMDCD)*, Modena, Italy, 8-9 April 2021; pp. 46-51.
- [22] Selema, A.; Ibrahim, M.N.; Sergeant, P. Mitigation of High-Frequency Eddy Current Losses in Hairpin Winding Machines. *Machines* 2022, 10, 328. <https://doi.org/10.3390/machines10050328>.
- [23] Deming Zhu, Xin Qiu, Nan Zhou and Yangguang Yan, "A comparative study of winding factors between distributed windings and non-overlapping concentrated windings," 2008 Third International Conference on Electric Utility Deregulation and Restructuring and Power Technologies, Nanjing, pp. 2725-2729, 2008.
- [24] M. Popescu, J. Goss, D. A. Staton, D. Hawkins, Y. C. Chong and A. Boglietti, "Electrical Vehicles—Practical Solutions for Power Traction Motor Systems," in *IEEE Transactions on Industry Applications*, vol. 54, no. 3, pp. 2751-2762, May-June 2018.
- [25] T. Ishigami, Y. Tanaka and H. Homma, "Motor Stator With Thick Rectangular Wire Lap Winding for HEVs," in *IEEE Transactions on Industry Applications*, vol. 51, no. 4, pp. 2917-2923, July-Aug. 2015.
- [26] F. Momen, K. Rahman and Y. Son, "Electrical Propulsion System Design of Chevrolet Bolt Battery Electric Vehicle," in *IEEE Transactions on Industry Applications*, vol. 55, no. 1, pp. 376-384, Jan.-Feb. 2019.
- [27] G. Berardi and N. Bianchi, "High-Speed PM Generators for Organic Rankine Cycle Systems: Reduction of Eddy Current Rotor Losses," in *IEEE Transactions on Industry Applications*, vol. 55, no. 6, pp. 5800-5808, Nov.-Dec. 2019.
- [28] G. Berardi and N. Bianchi, "Design Guideline of an AC Hairpin Winding," 2018 XIII International Conference on Electrical Machines (ICEM), Alexandroupoli, pp. 2444-2450, 2018.

## References

---

- [29] N. Bianchi and G. Berardi, "Analytical Approach to Design Hairpin Windings in High Performance Electric Vehicle Motors," 2018 IEEE Energy Conversion Congress and Exposition (ECCE), Portland, OR, pp. 4398-4405, 2018.
- [30] E. Preci et al., "Segmented Hairpin Topology for Reduced Losses at High-Frequency Operations," in IEEE Transactions on Transportation Electrification, vol. 8, no. 1, pp. 688-698, March 2022, doi: 10.1109/TTE.2021.3103821.
- [31] X. Sun, Z. Shi, G. Lei, Y. Guo and J. Zhu, "Analysis and Design Optimization of a Permanent Magnet Synchronous Motor for a Campus Patrol Electric Vehicle," in IEEE Transactions on Vehicular Technology, vol. 68, no. 11, pp. 10535-10544, Nov. 2019, doi: 10.1109/TVT.2019.2939794.
- [32] O. Sandre-Hernandez, R. Morales-Caporal, J. Rangel-Magdaleno, H. Peregrina-Barreto and J. N. Hernandez-Perez, "Parameter Identification of PMSMs Using Experimental Measurements and a PSO Algorithm," in IEEE Transactions on Instrumentation and Measurement, vol. 64, no. 8, pp. 2146-2154, Aug. 2015, doi: 10.1109/TIM.2015.2390958.
- [33] L. Dang, N. Bernard, N. Bracikowski and G. Berthiau, "Design Optimization with Flux Weakening of High-Speed PMSM for Electrical Vehicle Considering the Driving Cycle," in IEEE Transactions on Industrial Electronics, vol. 64, no. 12, pp. 9834-9843, Dec. 2017, doi: 10.1109/TIE.2017.2726962.
- [34] G. Feng, C. Lai and N. C. Kar, "An Analytical Solution to Optimal Stator Current Design for PMSM Torque Ripple Minimization With Minimal Machine Losses," in IEEE Transactions on Industrial Electronics, vol. 64, no. 10, pp. 7655-7665, Oct. 2017, doi: 10.1109/TIE.2017.2694354.
- [35] W. Zhao, X. Wang, C. Gerada, H. Zhang, C. Liu and Y. Wang, "Multi-Physics and Multi-Objective Optimization of a High Speed PMSM for High Performance Applications," in IEEE Transactions on Magnetics, vol. 54, no. 11, pp. 1-5, Nov. 2018, Art no. 8106405, doi: 10.1109/TMAG.2018.2835504.
- [36] D. -S. Jung, Y. -H. Kim, U. -H. Lee and H. -D. Lee, "Optimum Design of the Electric Vehicle Traction Motor Using the Hairpin Winding," 2012 IEEE 75th Vehicular Technology Conference (VTC Spring), Yokohama, Japan, 2012, pp. 1-4, doi: 10.1109/VETECS.2012.6240320.
- [37] L. Di Leonardo, G. Fabri, A. Credo, M. Tursini, and M. Villani, "Impact of Wire Selection on the Performance of an Induction Motor for Automotive Applications," Energies, vol. 15, no. 11, p. 3876, May 2022, doi: 10.3390/en15113876.
- [38] S. Xue, M. Michon, M. Popescu and G. Volpe, "Optimisation of Hairpin Winding in Electric Traction Motor Applications," 2021 IEEE International Electric Machines & Drives Conference (IEMDC), Hartford, CT, USA, 2021, pp. 1-7, doi: 10.1109/IEMDC47953.2021.9449605.
- [39] N. Rivière, M. Villani and M. Popescu, "Optimisation of a High Speed Copper Rotor Induction Motor for a Traction Application," IECON 2019 - 45th Annual Conference of the IEEE Industrial Electronics Society, Lisbon, Portugal, 2019, pp. 2720-2725, doi: 10.1109/IECON.2019.8927627.
- [40] P. Quassolo, F. Togni, E. Preci and A. Acquaviva, "Design Considerations For High Power Density Traction PM Motors With Hairpin Windings," 2022 International Conference on Electrical Machines (ICEM), Valencia, Spain, 2022, pp. 1669-1674, doi: 10.1109/ICEM51905.2022.9910656.
- [41] E. Preci et al., "Hairpin Windings: Sensitivity Analysis and Guidelines to Reduce AC Losses," 2021 IEEE Workshop on Electrical Machines Design, Control and Diagnosis (WEMDCD), Modena, Italy, 2021, pp. 82-87, doi: 10.1109/WEMDCD51469.2021.9425643.

- [42] E. Sayed et al., "Review of Electric Machines in More-/Hybrid-/Turbo-Electric Aircraft," in *IEEE Transactions on Transportation Electrification*, vol. 7, no. 4, pp. 2976-3005, Dec. 2021, doi: 10.1109/TTE.2021.3089605.
- [43] J. Song, J. Li, Z. Hu, L. Xu, J. Hu and M. Ouyang, "Analysis of Torque Performance of Motor with Continuous Flat Wire," *IECON 2021 – 47th Annual Conference of the IEEE Industrial Electronics Society*, 2021, pp. 1-5, doi: 10.1109/IECON48115.2021.9589959.
- [44] A. Nasr, G. Zito, A. Abdelli and K. Malick Cisse, "A Methodology to Design Hairpin Winding for Improved Thermal Performances in a Permanent Magnet Assisted Synchronous Reluctance Motor," *2022 International Conference on Electrical Machines (ICEM)*, 2022, pp. 1176-1182, doi: 10.1109/ICEM51905.2022.9910895.
- [45] A. Hebala, S. Nuzzo, P. H. Connor, G. Volpe, C. Gerada, and M. Galea, "Analysis and Mitigation of AC Losses in High Performance Propulsion Motors," *Machines*, vol. 10, no. 9, p. 780, Sep. 2022, doi: 10.3390/machines10090780.
- [46] M. Di Nardo, A. Marfoli, M. Degano and C. Gerada, "Open and Closed Rotor Slots Design of Single and Double Cages Induction Motor," *2021 IEEE Workshop on Electrical Machines Design, Control and Diagnosis (WEMDCD)*, 2021, pp. 125-130, doi: 10.1109/WEMDCD51469.2021.9425665.
- [47] D. Li, G. Feng, W. Li, B. Zhang, and J. Zhang, "Effect of Stator Slots on Electromagnetic Performance of a High-Voltage Line-Start Permanent Magnet Synchronous Motor," *Energies*, vol. 15, no. 9, p. 3358, May 2022, doi: 10.3390/en15093358.
- [48] D. B. Pinhal and D. Gerling, "Performance Map Calculation of a Salient-Pole Synchronous Motor with Hairpin Winding," *2019 IEEE 28th International Symposium on Industrial Electronics (ISIE)*, Vancouver, BC, Canada, pp. 359-365, 2019.
- [49] M. Aoyama and J. Deng, "Visualization and quantitative evaluation of eddy current loss in bar-wound type permanent magnet synchronous motor for mild-hybrid vehicles," in *CES Transactions on Electrical Machines and Systems*, vol. 3, no. 3, pp. 269-278, Sept. 2019.
- [50] G. Devito, S. Nuzzo, D. Barater, G. Franceschini, L. Papini and P. Bolognesi, "Design of the Propulsion System for a Formula SAE racing car based on a Brushless Motor," *2021 IEEE Workshop on Electrical Machines Design, Control and Diagnosis (WEMDCD)*, Modena, Italy, 2021, pp. 318-324, doi: 10.1109/WEMDCD51469.2021.9425626.
- [51] M. Soltani, S. Nuzzo, D. Barater, and G. Franceschini, "Investigation of the Temperature Effects on Copper Losses in Hairpin Windings," *Machines*, vol. 10, no. 8, p. 715, Aug. 2022, doi: 10.3390/machines10080715.
- [52] G. De Donato, F. Giulii Capponi and F. Caricchi, "On the Use of Magnetic Wedges in Axial Flux Permanent Magnet Machines," in *IEEE Transactions on Industrial Electronics*, vol. 60, no. 11, pp. 4831-4840, Nov. 2013, doi: 10.1109/TIE.2012.2225392.
- [53] Z. Yang, S. Wang, Y. Sun and H. Cao, "Vibration Reduction by Magnetic Slot Wedge for Rotating Armature Permanent Magnet Motors," in *IEEE Transactions on Industry Applications*, vol. 56, no. 5, pp. 4882-4888, Sept.-Oct. 2020, doi: 10.1109/TIA.2020.3008670.
- [54] S. Abdi, E. Abdi and R. McMahan, "Numerical Analysis of Stator Magnetic Wedge Effects on Equivalent Circuit Parameters of Brushless Doubly Fed Machines," *2018 XIII International Conference on Electrical Machines (ICEM)*, 2018, pp. 879-884, doi: 10.1109/ICELMACH.2018.8506747.
- [55] 60034-2-1. IEC, "Rotating electrical machines - Part 2-1: Standard methods for determining losses and efficiency from tests". 27 06 2014.
- [56] H. Lv, L. Zhang, C. Yao, Q. Sun, J. Du, and X. Chen, "An Improved Permanent Magnet Synchronous Motor Rotor Position Observer Design Based on Error Harmonic Elimination," *Machines*, vol. 10, no. 8, p. 633, Jul. 2022, doi: 10.3390/machines10080633.

## References

---

- [57] Formula SAE Rules 2021 Version 1.0. Available online: [www.fsaeonline.com/cdsweb/gen/DocumentResources.aspx](http://www.fsaeonline.com/cdsweb/gen/DocumentResources.aspx) (accessed on 11-19-2022).
- [58] C.A.C. Coello, B.G. Lamont, A. Van Veldhuizen, "Evolutionary Algorithms for Solving Multi-Objective Problems", Springer: New York, NY, USA, 2007; Volume 5.
- [59] X. Huang, B. Jiang, M. N. Alhallak, S. Nategh, Y. Liu and A. Boglietti, "Experimental Evaluation of Conductor Insulations Used in E-mobility Traction Motors," 2021 IEEE Workshop on Electrical Machines Design, Control and Diagnosis (WEMDCD), Modena, Italy, 2021, pp. 249-253, doi: 10.1109/WEMDCD51469.2021.9425683.
- [60] Y. -C. Xing, Q. -A. Lv, B. Lei, H. -J. Xiang, R. -G. Zhu and C. Liu, "Analysis of Transient Current Distribution in Copper Strips of Different Structures for Electromagnetic Railgun," in IEEE Transactions on Plasma Science, vol. 43, no. 5, pp. 1566-1571, May 2015, doi: 10.1109/TPS.2015.2414095.